Mon. Not. R. Astron. Soc. **306,** 857–896 (1999)

The *ROSAT* Brightest Cluster Sample – III. Optical spectra of the central cluster galaxies

C. S. Crawford,[1⋆] S. W. Allen,[1] H. Ebeling,[2] A. C. Edge[1] and A. C. Fabian[1]
[1]*Institute of Astronomy, Madingley Road, Cambridge CB3 0HA*
[2]*Institute for Astronomy, 2680 Woodlawn Drive, Honolulu, HI 96822, USA*

Accepted 1999 February 16. Received 1998 December 21

ABSTRACT

We present new spectra of dominant galaxies in X-ray-selected clusters of galaxies, which combine with our previously published spectra to form a sample of 256 dominant galaxies in 215 clusters. 177 of the clusters are members of the *ROSAT* Brightest Cluster Sample (BCS; Ebeling et al.), and 17 have no previous measured redshift. This is the first paper in a series correlating the properties of brightest cluster galaxies and their host clusters in the radio, optical and X-ray wavebands.

27 per cent of the central dominant galaxies have emission-line spectra, all but five with line intensity ratios typical of cooling flow nebulae. A further 6 per cent show only [N II]λλ6548, 6584 with Hα in absorption. We find no evidence for an increase in the frequency of line emission with X-ray luminosity. Purely X-ray-selected clusters at low redshift have a higher probability of containing line emission. The projected separation between the optical position of the dominant galaxy and its host cluster X-ray centroid is less for the line-emitting galaxies than for those without line emission, consistent with a closer association of the central galaxy and the gravitational centre in cooling flow clusters.

The more Hα-luminous galaxies have larger emission-line regions and show a higher ratio of Balmer to forbidden line emission, although there is a continuous trend of ionization behaviour across four decades in Hα luminosity. Galaxies with the more luminous line emission [$L(\mathrm{H}\alpha) > 10^{41}$ erg s^{-1}] show a significantly bluer continuum, whereas lower luminosity and [N II]-only line emitters have continua that differ little from those of non-line-emitting dominant galaxies. Values of the Balmer decrement in the more luminous systems commonly imply intrinsic reddening of $E(B-V) \sim 0.3$ and, when this is corrected for, the excess blue light can be characterized by a population of massive young stars. Several of the galaxies require a large population of O stars, which also provide sufficient photoionization to produce the observed Hα luminosity. The large number of lower mass stars relative to the O-star population suggests that this anomalous population is caused by a series of starbursts in the central galaxy.

The lower Hα-luminosity systems show a higher ionization state and few massive stars, requiring instead the introduction of a harder source of photoionization, such as turbulent mixing layers, or low-level nuclear activity. The line emission from the systems showing only [N II] is very similar to low-level LINER activity commonly found in many normal elliptical galaxies.

Key words: surveys – galaxies: clusters: general – cooling flows – galaxies: elliptical and lenticular, cD – galaxies: stellar content – X-rays: galaxies.

1 INTRODUCTION

We have compiled the *ROSAT* Brightest Cluster Sample (BCS) (Ebeling et al. 1998, hereafter Paper I), which is a 90 per cent flux-complete sample of the 201 X-ray-brightest clusters of galaxies in the northern extragalactic hemisphere ($\delta \geq 0°$ and $|b| \geq 20°$) within $z = 0.3$. The clusters were selected from their X-ray emission in the *ROSAT* All-Sky Survey (RASS) (Voges 1992), and include both clusters listed in optical catalogues

⋆E-mail: csc@ast.cam.ac.uk

and systems newly discovered through their X-ray properties (Crawford et al. 1995, hereafter C95; Paper I). The BCS is now redshift-complete at unabsorbed fluxes greater than 4.4×10^{-12} erg cm^{-2} s^{-1} in the 0.1–2.4 keV *ROSAT* band (Paper I). Paper I also tabulates two additional clusters with $z > 0.3$ that fulfil all the other BCS criteria (RXJ1532.9 + 3021 and Z1953). The BCS is the largest statistically complete X-ray-selected sample of clusters to date, and has been used to derive the cluster log N–log S distribution (Paper I), the cluster–cluster correlation function (Edge et al., in preparation), and also the X-ray luminosity function out to a redshift of 0.3 (Ebeling et al. 1997, hereafter Paper II). The BCS forms a unique statistical sample to define the characteristics of clusters at other wavebands and their dependence on the global cluster properties, without the biases inherent in optically-selected or radio-selected samples.

As part of the selection and compilation of the BCS, we have published optical spectra of central dominant galaxies in both Abell and Zwicky clusters without a previously known redshift, and also of the new *ROSAT*-discovered clusters (Allen et al. 1992, hereafter A92; C95). Preliminary analyses of the spectra of these galaxies show that around one-third of them display anomalies such as a spectrum featuring luminous emission lines and an excess ultraviolet/blue continuum. Such features are well known to be associated with galaxies at the centres of cooling flows (Hu, Cowie & Wang 1985; Johnstone, Fabian & Nulsen 1987, hereafter JFN; Heckman et al. 1989; Romanishin 1987; Donahue, Stocke & Gioia 1992; McNamara & O'Connell 1989, 1992, 1993), and preferentially with those that contain a radio source (Heckman et al. 1989; C95). The blue continuum is directly attributable to a modest amount of recent massive star formation, which can also power some of the luminous line emission (Allen 1995).

This paper is the first in a series in which we compile and correlate the properties of the brightest cluster galaxies (BCGs) and their host clusters in three wavebands. We present optical spectra of the dominant galaxies of 87 per cent of the BCS; subsequent papers will compile results from optical and radio images (Edge et al., in preparation) and the cluster X-ray properties (Crawford et al., in preparation; Ebeling et al., in preparation) in order to perform a full statistical analysis of the sample. A value of the Hubble constant of $H_0 = 50\,\mathrm{km\,s^{-1}\,Mpc^{-1}}$ and a cosmological deceleration parameter of $q_0 = 0.5$ have been used throughout this paper; where cluster properties are quoted from the literature, we convert them to this assumed cosmology.

2 OBSERVATIONS AND DATA REDUCTION

2.1 Target selection and samples

The BCS is comprised of clusters culled from a positional cross-correlation of X-ray sources detected in the RASS with the optical cluster catalogues of Abell and Zwicky (Abell 1958; Zwicky et al. 1961–1968; Abell, Corwin & Olowin 1989), as well as systems detected as extended X-ray sources in the RASS and confirmed as clusters using the Palomar Observatory Sky Survey (POSS) and deep optical CCD imaging (Paper I). The latter, purely X-ray-selected systems are referred to in this paper by the *ROSAT* X-ray source name, e.g., RXJ0107.4 + 3227. (Any more commonly used names are referred to in the notes accompanying the tables.) We identified the dominant galaxies from comparison of the X-ray emission centroid and extent (using *ROSAT* pointed observations where possible rather than the limited information available from the RASS) against the POSS and maps provided by the Automated Plate Measuring Machine at Cambridge. Our previous work (A92; C95) showed that the BCG is usually found within 1–2 arcmin of the centroid of the X-ray emission from the cluster. Where there is no simple identification of a single dominant galaxy near the X-ray centroid, we aimed to observe all possible candidates, and in cases where the cluster is known or suspected to be part of a multiple cluster system (e.g., A2249, A2256), to observe both (or more) dominant galaxies. For detailed information about the best candidate dominant galaxies within a cluster, and for the positions of good candidates remaining unobserved due to lack of time, see the notes appended to the log of observations presented in Tables 1 and 2. In the course of compiling the BCS we have taken spectra of the BCGs in several clusters that were not included in the final sample. These extra clusters were selected from the RASS using exactly the same (original) criteria, but were eventually discarded due to their faint X-ray flux, low Galactic latitude or negative declination. As they are a natural extension to the BCS, we include their BCG spectra in this paper to enlarge our sample, but list them separately from the 'true' BCS in the log of observations (Table 2).

2.2 Previous data

Optical spectra of 88 dominant galaxies in 79 clusters have already been presented by us in A92 and C95. The majority of these observations were taken using the Faint Object Spectrograph (FOS) on the 2.5-m Isaac Newton Telescope (INT) on La Palma, with the primary aim of determining the redshift of BCS clusters. The FOS yields low-resolution spectra in two orders, with dispersion of 5.4 Å pixel^{-1} over 3500–5500 Å and 10.7 Å pixel^{-1} over 5000–10 500 Å, taken from a 6-arcsec-long slit. Observations were usually made at the parallactic angle to minimize the effects of atmospheric dispersion, and the slit width was matched to the seeing of typically around 1.2 arcsec FWHM. The FOS spectra were reduced using an automated optimal extraction package, and thus *spatially extended* spectral information is not available for these galaxies. The short slit length may also mean that the sky-subtraction is less accurate for the lower redshift galaxies. The final spectra were corrected for atmospheric extinction and Galactic reddening, and flux-calibrated. C95 also includes 10 spectra at moderate resolution (5 Å pixel^{-1}) taken using the Intermediate dispersion Spectroscopic and Imaging System on the William Herschel Telescope (WHT). All the previous spectra are included in the log of observations given in Tables 1 and 2, although the reader is referred to A92 and C95 for a more detailed account of the observations and data reduction. The reference for the paper containing the first publication of the spectrum is listed in the tenth column of Tables 1 and 2 (A92; White et al. 1994, hereafter W94; C95).

A92 contains an observation of what was thought to be the central cluster galaxy in the 'sub'-BCS cluster A2552. This $z = 0.128$ galaxy (at RA 23$^{\mathrm{h}}$ 11$^{\mathrm{m}}$ 31$^{\mathrm{s}}$.1, Dec. 03° 37′ 55″; J2000) had a peculiar spectrum, with narrow emission lines, curious line ratios and an exceptionally strong blue continuum with no obvious stellar absorption features. Subsequent optical imaging has since shown that this galaxy has a peculiar morphology, and is too bright to be the dominant galaxy for the surrounding cluster (Edge et al., in preparation). The best candidate for the dominant cluster galaxy is the double system at RA 23$^{\mathrm{h}}$ 11$^{\mathrm{m}}$ 33$^{\mathrm{s}}$.3, Dec. 03° 38′ 05″ (J2000), at a redshift of 0.3025 (Ebeling, private communication). Reconsideration of our noisy spectrum of another nearby galaxy at RA 23$^{\mathrm{h}}$ 11$^{\mathrm{m}}$ 33$^{\mathrm{s}}$.3 and Dec. 03° 38′ 05″ (J2000) gives a tentative redshift of $z = 0.306$; this galaxy was originally assigned a redshift of 0.137 in C95, based on an erroneous identification of [N II] emission.

Table 1. Log of the observations – clusters in the BCS.

Cluster		RA (J2000)	Dec. (J2000)	Redshift	Lines?	Exp (sec)	Airmass	$A(V)$ (mag)	p.a. (deg)	Ref	Notes
A7		00 11 45.2	32 24 57	0.1017	×	1000	1.096	0.374	272	D96	
A21	a (SE)	00 20 37.5	28 39 30	0.0967	×	1000	1.529	0.293	155†	D96	
	b (NW)	00 20 37.2	28 39 36	0.0966	×	″	″	″	″	″	
A76		00 39 55.9	06 50 55	0.0407	×	1000	2.194	0.258	62	D96	IC 1568
Z235		00 43 52.1	24 24 22	0.083	√					C95	
A115		00 55 50.5	26 24 39	0.1970	√	1000	2.065	0.363	70	D96	
RXJ0107.4+3227		01 07 24.9	32 24 46	0.0175	√	1000	1.004	0.359	316	D96	NGC 383
A168		01 14 57.5	00 25 52	0.0443	[×]	1000	1.904	0.226	234	D96	UGC797
RXJ0123.2+3327		01 23 11.6	33 27 36	0.0141	N	1000	1.512	0.349	259	D96	NGC 499
RXJ0123.6+3315		01 23 39.8	33 15 22	0.0169	×	1000	1.945	0.349	70	D96	NGC 507
A193		01 25 07.6	08 41 59	0.0484	[×]	1000	1.488	0.307	238	D96	UGC977
A267		01 52 41.9	01 00 27	0.230	×					C95	
A262		01 52 46.5	36 09 08	0.0166	√	1000	1.043	0.358	245	D96	NGC 708
A272		01 55 10.5	33 53 50	0.0898	×	1000	1.347	0.373	85	D96	
RXJ0228.2+2811		02 28 03.6	28 10 34	0.0351	×	1000	1.608	0.522	70	D96	IC 227
A376		02 46 04.0	36 54 21	0.0482	[×]	1000	1.960	0.449	255	D96	UGC2232
A400	a (N)	02 57 41.5	06 01 37	0.0238	N	1000	1.210	0.630	355†	D96	MCG+01-08-027
	b (S)	02 57 41.6	06 01 22	0.0253	N	″	″	″	″	″	″ ″
A399		02 57 53.1	13 01 52	0.0699	×	1000	1.296	0.727	259	D96	UGC2438
A401		02 58 57.8	13 34 59	0.0737	N	1000	1.382	0.700	243	D96	UGC2450
Z808		03 01 38.2	01 55 15	0.169	√					C95	
A407		03 01 51.5	35 50 30	0.0484	[×]	1000	1.668	0.820	79	D96	UGC2489
A409		03 03 21.1	01 55 34	0.153	×					C95	
RXJ0338.7+0958		03 38 40.5	09 58 12	0.0338	√	1000	1.387	1.187	331†	D96	
RXJ0341.3+1524		03 41 17.5	15 23 49	0.029	×					C95	
RXJ0352.9+1941		03 52 58.9	19 41 00	0.109	√				†	C95	
A478		04 13 25.3	10 27 56	0.086	√	1000	1.058	0.670	315	W94	
RXJ0419.6+0225		04 19 37.9	02 24 35	0.0133	×	1000	1.389	0.767	49	D96	NGC 1550
RXJ0439.0+0715		04 39 00.6	07 16 05	**0.2452**	×	1000	1.265	0.747	70	D96	
RXJ0439.0+0520		04 39 02.2	05 20 45	0.208	√					C95	
A520		04 54 03.8	02 53 33	(0.2024)	×	1000	2.161	0.520	240	D96	
A523		04 59 12.9	08 49 42	**0.1036**	×	1000	1.343	0.800	57	D96	
RXJ0503.1+0608		05 03 07.0	06 07 58	0.088	×					C95	
A566		07 04 28.6	63 18 41	0.0945	×	1000	1.224	0.348	344	D96	MCG+11-09-031
A576	a	07 21 21.5	55 48 40	0.0368	×	1000	1.123	0.381	7	D96	
	b	07 21 32.5	55 45 28	0.0408	×	1000	1.123	0.381	7	D96	MCG+09-12-061
A586		07 32 20.4	31 38 02	0.1702	×	1000	1.027	0.343	333	D96	
RXJ0740.9+5526		07 40 58.2	55 25 39	0.0340	×	1000	1.298	0.309	296	M95	UGC3957
RXJ0751.3+5012	a (S)	07 51 17.7	50 10 46	0.0218	×	1000	1.265	0.339	113	M95	UGC4051
	b (N:E)	07 51 21.1	50 14 10	0.0236	√	1000	1.268	0.339	265†	M95	UGC4052
	c (N:W)	07 51 18.8	50 14 07	0.0228	×	″	″	″	″	″	
A602	a (NW)	07 53 16.5	29 24 06	0.0601	×	1000	1.078	0.290	267	D96	
	b (SE)	07 53 26.4	29 21 35	0.0600	×	1000	1.048	0.290	267	D96	
RXJ0819.6+6336		08 19 25.7	63 37 28	**0.1186**	×	1000	1.371	0.272	305	M95	
A646		08 22 09.6	47 05 54	0.1268	√	1000	1.218	0.269	290	D96	
Z1665		08 23 21.7	04 22 22	**0.0311**	N	1000	1.100	0.182	351	D96	IC 505
A655		08 25 28.9	47 08 01	0.129	×	1000	1.153	0.266	300	M95	
A667		08 28 05.8	44 46 03	0.145	×					C95	
A671		08 28 31.5	30 25 54	0.051	N	1000	1.293	0.262	66	M95	IC 2378
A665		08 30 57.3	65 50 32	0.1824	×	1000	1.385	0.282	310	M95	
A689		08 37 24.6	14 58 22	0.2793	×					C95	
A697		08 42 57.5	36 22 01	0.282	×					C95	
A750		09 09 12.6	10 58 29	(0.177)	N	1000	1.184	0.253	66	M95	
A763		09 12 35.3	16 00 03	0.0892	×	1000	1.080	0.233	225	D96	
A757		09 13 07.8	47 42 32	0.0520	×	1000	1.058	0.109	175	D96	
A773	a (S)	09 17 53.4	51 43 39	0.216	×					C95	
	b (N)	09 17 53.5	51 44 03	0.224	×					C95	
A795		09 24 05.3	14 10 22	0.1355	√	1000	1.042	0.234	210	D96	
Z2701		09 52 49.2	51 53 06	0.215	√					C95	
Z2844		10 02 36.6	32 42 26	0.0502	×	1000	1.138	0.101	270	D96	
A961		10 16 23.0	33 38 19	0.124	×	1000	1.190	0.113	90	M98	
A963		10 17 03.6	39 02 51	0.2059	×	1000	1.038	0.093	232	D96	
A980		10 22 28.4	50 06 21	0.158	[×]	1000	1.144	0.070	128	M95	
Z3146		10 23 39.6	04 11 12	0.2906	√					A92	

Table 1 – *continued*

Cluster		RA (J2000)	Dec. (J2000)	Redshift	Lines?	Exp (sec)	Airmass	$A(V)$ (mag)	p.a. (deg)	Ref	
A990		10 23 39.8	49 08 39	0.142	×				†	C95	
Z3179		10 25 58.0	12 41 09	0.1432	√					A92	
A1033		10 31 44.3	35 02 30	0.1259	×					A92	
A1068		10 40 44.4	39 57 12	0.1386	√					A92	
A1132		10 58 23.5	56 47 43	0.1365	×	1000	1.141	0.042	166	M95	
A1177		11 09 44.4	21 45 34	0.0323	×	1000	1.008	0.077	113	M95	NGC 3551
A1185	a (N)	11 10 38.3	28 46 03	0.0348	×	1000	1.005	0.115	45	M95	NGC 3550
	b (S,NW)	11 10 42.9	28 41 36	0.0331	×	1000	1.027	0.115	332†	M95	NGC 3552
	c (S,SE)	11 10 47.9	28 39 37	0.0288	×	〃	〃	〃	〃	〃	NGC 3554
A1190		11 11 43.6	40 49 15	0.0772	×	1000	1.693	0.112	260	M95	
A1201		11 12 54.4	13 26 10	0.1679	[×]	1000	1.040	0.107	10	D96	
A1204		11 13 20.3	17 35 41	0.1706	√					A92	
A1246		11 23 58.8	21 28 48	0.1904	×					A92	
A1302		11 33 14.6	66 22 46	0.1148	×	1000	1.264	0.071	5	D96	
A1314		11 34 49.2	49 04 41	0.0337	×	1000	1.095	0.112	144	M95	IC 712
A1361		11 43 39.5	46 21 22	0.1167	√					A92	
A1366		11 44 36.7	67 24 20	0.1155	×	1000	1.281	0.090	0	M95	
A1413		11 55 17.8	23 24 20	0.1427	×	1000	1.005	0.146	180	M95	
A1423		11 57 17.2	33 36 41	0.213	×				†	C95	
A1437	a (N)	12 00 25.3	03 20 50	0.1336	×	1000	1.112	0.122	10	M95	
	b (S)	〃	〃	0.1315	×	〃	〃	〃	〃	〃	
Z4803		12 04 26.8	01 53 45	0.0194	×	1000	1.166	0.125	210	M95	NGC 4073
RXJ1205.1+3920		12 05 10.2	39 20 49	0.037	×					C95	
RXJ1206.5 + 2810		12 06 38.8	28 10 27	0.0281	√	1000	1.009	0.113	275†	D96	NGC 4104
Z4905		12 10 16.8	05 23 11	**0.0766**	N	1000	1.108	0.099	20	M95	
Z5029		12 17 41.0	03 39 23	0.0767	×	1000	1.110	0.115	190	M95	
RXJ1223.0 + 1037		12 23 06.6	10 37 17	0.0259	√	1000	1.625	0.149	300	D96	NGC 4325
A1553	a (NW)	12 30 43.3	10 34 44	0.1634	[×]	1000	1.272	0.133	303	D96	MCG + 02-32-109
	b (SE)	12 30 48.9	10 32 48	0.1715	[×]	1000	1.355	0.133	303	D96	
RXJ1230.7 + 1220		12 30 49.5	12 23 22	0.0036	√	500	1.271	0.163	240	M95	M87
Z5247		12 34 17.5	09 46 00	0.229	×	1000	1.140	0.125	220	M98	
A1589		12 41 17.4	18 34 30	0.0709	×	1000	1.018	0.127	180	M95	MCG + 03-32-083
A1656		12 59 35.6	27 57 35	0.0237	×	1000	1.010	0.061	262	M95	NGC 4874
A1668		13 03 46.6	19 16 18	0.0640	√	1000	1.014	0.147	180	M95	IC 4130
A1677		13 05 50.7	30 54 20	0.1845	×					A92	MCG + 05-31-128
A1682	a	13 06 45.7	46 33 31	0.2190	×					A92	
	b	13 06 49.8	46 33 35	0.2330	×					A92	
RXJ1320.1 + 3308	a (W)	13 20 14.6	33 08 39	0.0360	√	1000	1.016	0.070	250†	D96	NGC 5096
	b (E)	13 20 17.6	33 08 44	0.0377	×	〃	〃	〃	〃	〃	NGC 5098
RXJ1326.3 + 0013		13 26 17.6	00 13 17	**0.0821**	×	1000	1.403	0.122	230	M95	
A1758a		13 32 38.4	50 33 38	0.2792	×					A92	
A1763		13 35 20.1	41 00 05	0.2280	×	1000	1.023	0.061	3	M95	
A1767		13 36 08.1	59 12 24	0.0715	N	1000	1.160	0.119	180	M95	MCG + 10-19-096
A1775	a (SE)	13 41 50.5	26 22 15	0.0700	×	1000	1.004	0.070	123†	M95	UGC8669
	b (NW)	13 41 49.1	26 22 27	0.0758	×	〃	〃	〃	〃	〃	
A1773		13 42 09.6	02 13 39	0.0763	×	1000	1.140	0.118	200	M95	
A1795		13 48 52.5	26 35 37	0.062	√	1000	1.011	0.077	165†	M95	MCG + 05-33-005
A1800		13 49 23.5	28 06 27	0.0750	×	1000	1.000	0.080	330	M95	UGC8738
A1809		13 53 06.3	05 08 59	0.0796	×	1000	1.704	0.136	300	D96	
A1831		13 59 15.0	27 58 34	0.0760	×	1000	1.007	0.093	80	M95	MCG + 05-33-033
A1835		14 01 02.0	02 52 45	0.2523	√	1000	1.189	0.150	214	M95	
		〃	〃	〃	√					A92	
		〃	〃	〃	√	1000	1.111	0.155	180	M95	
A1885		14 13 43.6	43 39 45	0.090	√				†	C95	
Z6718		14 21 35.8	49 33 05	0.071	×					C95	
A1902		14 21 40.6	37 17 31	0.160	[×]					C95	
A1914		14 25 56.8	37 49 00	0.170	[×]	1000	1.023	0.064	238	M95	
A1918		14 25 22.5	63 11 55	0.139	×	1000	1.212	0.117	183	M98	
A1927		14 31 06.6	25 38 02	0.0967	×	1000	1.253	0.147	67	D96	
A1930		14 32 37.9	31 38 49	0.1316	√	1000	1.011	0.077	290	M95	
RXJ1440.6 + 0327	a (SE)	14 40 42.9	03 27 58	0.0274	×	1000	1.108	0.189	285†	M95	NGC 5718
	b (NW)	14 40 39.0	03 28 13	0.0268	×	〃	〃	〃	〃	〃	IC 1042
RXJ1442.2 + 2218		14 42 19.4	22 18 13	**0.0970**	√	1000	1.563	0.173	289	D96	UGC9480
A1978		14 51 09.5	14 36 45	**0.1468**	×	1000	1.031	0.118	2	M95	

Table 1 – *continued*

Cluster		RA (J2000)	Dec. (J2000)	Redshift	Lines?	Exp (sec)	Airmass	$A(V)$ (mag)	p.a. (deg)	Ref	Notes
A1983	a (S)	14 52 55.4	16 42 11	0.0442	[×]	1000	1.357	0.136	194†	D96	MCG + 03-38-044
	b (N)	14 52 57.0	16 43 40	0.0459	[×]	″	″	″	″	″	
A1991		14 54 31.4	18 38 34	0.0595	√	1000	1.020	0.163	148	M95	NGC 5778
Z7160		14 57 15.1	22 20 35	0.2578	√					A92	
A2009		15 00 19.6	21 22 11	0.1532	√	1000	1.023	0.221	46	M95	
A2034	a	15 10 10.2	33 34 03	0.115	×					C95	
	b	15 10 11.6	33 29 13	0.111	×					C95	
A2029		15 10 56.2	05 44 43	0.0786	×	1000	1.088	0.204	170	M95	IC 1101
A2033		15 11 26.6	06 20 58	0.078	N	1000	1.115	0.198	243	M95	UGC9756
A2050		15 16 18.0	00 05 22	0.118	×	1000	1.140	0.316	165	M98	
A2052		15 16 44.6	07 01 18	0.0351	√	1000	1.103	0.195	30	M95	UGC9799
A2055	a (SE)	15 18 45.8	06 13 57	0.1019	N	1000	1.087	0.214	286†	M95	
	b (SW)	15 18 40.7	06 14 19	0.1031	×	″	″	″	″	″	
	c (N)	15 18 45.0	06 16 28	0.1056	×	1000	1.112	0.214	210	M95	
A2064		15 20 52.2	48 39 40	0.0741	×	1000	1.538	0.123	269	D96	
A2061	a (S)	15 21 11.1	30 35 03	0.0753	×	1000	1.048	0.128	272	M95	MCG + 08-28-020
	b (N)	15 21 20.5	30 40 16	0.077	×	1000	1.002	0.128	242	M95	
RXJ1522.0 + 0741		15 21 51.9	07 42 32	0.0451	[×]	1000	1.115	0.202	115	M95	NGC 5920
A2065	a (W)	15 22 24.1	27 42 53	0.0698	×	1000	1.046	0.195	110†	M95	MCG + 05-36-020
	b	15 22 27.7	27 42 36	0.0710	×	″	″	″	″	″	
	c (E)	15 22 29.2	27 42 28	0.0749	×	″	″	″	″	″	
A2063		15 23 05.4	08 36 35	0.0342	×	1000	1.066	0.199	180	M95	MCG + 02-39-020
A2069	a (SE)	15 24 08.4	29 52 56	0.1138	×	1000	1.148	0.134	331†	M95	
	b (NW)	15 24 07.4	29 53 20	0.1098	×	″	″	″	″	″	
	c (NW)	″	″	0.1135	×	″	″	″	″	″	
A2072		15 25 48.7	18 14 11	**0.127**	√	1000	1.025	0.262	210	M95	
RXJ1532.9 + 3021		15 32 53.8	30 21 00	**0.3615**	√	1000	1.036	0.147	270	M95	
A2107		15 39 39.1	21 46 57	0.042	×	1000	1.021	0.298	230	M95	UGC9958
A2111	a (NW)	15 39 40.4	34 25 28	0.2317	×	1000	1.334	0.129	340	D96	
	b (SE)	15 39 41.8	34 24 44	0.2300	×	″	″	″	″	″	
A2110		15 39 50.8	30 43 05	0.0976	×	1000	1.004	0.159	180	M95	
A2124		15 44 59.1	36 06 35	0.0663	×	1000	1.035	0.118	297	M95	UGC10012
A2142	a (SE)	15 58 20.0	27 14 02	0.089	×	1000	1.044	0.262	301†	M95	
	b (NW)	15 58 13.3	27 14 55	0.095	×	″	″	″	″	″	
A2147		16 02 17.0	15 58 30	0.0357	×	1000	1.030	0.226	200	M95	UGC10143
A2151a		16 04 35.7	17 43 19	0.035	×	1000	1.115	0.227	240	M95	NGC 6041
RXJ1604.9 + 2356		16 04 56.6	23 55 58	0.0324	×	1000	1.024	0.330	63	M95	NGC 6051
A2175		16 20 31.2	29 53 29	0.0961	×	1000	1.041	0.166	270	M95	
A2199		16 28 38.5	39 33 05	0.031	√	1000	1.096	0.058	289	M95	NGC 6166
A2204		16 32 46.9	05 34 33	0.1514	√	1000	1.093	0.378	317†	M95	
A2219	a	16 40 12.9	46 42 43	0.2250	×					A92	
	b	16 40 19.6	46 42 43	0.2248	×					A92	
	c	16 40 21.9	46 42 48	0.2344	×					A92	
RXJ1657.8 + 2751		16 57 58.1	27 51 16	0.035	×	500	1.526	0.284	105	M98	NGC 6269
A2244		17 02 42.5	34 03 39	0.0980	×	500	1.012	0.134	310	M95	
A2256	a (SE)	17 03 35.6	78 37 46	0.0541	×	500	1.565	0.275	300†	M95	NGC 6331
	b (SE)	17 03 33.7	78 37 49	0.0565	×	″	″	″	″	″	″
	c (NW)	17 03 29.0	78 37 57	0.0599	×	″	″	″	″	″	
	d (E)	17 04 26.9	78 38 27	0.0596	×	1000	1.573	0.275	155	M95	MCG + 13-12-018
A2249		17 09 48.6	34 27 34	0.0873	×	1000	1.005	0.166	0	M95	
A2255	a (NE)	17 12 34.8	64 04 16	0.0845	×	1000	1.235	0.170	229†	M95	
	b (SW)	17 12 28.7	64 03 40	0.0750	×	″	″	″	″	″	
RXJ1715.3 + 5725		17 15 22.6	57 24 43	0.0282	√	1000	1.150	0.169	160	M95	NGC 6338
A2254		17 17 45.8	19 40 51	0.178	×					C95	
Z8197		17 18 11.8	56 39 56	**0.1140**	√	1000	1.132	0.176	0	M95	
A2259		17 20 09.6	27 40 09	0.164	[×]					C95	
RXJ1720.1 + 2638		17 20 10.1	26 37 32	0.1611	√	1000	1.001	0.262	0	M95	
A2261		17 22 27.2	32 07 58	0.224	×					C95	
A2294		17 24 11.3	85 53 13	0.178	√					C95	
RXJ1733.0 + 4345		17 33 02.1	43 45 35	**0.0331**	√	1000	1.036	0.164	190	M95	IC 1262
RXJ1740.5 + 3539	a (NE)	17 40 34.4	35 39 14	**0.0416**	×	1000	1.015	0.176	226†	M95	MCG + 06-39-010
	b (SW)	17 40 32.1	35 38 47	**0.0448**	[×]	″	″	″	″	″	MCG + 06-39-009
Z8276		17 44 14.5	32 59 30	0.075	√	1000	1.010	0.240	297	M95	
RXJ1750.2 + 3505		17 50 16.9	35 04 59	**0.1712**	√	1000	1.014	0.205	310	M95	

Table 1 – *continued*

Cluster		RA (J2000)	Dec. (J2000)	Redshift	Lines?	Exp (sec)	Airmass	$A(V)$ (mag)	p.a. (deg)	Ref	Notes
Z8338		18 11 05.2	49 54 34	0.047	×	600	1.629	0.284	90	M98	NGC 6582
A2318		19 05 11.0	78 05 38	0.1405	×					A92	
RXJ2114.1 + 0234		21 13 56.0	02 33 56	**0.0497**	×	700	2.579	0.437	60	D96	IC 1365
RXJ2129.6 + 0005		21 29 39.9	00 05 23	**0.2346**	√	1000	1.593	0.272	310	M95	
A2390		21 53 36.7	17 41 45	0.2328	√	1000	1.754	0.453	68	D96	
A2409		22 00 52.6	20 58 10	0.1470	×					A92	
A2443		22 26 08.0	17 21 25	0.1105	×	1000	2.157	0.349	65	D96	
A2457		22 35 40.9	01 29 07	0.0592	×	1000	1.913	0.383	60	D96	
A2495		22 50 19.6	10 54 13	0.0808	√	1000	1.759	0.353	60	D96	MCG + 02-58-021
Z8852		23 10 22.3	07 34 52	0.0399	×	600	2.510	0.325	60	D96	NGC 7499
A2572a	a (NE)	23 17 13.5	18 42 30	0.0400	×	1000	2.050	0.316	222	D96	NGC 7578B
	b (SW)	23 17 11.9	18 42 05	0.0400	×	″	″	″	″	″	NGC 7578A
A2572b		23 18 30.3	18 41 21	0.0370	×	1000	1.774	0.313	247	D96	NGC 7597
A2589		23 23 57.4	16 46 39	0.0407	×	1000	1.154	0.277	240	D96	NGC 7647
A2593		23 24 20.1	14 38 50	0.0423	×	600	2.409	0.279	65	D96	NGC 7649
A2626	a (NE)	23 36 30.7	21 08 49	0.0556	×	1000	1.383	0.289	212†	D96	IC 5338
	b (SW)	″	″	0.0552	√	″	″	″	″	″	
A2627	a (N)	23 36 42.1	23 55 30	0.127	N					C95	
	b (S)	23 36 42.5	23 54 46	0.122	N					C95	
A2634		23 38 29.3	27 01 53	0.0298	√	1000	1.253	0.338	257	D96	NGC 7720
A2657		23 44 57.3	09 11 36	0.0401	×	1000	1.123	0.377	220	D96	MCG + 01-60-030
A2665		23 50 50.6	06 09 00	0.0567	√	1000	1.712	0.409	60	D96	MCG + 01-60-039
A2675		23 55 42.6	11 20 35	0.0746	×	1000	2.211	0.321	65	D96	

Notes on individual entries in Tables 1 and 2:

A21 Two galaxies form a double system in the slit, separated in projection by 6.8 arcsec (16 kpc). Galaxy a (to the SE) is the brighter, but galaxy b has an asymmetric diffuse envelope (see Porter, Schneider & Hoessel 1991).

A115 The central cluster galaxy contains the radio source **3C 28**. The *ROSAT* HRI image of this cluster shows two components to the X-ray morphology, suggesting it to be a double cluster. The smaller component to the south is centred on a galaxy at RA $00^{h}\ 56^{m}\ 00^{s}$, Dec. $26^{\circ}\ 20'\ 37''$ (J2000), but we have taken a spectrum for 3C 28 at the centre of the main X-ray component.

RXJ0107.4 + 3227 This cluster is also known as the group **IV Zw 038**, and the galaxy observed (NGC 383) is associated with the radio source **3C31**. Colina & Perez-Fournon (1990) note a central dust lane in this galaxy.

A168 The observed galaxy is offset by 3–4 arcmin from the X-ray centroid, but the X-ray image of the cluster is broad with no tight core, and the galaxy observed is clearly the brightest cluster galaxy.

RXJ0123.2 + 3327 (NGC 499) and **RXJ0123.6 + 3315** (NGC 507) form a double system.

A262 The central cluster galaxy is known from ground-based images to be bifurcated by a central dust lane (Colina & Perez-Fournon 1990), which splits the galaxy continuum light in our slit into two components separated in projection by 1.6 arcsec (0.8 kpc). The line emission is spatially centred exactly on the dust lane separating these two components.

A272 We have taken a spectrum of the brightest dominant galaxy, although a second candidate dominant galaxy lies 2.4 arcmin to the N.

A400 The dominant galaxies are a dumbbell system separated by 16.2 arcsec (∼11 kpc) in projection, and are associated with the twin radio source **3C75**.

Z808 The observed galaxy is associated with the radio source **4C+01.06**.

A407 Several bright galaxies appear to be embedded in a diffuse optical halo within a region of diameter ∼60 kpc. We present the spectrum only of the brightest galaxy.

RXJ0338.7 + 0958 is the cluster 2A 0335 + 096.

RXJ0341.3 + 1524 The observed galaxy is catalogued as **III Zw 054**.

A520 This is a bimodal cluster, and we have observed the brightest (to the SW of the cluster) of three dominant galaxies. This cluster was detected in the *Einstein* Medium Sensitivity Survey (EMSS) (Stocke et al. 1991).

A566 is associated with the radio source **4C+63.10**.

A576 Galaxy b, the more southerly of the two dominant galaxies observed, is the more probable central cluster galaxy.

A586 Two galaxies lie on our slit, separated by only 5.1 arcsec (20 kpc) in projection. We present only the spectrum of the main galaxy to the NW of the two.

RXJ0751.3 + 5012 This cluster has a disturbed X-ray morphology. The three galaxies for which we have spectra are the bright more southerly galaxy (a) and both components of a dumbbell system to the north [galaxy b to the E and c to the W of the pair, separated in projection by 22.1 arcsec (15 kpc)].

A602 We have taken the spectrum of each of the two equally bright dominant galaxies in this double cluster.

A671 We have taken the spectrum only of the larger, brighter galaxy surrounded by diffuse optical emission, which we assume is the BCG. A second very bright dominant galaxy lies 3.1 arcmin to the SE.

A665 There is a second, less bright galaxy also within the slit, 10.6 arcsec (42 kpc) to the SE of the dominant galaxy. We present only the spectrum of the dominant galaxy.

A689 This galaxy was observed in C95, but the redshift given in that paper is wrong. The spectrum is very noisy, and shows a very blue galaxy with uncertain stellar absorption features. The new redshift has been determined by Ebeling, Henry & Mullis (1999), and is confirmed as the redshift of the cluster from spectra of two other galaxies. The X-ray source is coincident with a moderately bright radio source, which could contribute significantly to the X-ray flux of the total cluster emission.

A750 The cluster contains an AGN at the same redshift. There are two equally bright dominant galaxies, separated by 94 arcsec, but we only present a spectrum of the galaxy to the SE; the other lies at RA $09^{h}\ 09^{m}\ 07^{s}$, Dec $10^{\circ}\ 67'\ 51''$ (J2000). This cluster and the AGN were detected in the EMSS (Stocke et al. 1991).

A763 The identification of this source is confused. Our optical identification of the point-like object at the X-ray centroid (RA $09^{h}\ 12^{m}\ 31\overset{s}{.}0$, Dec. $15^{\circ}\ 55'\ 25''$;

J2000) is of a star, despite it being associated with a moderate, spatially extended radio source. The spectrum presented in this paper is of the dominant galaxy 4.7 arcmin to the N of this star which, despite being the nearest obvious BCG, is probably too far to be associated with the X-ray source.
A773 The two galaxies appear to be equally dominant.
RXJ1000.5 + 4409 Galaxy a is the more likely central dominant galaxy.
Z3179 There is an *IRAS*-detected, foreground ($z = 0.032$) spiral galaxy 110 arcsec to the NW of the observed galaxy.
A1023 Position of observed galaxy revised from A92.
A1035 The cluster is contaminated by a foreground group at $z = 0.067$ (Maurogordato et al. 1997).
A1185 This X-ray source is very extended. Galaxy a is the brightest of the three observed, and agrees with the X-ray centroid.
A1190 We have taken a spectrum only of the brighter of two nearby dominant galaxies, that to the SE of the pair; the radio source **4C+41.23** is associated with the other galaxy.
A1201 We have taken a spectrum of the galaxy closest to the X-ray centroid. A brighter galaxy to the SE probably belongs to a foreground cluster.
A1204 Note that the declination is incorrectly given in A92 as +11°.
A1361 The observed galaxy is associated with the radio source **4C+46.23**.
A1413 A second, smaller galaxy also lies on the slit, at a separation of only 9.5 arcsec (31 kpc) to the N. We present the spectrum only of the main galaxy. Maurogordato et al. (1997) note the presence of a small foreground group of galaxies at $z = 0.1$.
A1437 The main galaxy is close dumbbell, of separation 3.2 arcsec (10 kpc)
Z4803 This source is also catalogued as the poor group **MKW4**.
RXJ1206.5 + 2810 The observed galaxy (NGC 4104) is a double galaxy in the group **MKW4s**, the two components being separated by 2.8 arcsec (2.2 kpc). The emission-line system spans the two systems. The cluster is an EMSS source (Stocke et al. 1991).
Z4905 The observed galaxy has a very large and asymmetric halo on the POSS.
Z5029 The observed galaxy is not associated with the radio source **4C+04.41** which lies in this cluster.

2.3 New observations

The majority of the optical spectra presented in this paper were acquired during two-week-long runs during 1995 May 03 – 09 and 1996 December 29 – 1997 January 03. A further six galaxies were observed during service time on 1998 March 16 and 29. The observations were made using the Intermediate Dispersion Spectrograph (IDS) on the INT on La Palma, with the R150V grating on the 235-mm camera to yield an intermediate-resolution spectrum with a dispersion of 6.5 Å pixel^{-1}. In combination with the TEK3 CCD detector, the spectra covered the observed wavelength range 3300–9500 Å with a dispersion of 0.7 arcsec pixel^{-1} in the spatial direction. The weather was clear for nine of the 14 nights, with seeing conditions of typically 1.2 arcsec, varying between 1 and 1.5 arcsec. The long slit was set at a width of 1.3 arcsec and usually oriented at the parallactic angle, except where a more favourable orientation would include a second dominant galaxy in the same observation (those galaxies known to be observed with the slit *not* at parallactic angle are marked by a dagger in column 9 of Tables 1 and 2). Exposures were routinely 1000 s, and three or four observations of flux standards were made during each night with the slit opened up to 5.5 arcsec.

The data were reduced using standard procedures in the software package IRAF. After subtraction of a bias frame, the data were flat-fielded using a normalized flat created from long exposures of a tungsten lamp. Any spatial dispersion of the spectrum due to atmospheric refraction was corrected at this stage so that the continuum intensity peaked in the same row along the detector. The data were wavelength-calibrated using exposures of copper-argon and copper-neon arc-lamps, flux-calibrated, and corrected for atmospheric extinction. The Galactic reddening expected toward each galaxy was calculated from neutral hydrogen columns (Stark et al. 1992) using the formula of Bohlin, Savage & Drake (1978), and the spectra were corrected using the law of Cardelli, Clayton & Mathis (1989) by the amount listed in column 8 of Tables 1 and 2. The data were sky-subtracted using background regions selected to be well outside the galaxy extent, as determined from fitting spatial profiles of the galaxy continuum. The slit was sufficiently long to achieve good sky subtraction for all but M87, the dominant galaxy of the most nearby cluster in our sample, RXJ1230.7 + 1220 (Virgo). Although we also took short exposures of a nearby F8 star after each galaxy observation with the aim of removing atmospheric absorption features from the galaxy spectra, we eventually decided that such correction might introduce more uncertainty in the final emission-line fluxes. Thus we have not applied this correction, but throughout the paper we note where detection of an emission line will be affected by atmospheric absorption; the galaxies most affected are those in the redshift ranges $0.044 < z < 0.048$ and $0.158 < z < 0.170$.

2.4 Overview of observations

A full log of observations is presented in Tables 1 and 2. Observations of dominant galaxies in clusters from the BCS are presented first in Table 1, with the remainder listed in Table 2. 'Sub'-BCS clusters that fulfil all the BCS criteria *except* that the RASS flux falls below the threshold for inclusion [and lies in the range $(3.7 - 4.4) \times 10^{-12}$ erg cm^{-2} s^{-1}] are marked as such in the final column of Table 2, as are the clusters included in an X-ray-selected sample of Abell clusters (marked XBACS; Ebeling et al. 1996). Galaxies are identified by the name of their host cluster in column 1, with their individual catalogued names listed in the final column and notes to the table. Where more than one galaxy in a cluster is observed, each is labelled a, b with an indication of their relative position (north, south, etc.) following in brackets. Further elaboration on the properties of the individual galaxies (including if one is a better candidate for the dominant cluster galaxy) and their host clusters are given in the notes to the tables. The coordinates of the galaxy observed are given in columns 2 and 3, as measured to better than 1 arcsec from the Space Telescope Science Institute Digitized Sky Survey (DSS), and the galaxies are presented in RA order within each table. The redshift is given in column 4, and is in bold type if it is newly determined (see Section 3.1), and in brackets if uncertain due to insufficient signal-to-noise ratio in the spectrum. Column 5 shows whether or not the galaxy has optical Hα-line emission ($\times$ or $\surd$), or is marked by an 'N' if there is only [N II]$\lambda\lambda$6548,6584 line emission (see Section 3.3). Clusters marked by [$\times$] show no obvious line emission, but the expected Hα and [N II] complex falls within a region of atmospheric absorption, and we cannot completely rule out very low level [N II]$\lambda\lambda$6548,6584 emission in these cases. Columns 6–9 show the total exposure, airmass, magnitude of expected Galactic

Table 2. Log of the observations – clusters not included in either the BCS due to their faint X-ray flux, declination < 0, or low Galactic latitude.

Cluster		RA (J2000)	Dec. (J2000)	Redshift	Lines?	Exp (sec)	Airmass	$A(V)$ (mag)	p.a. (deg)	Ref	Notes
Z353		01 07 40.7	54 06 33	(0.109)	×					C95	low $\|b\|$
A291 †		02 01 43.1	–02 11 47	0.196	√					C95	
A531		05 01 16.3	–03 33 47	0.094	×					C95	
RXJ0510.7−0801		05 10 47.8	–08 01 44	0.217	×					C95	
Z1121		06 31 22.7	25 01 07	0.083	N					C95	low $\|b\|$, 3C162
Z1133		06 38 04.0	47 47 56	0.174	×					C95	low $\|b\|$
A611		08 00 56.7	36 03 25	0.288	N					C95	sub-BCS
A621		08 11 12.2	70 02 30	0.223	×					C95	sub-BCS
RXJ0821.0 + 0752		08 21 02.4	07 51 47	0.110	√				†	C95	sub-BCS
A761		09 10 35.9	–10 35 00	0.091	×					C95	XBACS
RXJ1000.5 + 4409	a	10 00 25.1	44 09 14	0.155	√					C95	
	b	10 00 31.1	44 08 44	0.153	√					C95	
A971		10 19 52.0	40 59 19	0.093	×				†	C95	sub-BCS
A1023		10 27 58.5	–06 47 56	0.1165	N					A92	
A1035		10 32 14.0	40 16 17	0.078	×	1000	1.120	0.093	110	M95	sub-BCS
A1045		10 35 00.1	30 41 39	0.1381	×					A92	sub-BCS
A1084		10 44 32.9	–07 04 08	0.1329	√					A92	XBACS
A1173		11 09 15.2	41 33 43	**0.0767**	×	1000	1.028	0.102	342	M95	sub-BCS
Z3916 †		11 14 21.9	58 23 20	0.204	√					C95	
Z4673		11 56 55.6	24 15 37	0.1419	×					A92	sub-BCS
Z5604		12 57 21.6	69 30 20	0.227	×					C95	
A1651		12 59 22.4	–04 11 44	0.0860	×					A92	XBACS
A1664		13 03 42.5	–24 14 41	0.1276	√					A92	XBACS
A1672		13 04 27.1	33 35 16	0.1882	×					A92	
A1703	a	13 15 05.1	51 49 04	0.2836	×					A92	
	b	13 15 11.0	51 49 04	0.2336	×					A92	
RXJ1449.5 + 2746 MCG + 05-35-018		14 49 27.9	27 46 51	0.0311	N	1000	1.723	0.133	287	D96	sub-BCS,
A2104		15 40 08.0	–03 18 16	0.1554	×					A92	XBACS
A2146		15 56 13.8	66 20 55	0.2343	√					A92	sub-BCS
Z7833		16 10 00.7	67 10 15	0.2136	×					A92	
A2187		16 24 13.9	41 14 38	0.1839	×					A92	sub-BCS
A2201		16 26 58.8	55 28 30	0.130	×					C95	
A2208		16 29 38.8	58 31 52	0.1329	×					A92	
A2228 redshift		16 48 00.8	29 56 59	0.1013	×					A92	Also AGN at same
Z8193		17 17 19.1	42 26 59	0.1754	√					A92	
A2292		17 57 06.7	53 51 38	0.119	√					C95	
Z8451		19 57 14.0	57 51 27	0.0884	×					A92	low $\|b\|$
Z8503		21 22 19.8	23 10 33	0.1430	×					A92	low $\|b\|$
A2426		22 14 31.5	–10 22 26	0.0990	×					A92	
A2428		22 16 15.6	–09 20 00	0.0846	×					A92	XBACS
A2631		23 37 41.1	00 17 06	0.278	×					C95	sub-BCS

Notes on individual entries in Tables 1 and 2 continued:

RXJ1223.0 + 1037 The observed galaxy (NGC 4325) may have nuclear activity, as the X-ray source is barely extended in archival PSPC data, although the line emission is quite muted. Alternatively, it could be an example of a highly focused cooling flow in a low-luminosity group.

A1553 We have taken the spectrum of each of the two equally dominant bright galaxies in this double cluster.

RXJ1230.7 + 1220 is M87 in the Virgo cluster, and associated with the radio source **3C274**.

A1656 This is the Coma cluster, and we have taken the spectrum only of the more western of the two dominant galaxies, NGC 4874 .

A1668 The measured redshift is significantly different from that in Rhee & Katgert (1988).

A1672 Position of observed galaxy revised from A92.

A1677 Previously noted in A92 as Z5694. Position revised from original.

A1682 The two galaxies are equally dominant.

A1703 Galaxy a is the more likely central dominant galaxy.

RXJ1320.1 + 3308 Two equally bright galaxies lie along our slit position, with a projected separation of 38.1 arcsec (38 kpc).

A1758 This double cluster has its two components listed separately in Paper I. We list here the dominant galaxy associated only with A1758a, which produces approximately 40 per cent of the combined luminosity; there is a bright less dominant galaxy also at RA $13^{h}\ 32^{m}\ 51^{s}.9$, Dec. $50°\ 31'\ 36''$ (J2000).

A1763 The observed galaxy is associated with the radio source **4C+41.26**.

A1775 The two dominant galaxies form a double system, separated in projection by 21.1 arcsec (∼40 kpc); they are associated with the radio source **4C+26.41**.

A1795 The observed galaxy is associated with the radio source **4C+26.42**.

A1831 The cluster shows a foreground cluster at $z = 0.062$ (Maurogordato et al. 1997).

A1835 We present three different observations of the same central cluster galaxy, one from A92, and two from our May observing run at slightly different position angles.

A1914 This is a complex binary cluster, and we have only taken a spectrum of the brighter (to the SW) of the two dominant galaxies. The radio source **4C+38.39** is probably a radio halo and hence not associated with the observed galaxy.

RXJ1440.6 + 0327 The source is also catalogued as the poor group **MKW8**, and the two galaxies observed are also catalogued as Arp 171. The galaxy (a) to the SE is probably the dominant galaxy; the two galaxies on the slit are separated in projection by 59.2 arcsec (44 kpc).
RXJ1449.5 + 2746 The observed galaxy is offset from the centroid of this relatively compact X-ray source, indicating that it may well be unrelated to the X-ray emission.
A1983 Two equally bright dominant galaxies lie along the slit position, separated by 92.6 arcsec (112 kpc).
Z7160 This cluster is the EMSS cluster MS1455+223 (Stocke et al. 1991).
A2009 The cluster contains the radio source **4C+21.44**, which is, however, unlikely to be associated with the observed galaxy.
A2034 Galaxy b is the more likely central dominant galaxy.
A2029 The observed galaxy is associated with the radio source **4C+06.53**.
A2033 There are two galaxies along the slit; we take the spectrum of the main galaxy to the NE as the central dominant galaxy. The galaxy 38 arcsec to the SW is a foreground AGN at a redshift of 0.038.
A2052 The observed galaxy is associated with **3C317**.
A2055 There are three equally bright dominant galaxies; a and b lie along the same slit position, separated in projection by 80 arcsec (200 kpc). None of these redshifts agrees with the previously published redshift of 0.053 in Struble & Rood (1991).
A2064 The redshift of the observed galaxy is inconsistent with the previously published redshift of 0.1074 from Owen, White & Thronson (1988), from which the cluster redshift has been derived. We find no evidence to support the previous redshift in our spectrum.
A2061 This bimodal cluster is highly extended. We have observed the two equally bright dominant galaxies either side of the X-ray centroid.
RXJ1522.0 + 0741 The source is also catalogued as the poor group **MKW3s**. The central galaxy (NGC 5920) is associated with the radio source **3C318.1**.
A2065 There are three galaxies along our chosen slit position; galaxy a is 52 arcsec to the NW, and galaxy c lies 21 arcsec to the SE of the much less bright galaxy b. Galaxies a and c are both dominant galaxies.
A2069 This cluster is particularly extended, and the X-ray centroid lies between two bright galaxies; one the central dominant galaxy in A2069 (galaxy a). Our spectrum of the second bright galaxy at RA $15^{\rm h}\,24^{\rm m}\,22\overset{\rm s}{.}7$ and Dec. $29^\circ\,57'\,25''$ (J2000) shows it to be a foreground active galaxy at a redshift of 0.076. This galaxy may be a weak contributor to the total X-ray emission from the cluster, and we note that its redshift suggests that it may be a outlying member of the nearby cluster A2061. Also, along our slit position for galaxy a are two other cluster galaxies (b and c) 26 arcsec to the NW of galaxy a, and separated from each other by only 4.1 arcsec (11 kpc). This cluster is an EMSS cluster.
A2072 The X-ray centroid is offset by $2.5'$ from the observed galaxy, which is the nearest obvious BCG.
A2111 This cluster has two equally dominant central galaxies, separated by 47 arcsec (220 kpc) in projection. The X-rays from this cluster are elongated (Wang, Ulmer & Lavery 1997).
A2142 We have taken the spectrum of each of the two equally bright dominant galaxies in this binary cluster. They lie along the same slit position, separated by 104 arcsec (238 kpc).
A2146 The emission-line ratios of the observed galaxy and a pointed X-ray observation of the cluster show that this galaxy contains an AGN (Allen 1995), but the deep *ROSAT* HRI image shows that the majority of the flux is from extended cluster gas.
A2151 This cluster is resolved into two components by the RASS because of its low redshift. We list here the dominant galaxy in A2151a, which produces 93 per cent of the combined luminosity of the system.
RXJ1604.9 + 2356 The source is also catalogued as the poor group **AWM4**. The observed galaxy is associated with the radio source **4C+24.36**.
A2199 The observed galaxy (NGC 6166) is associated with **3C338**.
A2204 Two galaxies lie along our slit position, separated by 4 arcsec (14 kpc). The galaxy to the SE has the strong extended line emission associated with it, and we present the spectrum of only this galaxy.
A2219 Galaxy b is the most likely central dominant galaxy.
A2228 The X-ray flux and centroid of the cluster source is likely to be significantly affected by the presence of an AGN within, but not at the centre of the cluster (see A92).
RXJ1657.8 + 2751 This source is also catalogued as the poor group AWM5.
A2256 This cluster is a well-known binary system. Galaxies a and b form a common system, separated by 6.6 arcsec (∼10 kpc), and galaxy c is 19 arcsec further to the NW along this slit. Galaxy d is a bright dominant galaxy to the E of galaxies a, b and c, and the best candidate for a single central cluster galaxy.
A2249 This cluster is a binary system and relatively extended in the X-ray. We have only taken a spectrum of one of the two dominant giant elliptical galaxies (the more eastern), as it is in better agreement with the X-ray centroid. The cluster is associated with the radio source **4C+34.45**.
A2255 This cluster has two dominant galaxies separated by 53.7 arcsec (109 kpc); each of these galaxies appears to be a very close dumbbell in its own right.
RXJ1733.0 + 4345 The observed galaxy (IC 1262) is associated with **4C+43.46**.
RXJ1740.5 + 3539 Two dominant galaxies lie along this slit position, separated by 38.9 arcsec (∼45 kpc); galaxy b looks from the POSS to be the more likely candidate for the central cluster galaxy.
Z8276 is an uncatalogued radio-loud galaxy.
Z8338 This cluster has two close central galaxies; we observed the brighter to the east of the pair.
A2318 The X-ray centroid is offset from the galaxy observed, but note that the galaxy position given in A92 is in error. There is a Seyfert 1 galaxy coincident with the X-ray centroid at the redshift of the cluster, $z = 0.14$ (Edge, private communication), so this source is significantly contaminated.
RXJ2114.1 + 0234 The observed galaxy (IC 1365) has an asymmetric optical halo on the POSS image, and is contained in the poor group **II Zw 108**.
A2443 The cluster contains two dominant galaxies. We have only taken a spectrum of the brighter galaxy, which is a better candidate for the BCG. ; the other lies 2 arcmin to the NW. This fainter galaxy is associated with **4C+17.89**.
Z8852 This highly extended X-ray source is the Pegasus Group. The centre is occupied by two equally dominant galaxies: we have observed NGC 7499, and the other central galaxy NGC 7503 (which we did not observe) is associated with the radio source **4C+07.61**. NGC 7499 is closer to the X-ray emission centroid.
A2572a This source is also catalogued as the compact group Hickson 94. There are two galaxies along our slit, separated in projection by 33.7 arcsec (37 kpc). Galaxy a is the brighter, but galaxy b is embedded in an asymmetric optical halo on the POSS.
A2572b There is a second, higher redshift cluster in the background of A2572b that may contribute to the total X-ray flux measured from this cluster (Ebeling, Mendes de Oliveira & White 1995).
A2626 This cluster has two close galaxies separated by 3.4 arcsec (5 kpc), embedded in an asymmetric halo extended to the SW component. Galaxy b (SW) has line emission, and is associated with the radio source **3C464**.
A2627 The two galaxies observed appear equally dominant.
A2634 The observed galaxy (NGC 7720) is associated with **3C465**.

Table 3. Clusters in the BCS for which we do not have a spectrum of the central cluster galaxy.

Cluster		RA (J2000)	Dec. (J2000)	Redshift	Lines?	Ref	Notes
RXJ0000.1 + 0816		00 00 07.1	08 16 49	0.040	√	EHM99	UGC12890
RXJ0021.6 + 2803	(S)	00 21 36.9	28 03 04	0.094	×	EHM99	IV Zw 015
	(E)	00 21 44.0	28 03 56	0.094	×	EHM99	
A68	a (SE)	00 37 06.8	09 09 25	0.250	×	EHM99	
	b (NW)	00 37 04.9	09 09 47	0.259	×	EHM99	
A75	a (W)	00 39 28.5	21 13 48	0.062	–	SR91	cluster redshift
	b (E)	00 39 42.3	21 14 06	0.058	×	OLK95	MCG + 03-02-021
A77		00 40 28.2	29 33 22	0.071	×	OLK95	UGC428, EMSS
A84	a (SE)	00 41 54.9	21 22 37	0.103	–	SR91	cluster redshift
	b (NW)	00 41 41.3	21 24 10	0.102	×	OWT88	4C+21.05
A104		00 49 49.8	24 27 03	0.082	–	SR91	cluster redshift
RXJ0058.9 + 2657		00 58 22.7	26 51 57	0.048	×	DC95	NGC 326, 4C + 26.03
A147		01 08 12.0	02 11 39	0.042	×	P78	UGC701
A160		01 12 59.6	15 29 28	0.044	×	OLK95	MCG + 02-04-010
A189		01 25 31.3	01 45 34	0.019	×	S78	NGC 533, EMSS
Z1261		07 16 41.1	53 23 10	0.064	×	GB82	4C + 53.16
Z1478	a	07 59 44.3	53 58 57	0.104	×	EHM99	
	b	07 59 41.0	54 00 11	0.104	×	EHM99	
	c	07 59 39.2	54 00 54	0.104	×	EHM99	
Z1953		08 50 07.2	36 04 13.1	0.374	×	EHM99	
Z2089	a	09 00 36.8	20 53 43	0.235	√	EHM99	
	b	09 00 40.1	20 54 35	0.235	×	EHM99	
	c	09 00 36.6	20 53 43	0.235	×	EHM99	
A781	a	09 20 25.1	30 31 33	0.304	×	EHM99	
	b	09 20 25.6	30 29 40	0.293	×	EHM99	
RXJ1053.7 + 5450		10 53 36.6	54 52 06	0.070	×	EHM99	
A1235		11 23 15.6	19 35 53	0.104	–	SR91	cluster redshift
A1367		11 45 05.0	19 36 23	0.021	√	OLK	
A2108	a	15 40 15.9	17 52 30	0.092	–	SR91	cluster redshift
	b	15 40 18.9	17 51 25	0.092	–	SR91	cluster redshift
	c	15 40 17.9	17 53 05	0.092	–	SR91	cluster redshift
A2218		16 35 49.1	66 12 45	0.172	×	LPS92	
RXJ1651.1 + 0459		16 51 08.1	04 59 35	0.154	√	T93	Her-A, 3C348, MCG + 01-43-006
A2241		16 59 43.9	32 36 56	0.0984	×	U76	PGC59392
A2312		18 54 06.1	68 22 57	0.095	×	M97	
RXJ2214.7 + 1350		22 14 47.0	13 50 28	0.026	√	LM89	NGC 7237, 3C442
A2622		23 35 01.4	27 22 22	0.061	×	OLK95	
Z9077		23 50 35.4	29 29 40	0.095	√	DSG92	EMSS

References: DC95 Davoust & Considere 1995; DSG92 Donahue et al. 1992; EHM99 Ebeling, Henry & Mullis, in preparation; GB82 Gregory & Burns 1982; LM89 Laurikainen & Moles 1989; LPS92 Le Borgne, Pello & Sanahuja 1992; M97 Maurogordato et al. 1997; OLK95 Owen et al. 1995; OWT88 Owen et al. 1988; P78 Peterson 1978; S78 Sandage 1978; SR91 Struble & Rood 1991; T93 Tadhunter et al. 1993; U76 Ulrich 1976.

Notes on individual entries in Table 3:

There are five dominant galaxies with no redshift in the literature. The position of that galaxy is given but the redshift of the cluster is tabulated.

RXJ0001.6 + 0816 The central galaxy shows [N II] and [S II] line emission (EHM99).

RXJ0021.6 + 2803 Galaxy a is the BCG.

RXJ0058.9 + 2657 The central galaxy (NGC 326) is a dumbbell galaxy.

A68 Galaxy a is the brighter galaxy, nearer the RASS centroid.

A75 Galaxy a is the more likely BCG, but is very close to a bright star, making a observation difficult. Galaxy b is the radio galaxy 0037+209 (Owen et al. 1995).

A77 This galaxy contains the radio source 0037 + 292 (Owen et al. 1995).

A84 Galaxy a is the better candidate for the BCG. The redshift for galaxy b quoted by O'Dea & Owen (1985) is from Owen & White (in preparation), for which we can find no subsequent reference.

A104 Owen et al. 1995 showed that another galaxy in the cluster (harbouring the radio source 0047+241) and west of the dominant one listed in Table 3, at RA $00^{h}\ 49^{m}\ 41\overset{s}{.}8$, Dec. $+24°\ 26'\ 42''$ (J2000) has Hα + [N II] emission, but no [O II]λ3727 emission.

Z1478 None of the galaxies listed in Table 3 is the central dominant galaxy, which lies almost exactly behind a star, at RA $07^{h}\ 59^{m}\ 40\overset{s}{.}4$, Dec. $+54°\ 00'\ 22''$ (J2000).

Z1953 HRI observations of this cluster suggest that as much as two-thirds of the X-ray flux assigned to this system based on the RASS observation are in fact due to two X-ray point sources within 7 arcmin of the cluster (Ebeling, private communication).

Z2089 Galaxy (a) at the X-ray centroid has strong line emission with the line ratios ([N II]/Hα and [O III]/Hβ) suggestive of an AGN. The X-ray source is clearly resolved in a recent *ROSAT* HRI image, supporting its inclusion as a cluster in the BCS.

A781 A third galaxy at RA $09^{h}\ 20^{m}\ 22\overset{s}{.}3$, Dec. $30°\ 30'\ 53''$ (J2000) shows Hα in emission, but is foreground at a redshift of 0.126 (Ebeling, Henry & Mullis, in preparation). It is not clear whether galaxy a or b is the BCG, although b is brighter.

RXJ1053.7 + 5450 The observed galaxy is to the NW of a very extended X-ray source. There are several other slightly fainter galaxies the SE.

A1367 The BCG is NGC 3862, which is associated with the strong radio source **3C264**, and detected as an unresolved point source in *ROSAT* images

contributing approximately 5 per cent to the total X-ray emission from the cluster (Edge & Röttgering 1995). NGC 3862 is significantly offset from the centre of the highly extended X-ray emission, and is observed to have a weak emission line spectrum ([N II]>Hα, weak [O II]) with evidence for a blue continuum. *HST* observations reveal that 3C264 contains a non-thermal core and jet (Baum et al. 1998), which could contribute to this blue continuum. We have observed the galaxy NGC 3860 at RA $11^{h}\ 44^{m}\ 49\overset{s}{.}1$, Dec. $19°\ 47'\ 44''$ (J2000), which is the brightest galaxy in the broad cluster core. NGC 3860 has strong extended line emission, dominated by Hα.

A2108 There are three galaxies of equal rank in the core of this cluster.

RXJ1651.1 + 0459 Hercules A has moderate [O II]λ3727 and weak [O III]λ5007 ([O III]/[O II] = 0.2) emitted by one of two diffuse continuum components separated by 3 arcsec (10.5 kpc; Tadhunter et al. 1993).

A2241 This optical position and redshift of this cluster are confused in the literature; A2241 appears to be a superposition of an X-ray-bright cluster at $z \sim 0.1$ and an X-ray faint group at $z \sim 0.06$. The X-ray-bright cluster detected by *ROSAT* is clearly centred on PGC 59392 at a redshift $z = 0.0984$, which is also associated with the radio source **4C32.52C**. The galaxies at $z \sim 0.06$ are more than 10 arcmin from the X-ray peak, and form a separate system not detected by the RASS.

RXJ2214.7 + 1350 The cluster has two central galaxies (NGC 7236/7) sharing a disturbed halo.

Z9077 This source is an EMSS cluster, MS 2348.0+2913 (Stocke et al. 1991). The central galaxy has Hα +[N II] emission at a flux of $(2.6 \pm 2.6) \times 10^{-15}$ erg cm^{-2} s^{-1} discovered from narrow-band imaging by Donahue et al. (1992).

reddening and slit position angle respectively for the new observations. A † in column 9 marks an observation where the position angle of the slit is known not to be at the parallactic angle. Column 10 gives either the run of the new IDS observations (M95 for 1995 May, D96 for 1996 December, M98 for 1998 March) or the reference for the first publication of the spectrum (A92, W94 or C95; see Section 2.2).

2.5 Supplementary data from the literature

27 clusters remain for which we have not observed the BCG, and these are listed in Table 3. The identification of the possible BCG for each cluster has been made by us from comparison of the X-ray properties with the digitized POSS in the same way as for the observed galaxies; the notes accompanying the table indicate which of the galaxies listed could be the BCG. Eight clusters have galaxies observed by Ebeling, Henry & Mullis (in preparation), and we have used NED to search the literature for basic information (i.e., whether the BCG has optical emission lines or not) on the remainder. Only five clusters remain for which we do not have any spectral information for the BCG (A75, A84, A104, A1235 and A2108). In Table 3 we list the cluster name, galaxy coordinates and redshift in columns 1–4 respectively. Where possible we list the redshift of the individual galaxy if known from the literature; otherwise we list the cluster redshift and mark it as such in the final column. Whether or not the galaxy is known to have Hα-line emission is marked in column 5, with a reference to the source for the redshift (and emission-line properties) in column 6. Individual names are given in the final column, with more detailed information in the notes to the table.

3 DATA ANALYSIS AND RESULTS

3.1 New redshifts

We have obtained a total of 17 new cluster redshifts for the BCS, which are listed with a redshift marked in bold font in Tables 1 and 2 (the redshift of the cluster is assumed the same as that of its BCG). The redshifts were determined using the cross-correlation technique detailed in A92 and C95. We have compared the redshifts we have derived for our whole sample to all those available in the literature, and find that errors in our redshift are typically less than ± 0.0005. The only exceptions are those spectra taken on the fourth night in the 1995 May run, which have a less precise wavelength calibration; these redshifts are quoted to within ± 0.001. One new X-ray discovered cluster (RXJ1532.9+3021) was discovered to have a redshift of 0.3615, the second highest in the BCS.

3.2 Completeness of sample

Combining both the new observations presented here and those observations from A92 and C95, we have compiled a total spectral sample of 256 dominant galaxies in 215 clusters. 213 of these spectra are of dominant galaxies in 177 clusters of the BCS, leading to a completeness in coverage of 87 per cent for this sample. With the sole exception of 3C264 in A1367, we have spectra for all the BCGs in the BCS down to an unabsorbed X-ray flux limit of 7.9×10^{-12} erg cm^{-2} s^{-1} (98 clusters); this limit corresponds to a luminosity of 3.6×10^{44} erg s^{-1} at $z = 0.1$, 1.5×10^{45} erg s^{-1} at $z = 0.2$, and 3.5×10^{45} erg s^{-1} at $z = 0.3$ (in the *ROSAT* 0.1–2.4 keV band). [We have basic information on whether a BCG has an emission-line spectrum or not down to an X-ray flux of 7.1×10^{-12} erg cm^{-2} s^{-1} (109 clusters).] Fig. 1 shows the redshift distribution for all clusters in the BCS, and the distribution of those for which we have optical spectra; for redshift bins at $z < 0.25$ we have spectra of over 83 per cent of the BCS BCGs.

3.3 Occurrence of line emission

Many of the spectra show strong low-ionization emission lines commonly observed in central cluster galaxies (e.g. Heckman 1981; Hu et al. 1985; JFN; Heckman et al. 1989; A92; C95). The major coolants are hydrogen and oxygen, and lines of nitrogen and sulphur are also strong. We have marked which galaxies show such line emission by a tick ($\surd$) in column 5 of Tables 1 and 2. We determine whether or not a galaxy has line emission if the lines of [N II]$\lambda\lambda$6548,6584 (the most common coolant) can be fitted at the redshift of the galaxy, at an intensity significantly (3σ) above the noise in the galaxy continuum. As we are sampling down to lower values of X-ray luminosity than in A92 and C95, we also find a population of galaxies that show only low-level [N II]$\lambda\lambda$6548,6584 line emission with Hα in absorption. These galaxies are marked separately in column 5 of Tables 1 and 2 by an 'N'. We show the slit spectrum of all the line emitters with $L(\mathrm{H}\alpha) > 10^{40}$ erg s^{-1} in Fig. 2, including for completeness those from A92 and C95. The spectra are presented in descending order of the observed Hα luminosity (i.e., *not* corrected for any internal reddening as detailed in Section 3.9). Some of the galaxy spectra have been smoothed with a box 3 pixels wide (these are noted in the title of each plot). Fig. 3 shows three examples of the galaxies that feature only [N II] line emission. We determine a flux limit for the detection of Hα emission by investigating the redshift-dependence of the fitted Hα luminosity. We find that below a redshift of 0.05, a systematic uncertainty in the level of stellar Hα absorption expected from the underlying galaxy continuum dominates our detection level,

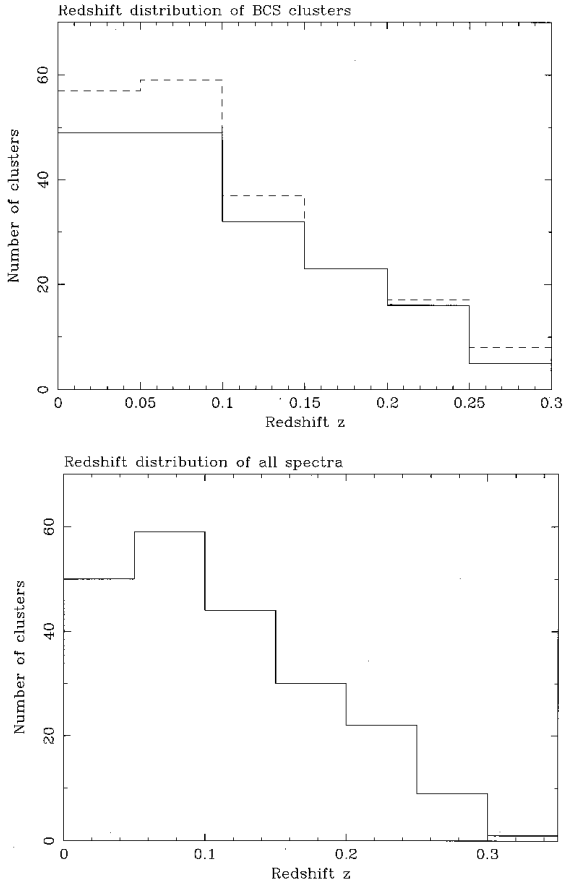

Figure 1. (Top) The redshift distribution of the 201 $z < 0.3$ clusters in the BCS (dashed line) and of those clusters in the BCS for which we have spectra (solid line). (Bottom) The redshift distribution of all the clusters for which we have spectra, i.e., all those in Tables 1 and 2.

leading to an upper limit to Hα of $\sim 4 \times 10^{39}$ erg s^{-1}. Beyond this redshift, we find the detection limit to rise according to the expected $L \propto z^2$ relation. We fit this slope at what we estimate to be the least significant detection of Hα in emission in a galaxy at $z > 0.05$, and extrapolate to obtain Hα luminosity limits of 1.9×10^{40}, 7.8×10^{40} and 1.8×10^{41} erg s^{-1} at redshifts of 0.1, 0.2 and 0.3 respectively.

Taking the 203 members of the BCS sample (excluding the 'b' components of the A2572, A2151 and A1758 clusters and including the two clusters at $z > 0.3$), 32±5 per cent show some level of line emission (i.e., including those with only [N II] and no Hα), and 27±4 per cent show Hα in emission; we assume that the five clusters for which the emission-line properties of the BCG are not known are *not* line emitters, and obtain the errors assuming that $\sqrt{n}$ statistics are applicable. The fractions of line emitters are similar if we include all the galaxies from Table 2 that are not *bona fide* members of the BCS, at 34±5 and 27±4 per cent for all emitters and Hα-only emitters respectively.

Fig. 4 shows the frequency of line emitters as a function of the X-ray luminosity (L_X is taken from Paper I) for all the BCS sample, and then for all clusters included in this paper for which we have an X-ray flux (i.e., including those in Table 2 that are in the sub-BCS and XBACS). The data have been grouped so as to contain an equal number (45–50) of clusters per luminosity bin. In both samples there is no compelling evidence for an increase in the frequency of line emission with X-ray luminosity, the distribution in each case being consistent with a constant fraction around 31.5±4 per cent (including 6 per cent with [N II]-only line emission).

Fig. 5 shows the frequency of line emitters as a function of redshift, both for the BCS and for all the clusters in this paper. We have grouped the sample into an equal number of clusters per redshift bin (50), and again assume that the five clusters whose BCG optical properties are not known are not line emitters. Both samples show the fraction to be high in the lowest redshift bin; assuming that the galaxy line luminosity is correlated with the cluster X-ray luminosity, the threshold for detecting line emitters will be lower at low redshift. The frequency of line emission drops sharply at a redshift of 0.07, and then climbs back up to a fraction above 30 per cent above a redshift $z > 0.1$. The BCS X-ray flux limit pre-selects the most luminous clusters at any epoch, and by a redshift of 0.2 will include only those clusters whose X-ray luminosity is boosted by the presence of a massive cooling flow (which would enhance the probability of line emission), or because it is a binary cluster system whose X-ray emission has been enhanced because it is blended (and such systems usually do not have cooling flows). Fig. 4, however, indicates that the fraction of line emitters is not dependent on X-ray luminosity, so the rise in the fraction of line emitters with redshift may reflect a real increase in the number of sites promoting line emission at $z > 0.1$. To test this, we looked at the 10 clusters in the complete (i.e., $z < 0.3$) BCS that have an X-ray luminosity above 1.8×10^{45} erg s^{-1}, which corresponds to the flux limit of 4.4×10^{-12} erg cm^{-2} s^{-1} at the redshift of the furthest cluster in the sample ($z = 0.29$). Only one of the five clusters with a redshift $z < 0.23$ has line emission in the central galaxy, whereas four out of the five at $0.23 < z < 0.29$ do. Dropping the X-ray luminosity cut-off to 1×10^{45} erg s^{-1}, however, results in equal numbers of line emitters in the 17 clusters below and 16 clusters above 0.23. Thus any evidence for evolution in the frequency of occurrence of line emission (and thus presumably massive cooling flows) with redshift (e.g., Donahue et al. 1992) is only very tentative, and can involve only the most luminous clusters.

Whilst a cooling flow is not the only possible cause of line emission around a BCG, all but five of the 64 Hα-emitting central galaxies (those in A1068, A2089, A2146, A2294 and RXJ0821.0+0752; see Section 3.7 and notes to the tables) have line intensity ratios consistent with the nebulae seen around the central cluster galaxies of known cooling flows. Removing these five exceptions from consideration decreases the overall frequency of line emission by only 2 per cent in either the BCS, or all clusters for which we have spectra.

We find, however, a higher probability that a purely X-ray-selected cluster will contain an emission-line system around its BCG. Of the 39 'RXJ' BCS clusters listed in Tables 1 and 3, 19 have a BCG with line emission and 19 do not, and only one has [N II]-only emission. Including also the 'RXJ' clusters in Table 2, 20 out of the 43 show Hα in emission, with only two [N II]-only emitters. The fraction of line emitters is significantly greater in the 'RXJ' clusters than in the sample as a whole. This is not simply a selection of the RXJ systems being at lower redshift, and thus line emission being easier to detect in the central cluster galaxy. Of the 29 Abell and 31 RXJ clusters at $z < 0.05$ in Tables 1 and 3, only five (and a sole [N II]-only emitter) of the central galaxies in the Abell clusters show line emission; 16 (plus two [N II]-only emitters) of the RXJ systems have line emission. Assuming that the emission-line nebulae are (nearly) all tracing the presence of a cooling flow in these clusters, this suggests that the X-ray-selected clusters contain a higher fraction of cooling flows. This is most likely due to not only

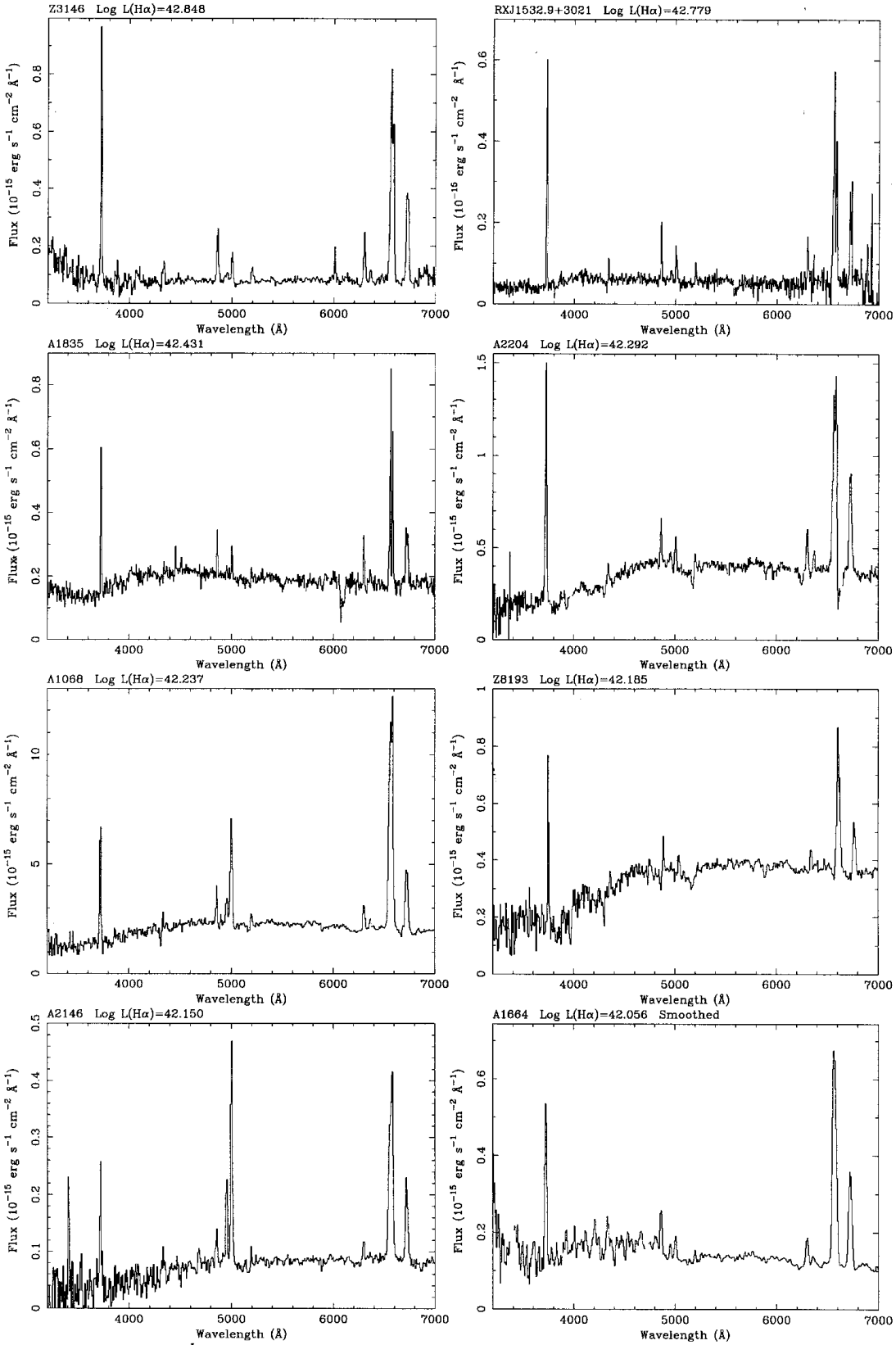

Figure 2. The spectra of line-emitting central cluster galaxies in descending order of the observed Hα luminosity – the brightest line emitters with log L(Hα) from 42.9 to 42.05. Some of the spectra have been smoothed (as noted in the title for each), and cosmic ray hits have been removed.

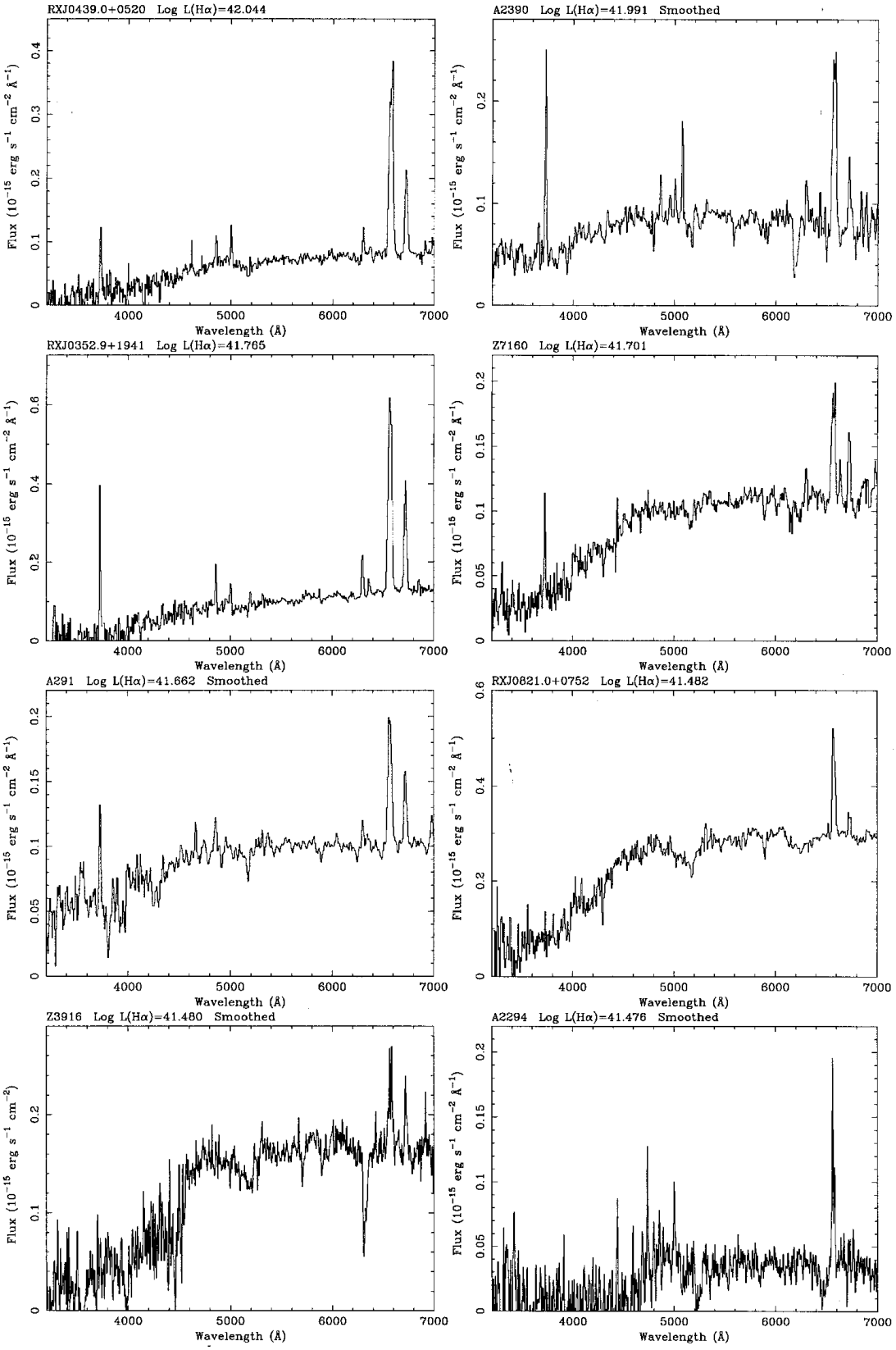

Figure 2 – *continued.* The spectra of line-emitting central cluster galaxies with log L(Hα) in the range 42.05–41.47.

the fact that the RASS X-ray detection algorithm used to construct the BCS is most sensitive to point or peaked X-ray sources (Paper I), but also that cooling flows may enhance the X-ray luminosity of a cluster (Allen & Fabian 1998). Thus the X-ray-selected samples will preferentially contain cooling flow clusters (see also Pesce et al. 1990).

Only 36 of the 59 Hα-line emitters show significant [O II]λ3727 line emission, although this fraction of 61 ± 13 per cent should be

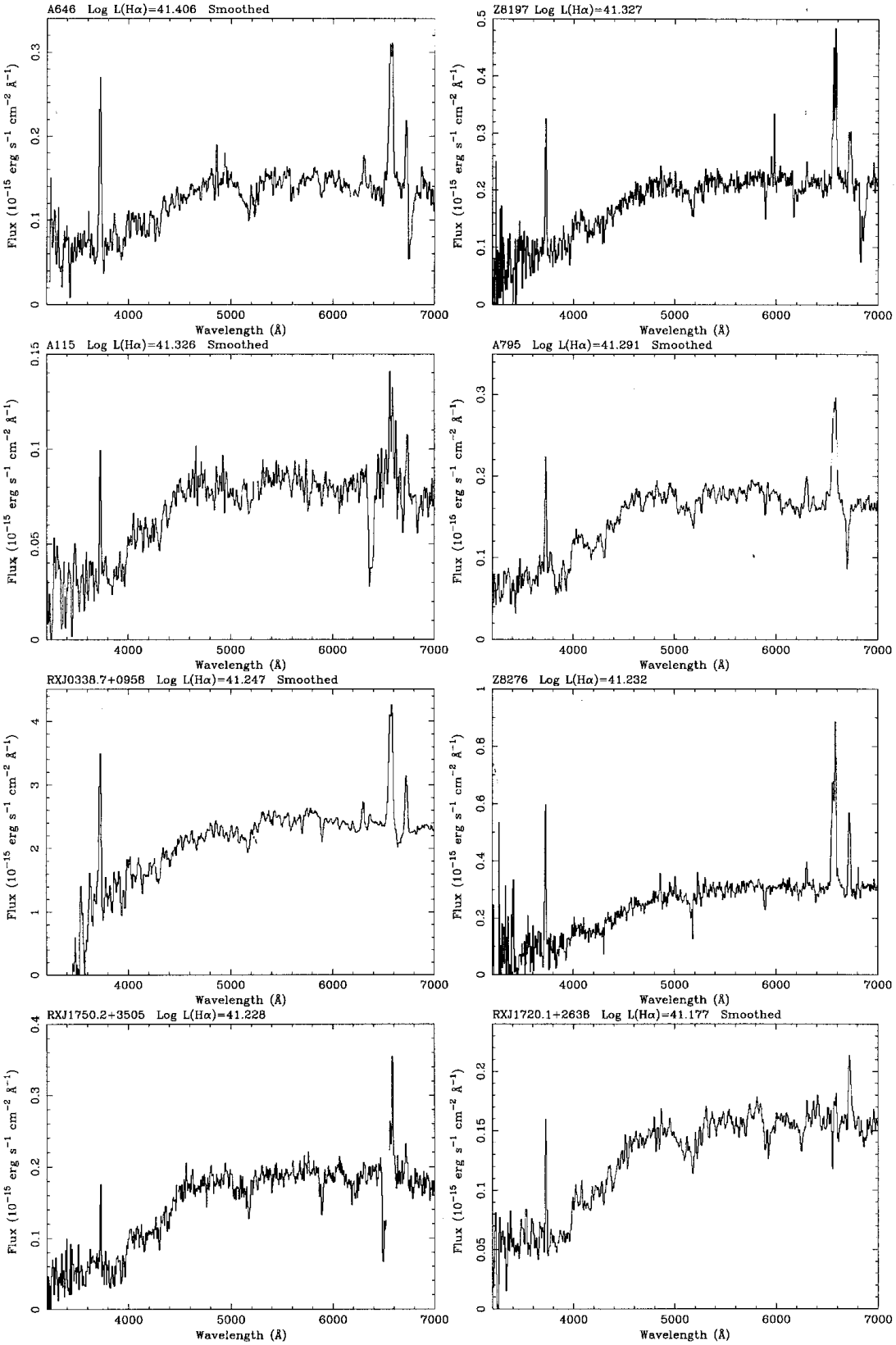

Figure 2 – *continued.* The spectra of line-emitting central cluster galaxies with log L(Hα) in the range 41.41–41.17.

regarded as a lower limit to the true fraction. Detectability of [O II] will be affected both by any dust intrinsic to the galaxy (see Section 3.9), and by atmospheric refraction, given that the slit placement is decided on the red galaxy image.

3.4 Comparison of X-ray and optical centroids

We have calculated the projected separation between the X-ray centroid of each cluster detection in the RASS (from Paper I) and

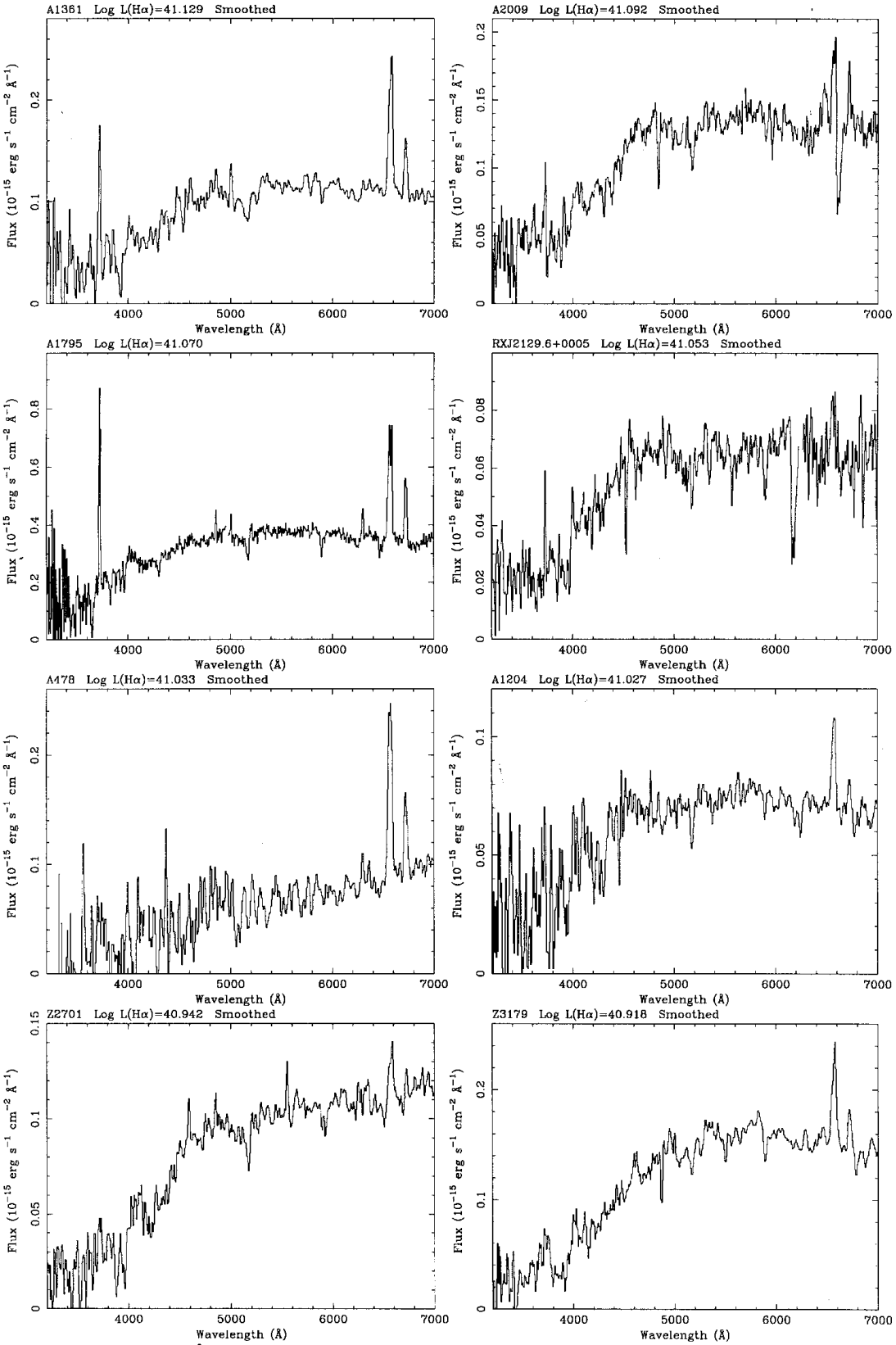

Figure 2 – *continued.* The spectra of line-emitting central cluster galaxies with log $L(\mathrm{H}\alpha)$ in the range 41.13–40.91.

the optical position of its BCG. Where identification of a single dominant galaxy is not obvious, we have used the coordinates of the galaxy nearer to the X-ray centroid. We have also excluded galaxies with AGN-type line intensity ratios (see Section 3.7), as there is a small possibility that an X-ray centroid may be skewed towards a BCG if it is itself an X-ray emitter (although *ROSAT* HRI images demonstrate that point source contamination is in general not a problem). Although the coordinates of each optical galaxy are very

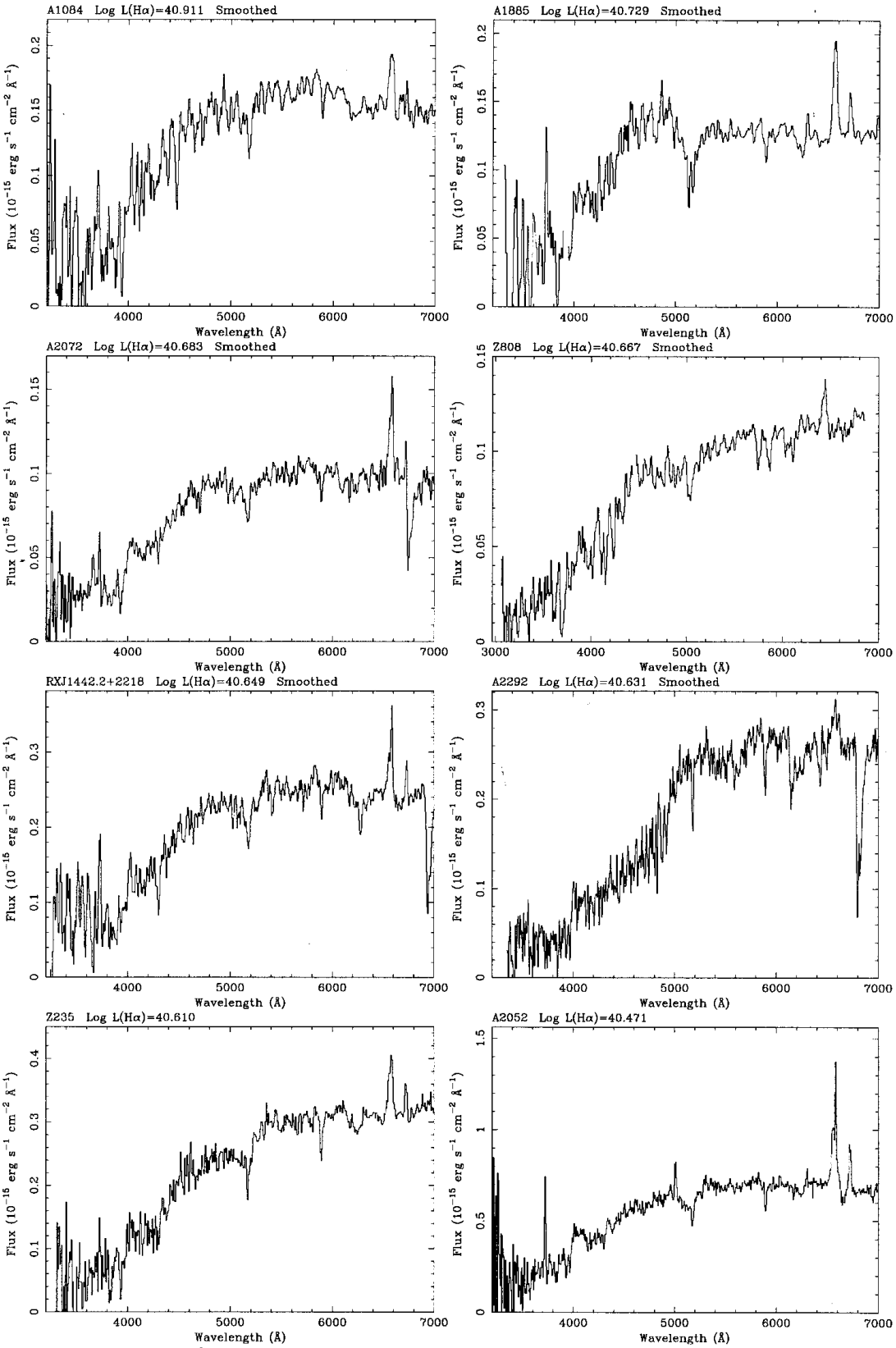

Figure 2 – *continued.* The spectra of line-emitting central cluster galaxies with log $L(\mathrm{H}\alpha)$ in the range 40.91–40.47.

well determined from the digitized POSS (Tables 1–3), the positions for the RASS X-ray sources are far less well determined due to the broadness of the RASS point spread function. To make things worse, the attitude solution for the RASS is less accurate than the one for pointed *ROSAT* observations, the photon statistics in the RASS are generally poor and faint blends are harder to recognize, all of which effects combine to give X-ray positional errors of up to about 1 arcmin. A few sources may have larger errors on the

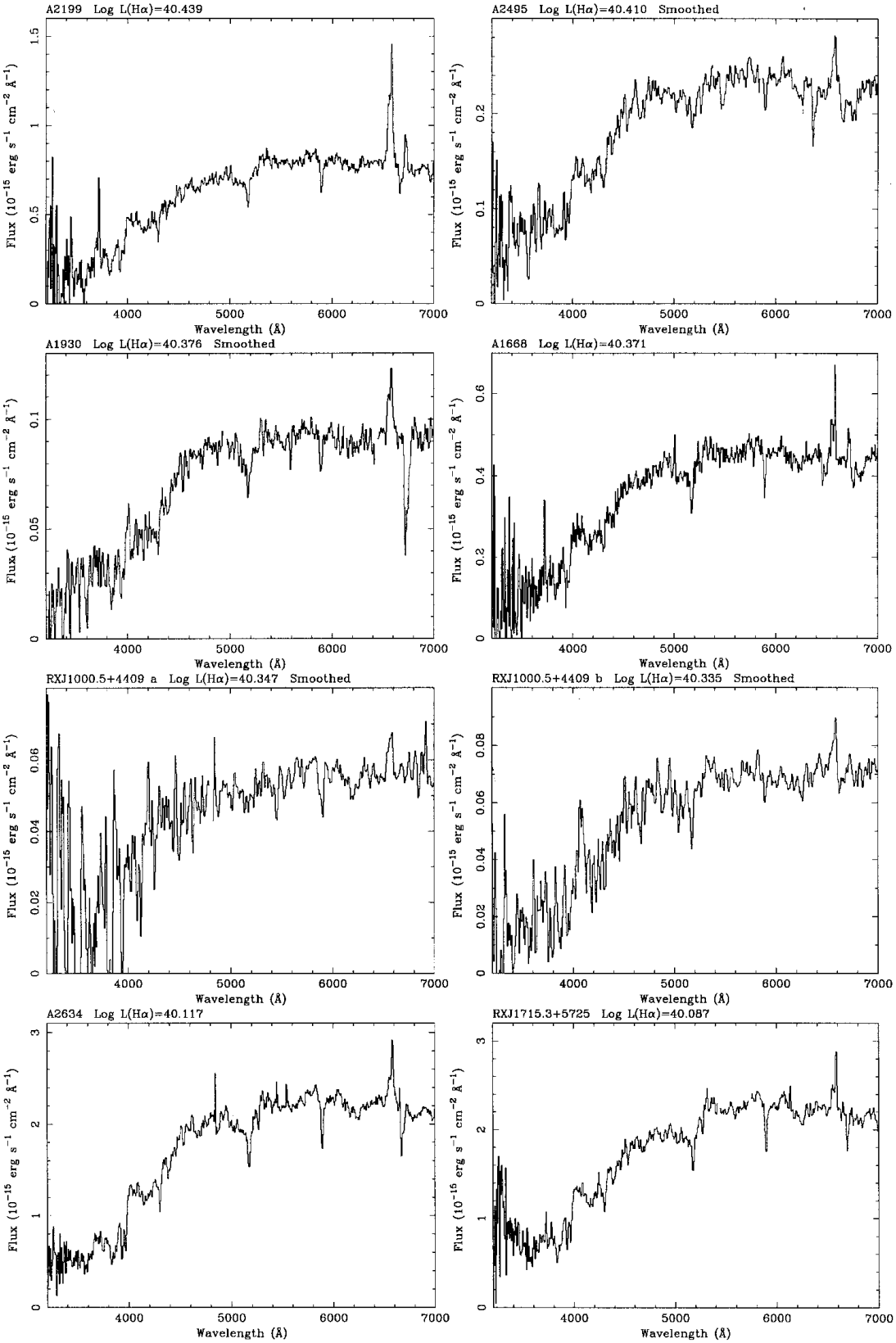

Figure 2 – *continued.* The spectra of line-emitting central cluster galaxies with log $L(\mathrm{H}\alpha)$ in the range 40.45–40.08.

X-ray centroid if the cluster contains an AGN or substantial substructure.

Even with these caveats on the accuracy of the X-ray position, we find that the projected separation between the X-ray centroid of the cluster and the optical position of the dominant galaxy differs according to the emission-line properties of the BCG. The line emitters (including the [N II]-only emitters) show a much smaller average separation between the BCG and cluster X-ray centroid

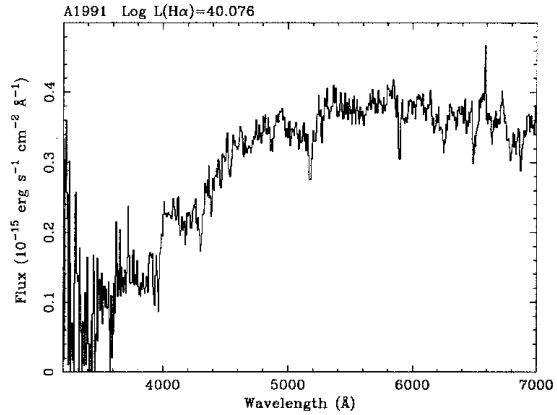

Figure 2 – *continued.* The spectrum of the line-emitting central cluster galaxy in A1991, with log $L(\mathrm{H}\alpha)$ of 40.07.

(with a mean of 29 ± 6 kpc) than do the others (a mean of 89 ± 8 kpc). Assuming that the majority of the line-emitting galaxies are contained in cooling flows, this is consistent with the results of both Allen (1998) and Peres et al. (1998) that the offset between the X-ray centroid and the brightest central galaxy, or the gravitational lensing centre are larger for non-cooling flow clusters. A precise positional coincidence is not necessarily expected, especially if the cluster contains a strong central radio source that may have displaced the cooling gas at the very centre, e.g., 3C84 in the Perseus cluster (Böhringer et al. 1993). We will address this issue further in the next paper in the series, using better X-ray centroids obtained from pointed *ROSAT* observations of this sample and also X-ray confirmation of whether an individual cluster contains a cooling flow.

3.5 Continuum spectral indices

The ultraviolet/blue continuum sometimes seen in BCGs is usually ascribed to the light from an excess young stellar population (e.g., JFN; McNamara & O'Connell 1989, 1992, 1993; Allen 1995; McNamara et al. 1999). The level of massive star formation can be assessed from its effect on absorption features in the spectrum of the galaxy (JFN; Cardiel, Gorgas & Aragon-Salamanca 1995, 1998). The excess blue light is concentrated towards the central 5–10 kpc of the galaxy, and outside of this region the stellar spectral indices are very similar to that of an ordinary giant elliptical galaxy (Cardiel et al. 1998). Thus, to make a meaningful comparison between galaxies in our sample, where possible we measure the continuum spectral indices in a spectrum taken from the same central region of a galaxy.

A spectrum for each galaxy was extracted from a projected aperture of diameter 10 kpc along the slit. This extraction is straightforward for the lower redshift objects, whereas the accuracy of obtaining a 10-kpc aperture at the more distant galaxies was dictated by whether the intensity peak fell on one or between two rows of the detector, and the need to extract a spectrum using an integer number of rows. In practice, the spectra are extracted from aperture sizes varying only between 8.6 and 11.2 kpc; we have listed the aperture used in column 2 of Table 4, where the stellar indices derived from these spectra are tabulated. Selecting a central aperture is possible only for the *new* IDS observations presented in this paper. For the FOS spectra taken from A92 and C95 we cannot specify the aperture (other than an upper limit taken from the slit length of 6 arcsec), as the spectra were extracted using an automatic optimal extraction technique that does not yield spatially extended information. The aperture taken to produce the spectra from the WHT observations in C95 is unknown.

The common presence of Balmer line emission in the blue continuum-excess galaxies precludes the use of standard Balmer absorption-line indices to assess the stellar population. Instead, we measure the strength of two other stellar features in our spectra: the Mg_2 index (which assesses the depth of the MgH and Mg*b* molecular bands at 5177 Å, as defined by Faber et al. 1985) and the '4000-Å break':

$$D_{4000} = \frac{\int_{4050}^{4250} f_\lambda \mathrm{d}\lambda}{\int_{3750}^{3950} f_\lambda \mathrm{d}\lambda}.$$

The 4000 Å-break was originally defined from spectra in f_ν (Bruzual 1983), but note that here we measure it from an f_λ spectrum. We also use a wider colour ratio, δBR, more suited to testing the presence of an excess blue continuum, as defined in A92 and C95:

$$\delta BR = \frac{\int_{3500}^{3650} f_\lambda \mathrm{d}\lambda}{\int_{5800}^{6200} f_\lambda \mathrm{d}\lambda}.$$

Unlike both D_{4000} and the Mg_2 index, δBR uses bandpasses free from line emission, although it is more sensitive to the presence of internal reddening (see Section 3.9). D_{4000} can be affected by the emission lines [Ne III]λ3869, [S II]λλ4069/4076 and Hδ, and the Mg_2 index by [N I]λ5199 and [O III]λ4959. In practice, these lines of [Ne III] and [S II] are rarely present in the BCG spectra, but contamination of Mg_2 by [O III] and [N I] is more commonplace. Where present, we remove emission lines by fitting them in a 'residual' spectrum created by subtracting a scaled non-emission-line galaxy template from the BCG (see Section 3.6). This emission-line model is then subtracted from the original galaxy spectrum, and the D_{4000} and Mg_2 stellar indices are measured from this line-corrected spectrum. The stellar indices for each galaxy are shown in Table 4, in RA order. Column 1 gives the name, and column 2 the projected spatial size of the aperture from which the given spectral indices are measured. Columns 3, 4 and 5 give the Mg_2 index, D_{4000} and δBR respectively. Column 6 presents the Hα luminosity *for the given aperture* – note that as the emission lines are often spatially extended beyond a 10-kpc diameter, this may represent an underestimate of the *total* Hα luminosity of the galaxy. Columns 7–9 give the estimate of internal reddening from the Balmer emission lines, and the corrected values of δBR and Hα luminosity (see Section 3.9). Bracketed values of D_{4000} in column 4 represent uncertain measures where examination of the spectrum suggests that the abnormally high value is caused by a loss of blue light from the slit.

3.6 Emission-line fitting

We estimate the spatial diameter of the line emission along the slit by extracting a profile of the galaxy centred on the observed [N II] and Hα emission, and subtracting the profile of the galaxy in nearby line-free continuum (e.g., 6400–6500 Å). The nebulae often extend well beyond the ~10-kpc aperture used to find the stellar indices in Section 3.5; so, in order to measure the *total* line luminosities from the galaxy in the slit, we have extracted a spectrum from the total spatial region spanned by the emission lines. We cannot rule out the possibility that the nebulae could also be extended in a direction perpendicular to the slit position, so these line fluxes may sometimes give underestimates of the *total* line luminosity of the galaxy.

We fit the emission lines in close sets, such as the Hα +[N II]λλ6548,6584+[S II]λλ6717,6731+[O I]λλ6300,6363 complex.

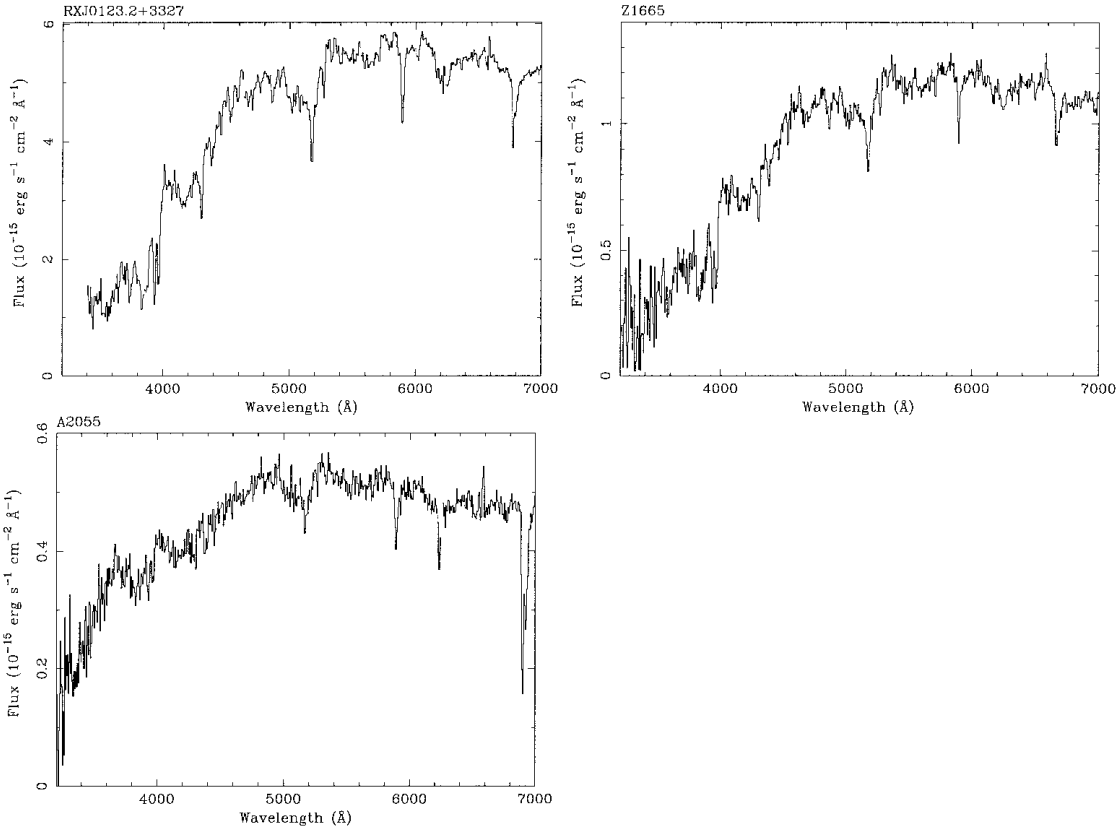

Figure 3. Three examples (RXJ0123.2+3327, Z1665 and A2055) of central cluster galaxies with spectra showing only low-level [N II]λλ6548,6584 line emission.

Within such a set, the individual emission lines are modelled as Gaussians fixed to be at the same redshift and velocity width as each other, and the underlying continuum is modelled by a linear function. The Hα +[N II]λλ6548,6584 blend is sufficiently resolved to give good fits for individual line components (e.g., Z3146, RXJ0439.0 + 0520, Z8197 in Fig. 2; note, however, that many other spectra in this figure are shown after smoothing, and belie the ease of resolving the lines). The resulting fluxes for the red emission lines of galaxies are given in Table 5; lines that are partially affected, or even completely absorbed by the Earth's atmosphere are marked by square brackets. The errors given on the fluxes are estimated from the $\Delta\chi^2 = 1$ confidence limits to the Gaussian intensity in each line, assuming that the fit to the (unweighted) spectrum has a reduced $\chi^2 = 1$. Thus these errors do not take into account any systematics introduced by the data reduction. 2σ upper limits are estimated for lines not detected, assuming them to have the same redshift and velocity width as the rest of the complex. We also assume that any Hα in absorption due to the underlying stellar continuum is negligible in comparison to the Hα visible in emission (this point is assessed further in Section 3.9).

We are unable to make such an assumption about stellar Hβ absorption in the underlying continuum, however, as it is expected to be stronger relative to the Hβ emission than is the case for Hα. In order to take the effects of stellar Hβ absorption into account, we created a template galaxy from the averaged rest-frame spectra of 24 galaxies in our sample. These galaxies were chosen to have good signal-to-noise ratios, no line emission, and 'average' stellar indices – i.e., Mg_2 in the range 0.25–0.32 and D_{4000} between 1.65 and 1.95; the final template had an Mg_2 index of 0.29 and D_{4000} of 1.9. The template was then normalized to each line-emitting central cluster galaxy in the region 5050–5100 Å (in the rest frame; this comprises the flat left-hand shoulder of the Mg absorption feature) and subtracted to give a residual spectrum. The [O III]λλ4959,5007, Hβ and [N I]λ5199 emission lines were then fitted together in the residual spectrum, again with each line modelled by a Gaussian of the same redshift and velocity width as each other. The fluxes of these blue emission lines are tabulated in Table 6, along with the flux of the [O II]λ3727 doublet, which was also fitted by a Gaussian (a satisfactory fit at this spectral resolution). In Table 6 we list first the fluxes of Hβ, [O III] and [N I] from the fits to the *non*-template-subtracted spectrum, and secondly in each column we list the fits from the residual spectrum in square brackets. If no template-subtracted result is presented, it is no improvement on the previous fit. The correction for the underlying continuum is not very significant for all the strong line emitters (e.g., Z3146, A1835). Although one might expect the depths of the Mg_2 and Hβ absorption features to be well correlated for an old stellar spectrum, this might not be the case for galaxies containing a blue light component. Galaxies with the strong line emission are in fact those that also contain the excess blue continuum (A92; Allen 1995; C95), for which the template subtraction given here may not be the most appropriate. However, it is clear that the line emission in these galaxies is so strong that errors due to inaccurate stellar Hβ absorption are minimal. Where the template subtraction is in danger of being most in error is if the galaxy contains a fading starburst with Balmer absorption lines at a maximum. Whilst this may not be a principal component of the most line-luminous systems, it may be relevant for lower luminosity systems.

Most of the galaxies newly observed for this paper are either non-emitters or show lower luminosity line emission than those in A92

and C95; only three of the new systems show a slit Hα luminosity above 3×10^{41} erg s^{-1} (RXJ1532.9 + 3021, A2204 and A2390). As well as being the second highest redshift cluster in the sample, RXJ1532.9 + 3021 contains an exceptionally line-luminous BCG, second only to that in Z3146.

The luminosity of the Hα line emission correlates with the size of the nebula (for those galaxies with spatially resolved spectra only), in the sense that the more luminous systems are larger. Fig. 6 shows a plot of the observed Hα surface brightness against the diameter of the emission-line nebula. The systems at higher luminosity are clearly larger (mean diameter of 34 kpc, compared to 8 kpc for the lower luminosity nebulae). These numbers are not precise, as the diameters are measured from slit positions placed at random over what may be an asymmetric nebula; this may be responsible for some of the scatter in the plot. Few of the lower luminosity systems are any larger than those showing only [N II] line emission.

We find no correlation between the velocity width (taken from the fit to the Hα + [N II] emission-line complex and corrected for the instrumental resolution) and the Hα luminosity for all the emission-line galaxies.

3.7 Line intensity ratios

We have calculated line intensity ratios, using the template-subtracted values of Hβ and [O III] line flux where relevant. The errors on the line ratios are formally propagated through from the errors on the line intensity from the fitting, and do not represent extrema of the division. We do not include the red emission-line ratios for RXJ1720.1 + 2638, as line fluxes of [N II] and Hα were badly affected by atmospheric absorption, and [S II] by a cosmic ray hit. RXJ1750.2 + 3505 is also excluded because the Hα line is affected by a cosmic ray hit.

We plot the ratio [N II]λ6584/Hα against the luminosity of Hα in Fig. 7, and confirm the trend for the more luminous systems to show a larger ratio of Balmer line emission to forbidden-line emission (as in Heckman et al. 1989, A92 and C95). We note that the galaxies form a continuous distribution of [N II]/Hα through four decades in Hα luminosity, with only a few obvious outliers. Whilst the majority of the clusters selected in an X-ray flux-limited sample will contain cooling flows, the emission-line BCGs in this paper may not be a heterogeneous set. Follow-up pointed X-ray data will detail exactly which clusters contain what strength of cooling flow (Allen et al., in preparation; Crawford et al., in preparation; Edge et al. 1999, in preparation), but it is possible to mark out exceptions from the optical emission-line spectrum alone. We broadly split the galaxies within the [N II]/Hα versus L(Hα) correlation shown in Fig. 7 into high-Hα-luminosity systems (L(Hα) > 10^{41} erg s^{-1}) marked by solid circles (e.g., A1835, Z3146, Z8193) and those of lower Hα luminosity (e.g., A262, A1991, A2199) marked by open circles. Note that whilst this division resembles the classification of cooling flow nebulae into 'class I'/'class II' systems of Heckman et al. (1989), the clusters show a *continuous* distribution between the two. In particular, this continuous behaviour makes the division between the two types fairly arbitrary, and there is some overlap at L(Hα)$\sim 10^{41}$ erg s^{-1} . Here the classification of each individual galaxy was also based on other line ratios (Fig. 8). The separation of the sample into different symbols in the figures is less an attempt to classify the observed systems, and more to separate out the behaviour of each end of the distribution in the diagrams in this paper. A few emission-line systems lie outside the general trend; these are marked either by stars for two systems with higher [N II]/Hα than expected for their Hα luminosity (A1068 and A2146), or by open triangles for the two systems with systematically lower [N II]/Hα at a range of Hα luminosity (A2294 and RXJ0821.0 + 0752; note that the position of these last two galaxies in Fig. 7 overlap). Although the central galaxies in A2204 and RXJ0439.0 + 0520 appear to have properties similar to the anomalously high [N II]/Hα systems (stars) in Fig. 7, their behaviour in all other plots fits better with the other high-luminosity systems (Fig. 8). The line intensity ratio diagrams of [O III]λ5007/Hβ and [S II]λ6717/Hα against [N II]λ6584/Hα are shown in Fig. 8. We choose these diagrams as they are the least subject to internal reddening (see Section 3.9). The ionization state of the nebula is also correlated with its size (Fig. 9).

3.8 Spatially extended emission-line ratios

The line ratio plots in Figs 7–9 are constructed from the flux-weighted *average* values, as given in Tables 5 and 6. It is possible, however, for the line ratios to vary within an individual galaxy. Such behaviour has been noted before for the central galaxy in S1101 (Crawford & Fabian 1992), where the relative intensities of [N II]λ6584 and Hα swap between the nucleus and an extended filament. Several of our emission-line galaxies are sufficiently extended that we are able to sample the line ratios at several points in the nebula. We find that the line ratios commonly change away from the centre of the galaxy, but not in a heterogeneous manner. For example, the line ratio [N II]/Hα can either increase (e.g., A1835; Fig. 10) or decrease (e.g., A1795; Fig. 10) between the galaxy and the extended parts of the nebula. The line ratio [S II]λ6717/Hα behaves in a similar manner to [N II]/Hα. The changes in ionization are not simply accounted for by an increased stellar Hα absorption in the galaxy continuum decreasing the amount of measured Hα line emission (and thus increasing the value of [N II]/Hα derived). First, the change in the [N II]/Hα line ratio with radius is in some galaxies positive (Figs 10 and 11). Secondly, we have estimated the effect of stellar absorption on the [N II]/Hα ratio for all these galaxies with spatially extended emission, by subtracting off the non-emitting template galaxy, scaled to match the depth of the (nearby) NaD absorption line. We find that the value of [N II]/Hα measured for the galaxy centre is decreased by at most 7 per cent (in RXJ0338.7 + 0958 and A1795), and more commonly by only 1–2 per cent. Thus the change in line ratio appears to be a real change in ionization.

3.9 Intrinsic reddening

For several of the galaxies, the Hα/Hβ intensity ratio is significantly greater than the expected canonical value of 2.86, suggesting that the observed spectra are reddened along the line of sight. We have already corrected the spectra for the extinction expected from our Galaxy, and so assume any further reddening is intrinsic to the central cluster galaxy. In column 7 of Table 4, we list the $E(B-V)$ derived from the observed Hα/Hβ intensity ratio in the $\sim$10-kpc aperture (and from the total aperture for spectra from A92 and C95). The intensity of Hβ is measured by again constructing a difference spectrum (see Section 3.6; but for the 10-kpc apertures now) to approximate Hβ in absorption from the underlying galaxy continuum. We estimate $E(B-V)$ only where Hβ was detected, or should have been significantly detected above the noise if it were 35 per cent of the Hα intensity. We also omit galaxies with only marginal evidence for internal reddening as deduced from a noisy line ratio (e.g., A1204, Z3916). The limits shown on $E(B-V)$ are propagated from the errors to the fits of the Hα and Hβ emission-line fluxes, and do not take into account any systematics (for

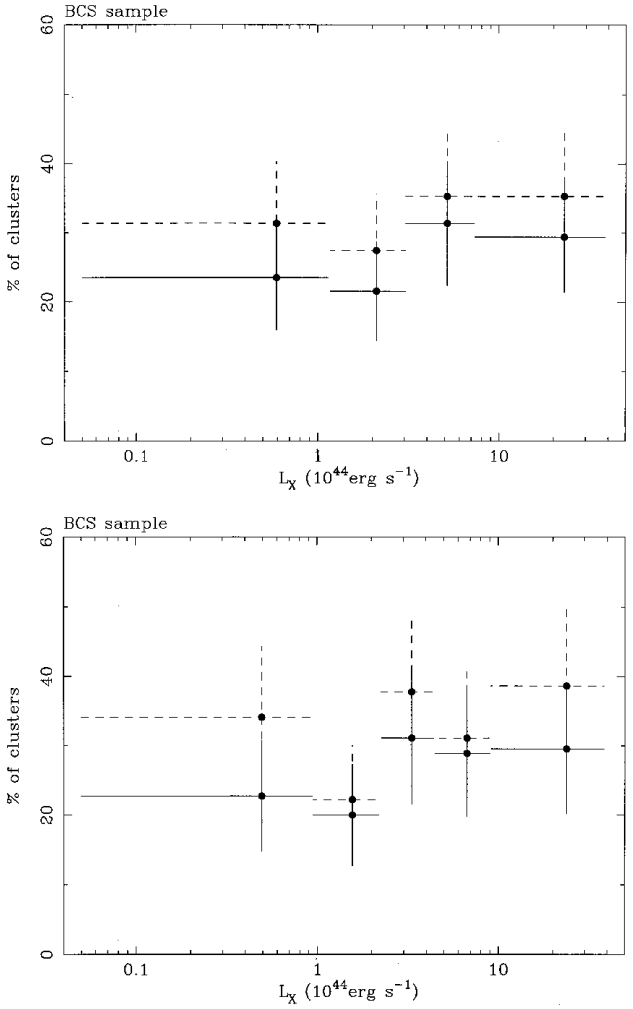

Figure 4. Frequency of line emitters as a function of 0.1–2.4 keV X-ray luminosity: (top) for those galaxies in the BCS (i.e., Tables 1 and 3, assuming that the five clusters whose spectral properties are not known are non-line emitters) and (bottom) for all the galaxies included in this paper for which we have the X-ray luminosity (i.e., members of the BCS, 'sub'-BCS and XBACS). In both panels, markers with solid error bars show only the line emitters marked by a $\surd$ in Tables 1–3, whilst the markers with dotted error bars include those with low-level [N II]λλ6548,6584 and no Hα. The errors assume $\sqrt{n}$ statistics.

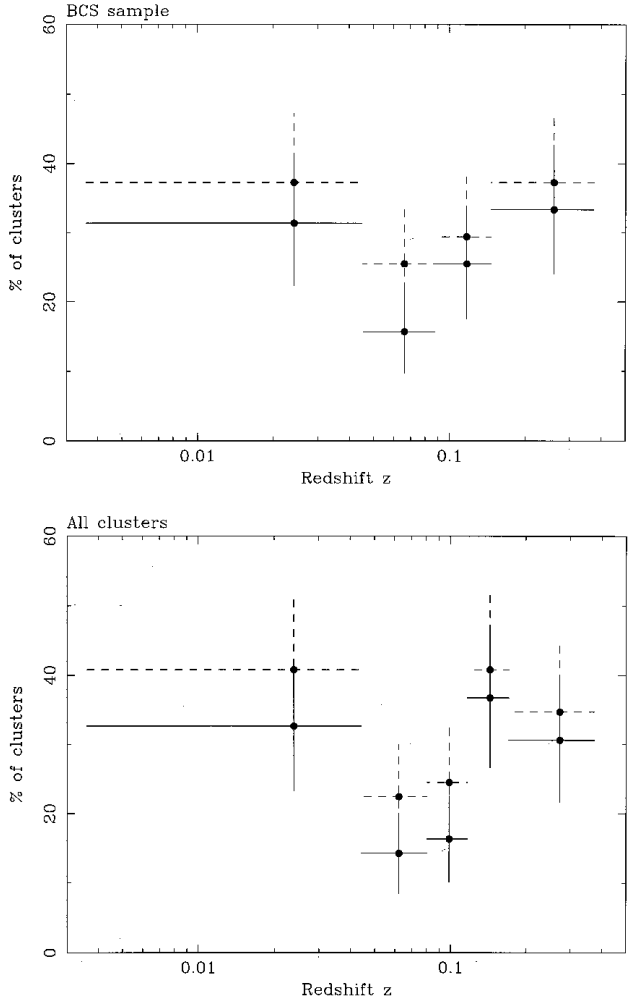

Figure 5. Frequency of line-emitting central cluster galaxies as a function of redshift for (top) all the BCS sample (i.e., Tables 1 and 3, assuming that the five clusters whose spectral properties are not known are non-line emitters) and (bottom) for all clusters included in the paper. Markers and error bars as in Fig. 4.

example, the appropriateness of the template subtraction). The spectra of the affected galaxies are then dereddened by the amount shown, assuming $R = 3.2$ and that the dust forms a uniform screen at the redshift of the galaxy. We then measure 'revised' values of the δBR index and Hα luminosity, shown in columns 8 and 9 of Table 4 respectively. The errors on the revised values of δBR and Hα luminosity are from the fits, and not due to the range of values given by the errors on $E(B-V)$. The Mg_2 index is not affected by reddening, and the D_{4000} break is less affected than δBR.

We have six spectra in common with Allen (1995), and find reduced values of $E(B-V)$ for some of these objects (e.g., A1664, A1068). Although we use the same spectra, this difference is due to our template subtraction increasing the measured Hβ flux and thus increasing the Hα/Hβ ratio. Our errors on $E(B-V)$ are also smaller than those of Allen, as we propagate the errors to the intensity from the fits to the emission lines (which we also quote to 1σ rather than to 90 per cent) to give errors on the Hα/Hβ ratio, rather than using the extrema of the fits. There are several galaxies with low-level line emission for which the Hα/Hβ ratio is significantly less than 2.86 (e.g., Z2701, RXJ1230.7 + 1220). This suggests that for these galaxies it is necessary to also take into account Hα in absorption to give an accurate Balmer decrement. Several galaxies have the lower limit to $E(B-V)$ consistent with no internal reddening (e.g., A478, A646, A1795, A2052 and A2199).

Placement of the spectrograph slit at the telescope depends on a (live) direct image, and is thus optimized to the strong red continuum of an elliptical galaxy. Thus, if a galaxy is not observed at the parallactic angle, we can expect the blue light to be preferentially lost from the slit spectrum. This might affect the observations (in that the Hα/Hβ intensity ratio is artifically increased due to preferential loss of Hβ from the slit) of A291, RXJ0338.7 + 0958 and A1795, and does appear from the spectrum (see Fig. 2) to be important for the observations of RXJ0352.9 + 1941 and RXJ0439.0 + 0520. However, we note that a galaxy marked as an 'low-luminosity outlier' in Figs 7–9 (RXJ0821.0 + 0752; the other A2294 is too noisy to tell) requires a exceptionally high level of internal reddening [$E(B-V) > 1.1$] to interpret the lack of a strong Hβ detection. We note, however, that

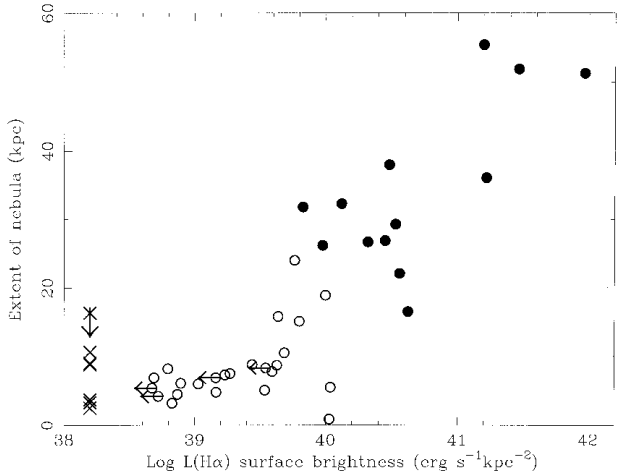

Figure 6. Hα surface brightness plotted against the diameter of the nebula for all galaxies with spatially resolved spectra. High-Hα-luminosity systems [L(Hα)> 10^{41} erg s^{-1}] are shown by solid circles, and the lower luminosity line emitters by open circles. The crosses shown at an arbitrary value of Hα surface brightness of $10^{38.2}$ erg s^{-1} kpc^{-2} indicate the diameters of the [N II]-*only* emitters.

this galaxy was not observed at the parallactic angle (and so Hβ may have been preferentially been lost from the slit relative to Hα).

3.10 Relation of the stellar indices to line luminosity

We plot the values of Mg_2 and D_{4000} for the newly observed galaxies (IDS spectra) in Fig. 12, excluding spectra marked as noisy in Table 4. The indices are all measured from a central ~10-kpc aperture, and the galaxies are marked by symbols dependent on both the presence and strength of Hα line emission in the spectrum. The high-luminosity systems are marked by solid circles, and the lower luminosity systems by open circles of the same size. [N II]-only and non-line emitters are also marked by open circles, but of a smaller size as shown in the key to the figure. Observations not taken at the parallactic angle (which may affect the measured value

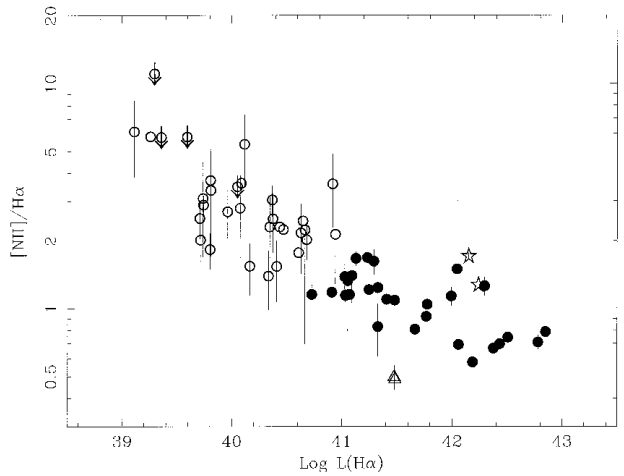

Figure 7. Plot of the Hα slit luminosity against the [N II]λ6584/Hα line intensity ratio, for all emission-line objects in this paper. High-Hα-luminosity systems are marked by solid circles, and lower luminosity ones by open circles. Outliers from the general trend are marked by stars (at higher ionization) or by open triangles (at lower ionization; two markers which overlap).

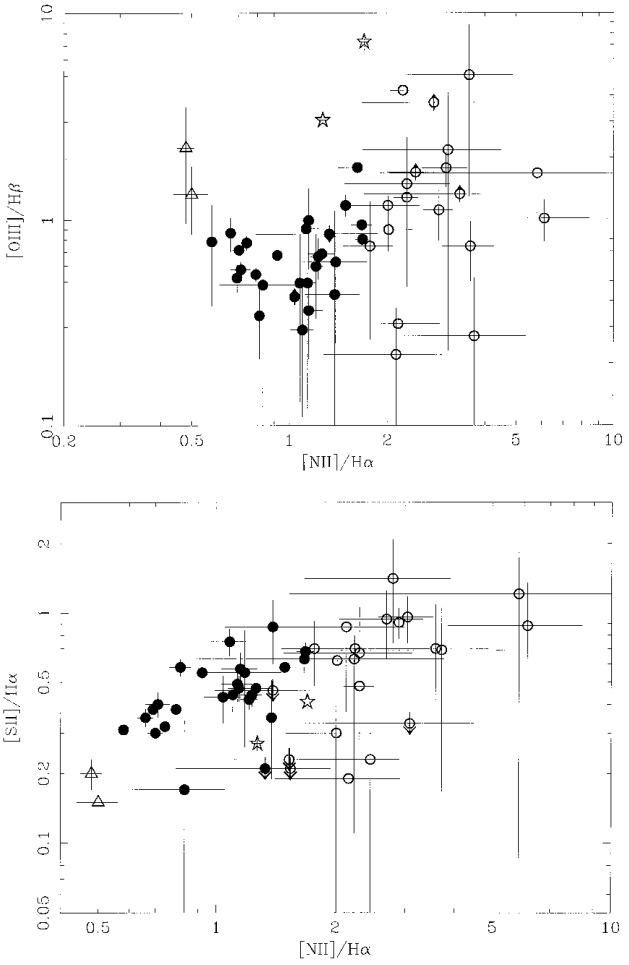

Figure 8. Plot of the line intensity ratios [O III]λ5007/Hβ (top) and [S II]λ6717/Hα (bottom) against [N II]λ6584/Hα. Symbols as in Fig. 7.

of D_{4000}) are marked also by a cross. Fig. 13 shows the same data, but now including stellar indices measured from the spectra presented in A92 and C95, and again excluding spectra marked as noisy in Table 4. The larger scatter within the plot is mainly due to the variety of projected apertures from which the FOS and WHT spectra are extracted. None the less, the same trend as in Fig. 12 is apparent; the stronger line emitters show a significantly bluer spectrum, i.e., a lower D_{4000} for a given Mg_2 index. The lower luminosity line emitters show stellar indices little different from the general population of BCG.

The association of high-luminosity line emitters with the excess blue continuum is also apparent from a plot of Hα line luminosity against δBR for all apertures (Fig. 14), whether these quantities are corrected for internal reddening or not. The distribution of δBR observed in the *non*-line-emitting BCG in the sample is also plotted by diamond markers at the arbitrary value of $L(\mathrm{H}\alpha) = 3 \times 10^{38}$ erg s^{-1}, using only spectra from the ~10-kpc apertures. The size of diamond marker plotted is directly proportional to the number of non-emitting galaxies with that value of δBR, where the majority lie in the range $0.08 < \delta BR < 0.11$. Of the three non-emitting systems with $\delta BR = 0.05$, two are not at the parallactic angle. There are a total of six non-line-emitters with $0.14 < \delta BR < 0.20$, and only one above δBR of 0.20 (A1366 at δBR of 0.23). Similar values are found for the δBR values for the data from

Table 4. Stellar indices and Hα luminosities from the ∼10-kpc galaxy apertures.

Cluster		aperture size (kpc)	Mg_2 index	4000-Å break	δBR	L(Hα) (10^{40}erg/s)	$E(B-V)$	revised δBR	revised L(Hα) (10^{40}erg/s)
A7		10.5	0.31	1.92	0.11	—	—	—	—
A21	a	10.1	0.30	2.12	0.05	—	—	—	—
	b	10.1	0.31	2.09	0.08	—	—	—	—
A76		10.0	0.32	1.91	0.08	—	—	—	—
Z235		<12.6	0.29	1.90	0.06	$4.1^{+0.6}_{-0.6}$	—	—	—
A115		8.8	0.33	1.60	0.14	$12.7^{+1.9}_{-1.8}$	—	—	—
RXJ0107.4+3227		10.4	0.31	1.78	0.09	$0.5^{+0.1}_{-0.1}$	—	—	—
Z353 [1]		<15.9	0.24	(7.1)	0.02	—	—	—	—
A168		10.1	0.30	1.89	0.11	—	—	—	—
RXJ0123.2+3327		9.8	0.30	1.86	0.09	—	—	—	—
RXJ0123.6+3315		10.4	0.25	1.88	0.09	—	—	—	—
A193		10.0	0.29	1.77	0.09	—	—	—	—
A267		<27.9	0.31	1.91	0.08	—	—	—	—
A262		10.2	0.28	1.95	0.08	$0.6^{+0.1}_{-0.1}$	—	—	—
A272		9.5	0.34	1.85	0.10	—	—	—	—
A291		<25.1	0.28	1.56	0.23	$45.9^{+2.2}_{-1.9}$	—	—	—
RXJ0228.2+2811		10.1	0.30	1.85	0.09	—	—	—	—
A376		9.9	0.30	1.92	0.09	—	—	—	—
A400	a	10.2	0.31	1.90	0.07	—	—	—	—
	b	10.9	0.29	1.86	0.07	—	—	—	—
A399		10.1	0.29	1.68	0.14	—	—	—	—
A401		10.6	0.28	1.58	0.13	—	—	—	—
Z808		<22.4	0.23	2.02	0.08	$4.6^{+1.2}_{-1.3}$	—	—	—
A407		10.9	0.27	1.79	0.10	—	—	—	—
A409 [2]		<20.8	0.28	2.47	0.08	—	—	—	—
RXJ0338.7+0958		9.7	0.28	1.37	0.11	$10.3^{+0.5}_{-0.4}$	$0.43^{+0.13}_{-0.15}$	$0.24^{+0.07}_{-0.06}$	$29.0^{+10.6}_{-8.8}$
RXJ0341.3+1524		<4.8	0.28	2.37	0.05	—	—	—	—
RXJ0352.9+1941 [1]		<15.9	0.27	(2.81)	0.04	$58.2^{+1.3}_{-1.6}$	$0.43^{+0.07}_{-0.07}$	$0.08^{+0.01}_{-0.01}$	$148.7^{+27.3}_{-23.0}$
A478 [2]		<13.0	0.24	2.08	0.11	$10.8^{+0.5}_{-0.5}$	$0.29^{+0.25}_{-0.29}$	$0.20^{+0.11}_{-0.09}$	$20.1^{+16.8}_{-9.3}$
RXJ0419.6+0225		10.6	0.31	1.80	0.10	—	—	—	—
RXJ0439.0+0715 [2]		10.2	0.24	1.76	0.17	—	—	—	—
RXJ0439.0+0520 [1]		<26.1	0.35	1.32	0.09	$110.7^{+3.0}_{-4.5}$	$0.40^{+0.07}_{-0.08}$	$0.19^{+0.03}_{-0.03}$	$239.7^{+42.3}_{-44.0}$
A520 [2]		8.9	0.22	2.02	0.13	—	—	—	—
A523		10.7	0.32	1.82	0.12	—	—	—	—
A531		<14.0	0.29	1.66	0.09	—	—	—	—
RXJ0503.1+0608		<13.3	0.30	2.19	0.04	—	—	—	—
RXJ0510.7−0801		<26.8	0.33	1.65	0.05	—	—	—	—
Z1121		<12.6	0.18	1.13	0.11	—	—	—	—
Z1133		<22.9	0.30	1.91	0.07	—	—	—	—
A566		9.9	0.29	1.62	0.15	—	—	—	—
A576	a	9.9	0.28	1.70	0.10	—	—	—	—
	b	10.8	0.30	1.89	0.10	—	—	—	—
A586		10.5	0.28	1.73	0.17	—	—	—	—
RXJ0740.9+5526		10.5	0.29	1.76	0.07	—	—	—	—
RXJ0751.3+5012	a	9.8	0.29	1.96	0.08	—	—	—	—
	b	10.2	0.28	1.49	0.12	$0.5^{+0.1}_{-0.1}$	—	—	—
	c	10.1	0.29	1.82	0.10	—	—	—	—
A602	a	9.9	0.21	1.74	0.11	—	—	—	—
	b	9.9	0.31	1.53	0.12	—	—	—	—
A611 [2]		<32.2	0.16	1.57	0.12	—	—	—	—
A621		<27.3	0.23	2.03	0.04	—	—	—	—
RXJ0819.6+6336		10.9	0.34	1.62	0.14	—	—	—	—
RXJ0821.0+0752		<16.0	0.27	1.73	0.10	$30.3^{+2.2}_{-1.9}$	$1.16^{+0.33}_{-0.58}$		
A646		10.5	0.25	1.39	0.17	$15.6^{+1.2}_{-1.1}$	$0.06^{+0.10}_{-0.06}$	$0.18^{+0.04}_{-0.01}$	$17.6^{+5.4}_{-2.0}$
Z1665		10.8	0.28	1.65	0.11	—	—	—	—
A655		10.6	0.26	1.74	0.13	—	—	—	—
A667		<20.0	0.31	1.92	0.07	—	—	—	—
A671		9.5	0.28	1.75	0.09	—	—	—	—
A665		11.1	0.19	1.76	0.12	—	—	—	—
A689 [2]		<31.0	0.04	1.06	0.38	—	—	—	—
A697		<31.8	0.26	1.85	0.11	—	—	—	—
A750 [2]		10.9	0.15	1.91	0.16	—	—	—	—
A761		<13.6	0.31	1.40	0.16	—	—	—	—

Table 4 – *continued*

Cluster		aperture size (kpc)	Mg_2 index	4000-Å break	δBR	$L(H\alpha)$ (10^{40}erg/s)	$E(B-V)$	revised δBR	revised $L(H\alpha)$ (10^{40}erg/s)
A763		9.4	0.26	1.80	0.12	—	—	—	—
A757		9.7	0.30	1.87	0.10	—	—	—	—
A773	a	<26.8	0.27	2.32	0.11	—	—	—	—
	b	<27.4	0.31	1.90	0.10	—	—	—	—
A795		8.8	0.32	1.61	0.14	$12.9^{+1.0}_{-1.1}$	—	—	—
Z2701		<26.7	0.28	1.81	0.06	$8.7^{+2.8}_{-2.8}$	—	—	—
RXJ1000.5 + 4409 [2]	a	<21.0	0.12	1.93	0.08	$2.2^{+0.8}_{-0.8}$	—	—	—
	b	<20.8	0.33	2.23	0.09	—	—	—	—
Z2844		10.3	0.36	1.79	0.09	—	—	—	—
A961 [2]		9.7	0.24	2.44	0.07	—	—	—	—
A963		9.1	0.31	1.94	0.10	—	—	—	—
A971		—	0.20	1.96	0.08	—	—	—	—
A980		10.0	0.30	1.79	0.11	—	—	—	—
Z3146		<32.0	0.22	1.14	0.42	$704.7^{+14.8}_{-11.1}$	$0.20^{+0.04}_{-0.03}$	$0.58^{+0.05}_{-0.03}$	$881.5^{+88.5}_{-61.5}$
A990 [2]		—	0.36	2.13	0.12	—	—	—	—
Z3179		<19.8	0.22	1.90	0.07	$9.1^{+2.0}_{-3.1}$	—	—	—
A1023		<16.8	0.27	1.76	0.13	—	—	—	—
A1033		<17.9	0.33	1.50	0.14	—	—	—	—
A1035		11.2	0.32	1.73	0.10	—	—	—	—
A1045		<19.2	0.28	1.55	0.14	—	—	—	—
A1068		<19.3	0.27	1.24	0.24	$172.6^{+20.1}_{-19.3}$	$0.39^{+0.07}_{-0.08}$	$0.50^{+0.07}_{-0.07}$	$386.8^{+71.3}_{-67.8}$
A1084 [1]		<18.6	0.30	2.16	0.04	$8.0^{+0.9}_{-1.3}$	—	—	—
A1132		11.1	0.32	1.76	0.12	—	—	—	—
A1173		11.0	0.26	1.69	0.08	—	—	—	—
A1177		11.2	0.28	1.80	0.08	—	—	—	—
A1185	a	10.0	0.26	1.64	0.09	—	—	—	—
	b	10.8	0.25	1.84	0.08	—	—	—	—
	c	8.9	0.26	1.83	0.06	—	—	—	—
A1190		11.0	0.26	1.63	0.05	—	—	—	—
A1201		10.4	0.29	1.80	0.14	—	—	—	—
A1204 [2]		<22.6	0.26	1.72	0.12	$10.6^{+1.8}_{-1.3}$	—	—	—
Z3916 [2]		—	0.24	1.44	0.04	$30.2^{+1.9}_{-3.6}$	—	—	—
A1246		<24.5	0.28	1.83	0.13	—	—	—	—
A1302		9.7	0.34	1.78	0.10	—	—	—	—
A1314		9.7	0.33	1.76	0.08	—	—	—	—
A1361		<16.8	0.35	1.48	0.11	$13.5^{+3.5}_{-1.9}$	—	—	—
A1366		9.7	0.25	1.24	0.23	—	—	—	—
A1413		9.2	0.34	1.75	0.10	—	—	—	—
Z4673		<19.6	0.22	1.66	0.14	—	—	—	—
A1423 [2]		—	0.31	2.44	0.04	—	—	—	—
A1437	a	10.9	0.29	1.75	0.11	—	—	—	—
	b	10.8	0.29	1.74	0.11	—	—	—	—
Z4803		9.6	0.29	1.86	0.07	—	—	—	—
RXJ1205.1 + 3920		<6.1	0.16	1.88	0.07	—	—	—	—
RXJ1206.5 + 2810		9.9	0.28	1.82	0.11	$0.7^{+0.1}_{-0.1}$	—	—	—
Z4905		9.6	0.24	1.56	0.10	—	—	—	—
Z5029		9.6	0.34	1.67	0.09	—	—	—	—
RXJ1223.0 + 1037		10.1	0.27	1.69	0.09	$0.5^{+0.2}_{-0.2}$	—	—	—
A1553	a	10.3	0.27	1.98	0.10	—	—	—	—
	b	10.6	0.32	1.72	0.13	—	—	—	—
RXJ1230.7 + 1220		9.9	0.32	1.72	0.11	$0.1^{+0.0}_{-0.1}$	—	—	—
Z5247		10.3	0.34	1.90	0.08	—	—	—	—
A1589		10.2	0.26	1.80	0.10	—	—	—	—
Z5604 [2]		<27.7	0.23	1.26	0.04	—	—	—	—
A1651		<13.0	0.39	1.94	0.06	—	—	—	—
A1656		10.2	0.29	1.94	0.09	—	—	—	—
A1664		<18.0	0.29	1.24	0.37	$113.8^{+2.7}_{-2.2}$	$0.46^{+0.06}_{-0.07}$	$0.91^{+0.11}_{-0.11}$	$304.9^{+42.6}_{-47.4}$
A1668		10.5	0.31	1.66	0.08	$2.3^{+0.4}_{-0.4}$	—	—	—
A1672 [2]		<24.3	0.30	1.60	0.15	—	—	—	—
Z5694		<24.0	0.24	2.05	0.09	—	—	—	—
A1682	a	<27.0	0.31	1.85	0.19	—	—	—	—
	b	<28.2	0.33	1.50	0.14	—	—	—	—

Table 4 – *continued*

Cluster		aperture size (kpc)	Mg_2 index	4000-Å break	δBR	L(Hα) (10^{40}erg/s)	$E(B-V)$	revised δBR	revised L(Hα) (10^{40}erg/s)
A1703	a	<31.9	0.25	2.22	0.08	—	—	—	—
[2]	b	<28.2	0.13	0.85	0.15	—	—	—	—
RXJ1320.1 + 3308	a	9.6	0.33	1.84	0.08	$0.4^{+0.3}_{-0.3}$	—	—	—
	b	10.8	0.21	1.80	0.10	—	—	—	—
RXJ1326.3 + 0013		10.2	0.21	1.61	0.12	—	—	—	—
A1758		<31.6	0.26	1.78	0.07	—	—	—	—
A1763		9.7	0.34	2.06	0.09	—	—	—	—
A1767		10.3	0.29	1.76	0.08	—	—	—	—
A1775	a	8.9	0.24	1.72	0.09	—	—	—	—
	b	10.9	0.32	1.76	0.09	—	—	—	—
A1773		9.5	0.23	1.62	0.12	—	—	—	—
A1795		10.3	0.24	1.27	0.13	$11.3^{+0.4}_{-0.3}$	$0.15^{+0.15}_{-0.15}$	$0.18^{+0.06}_{-0.05}$	$16.1^{+7.0}_{-4.8}$
A1800		9.4	0.26	1.68	0.10	—	—	—	—
A1809		9.9	0.30	1.81	0.10	—	—	—	—
A1831		12.2	0.28	1.75	0.11	—	—	—	—
A1835		10.4	0.10	1.16	0.33	$163.9^{+2.1}_{-3.6}$	$0.40^{+0.06}_{-0.06}$	$0.71^{+0.09}_{-0.08}$	$430.3^{+67.0}_{-58.4}$
		10.4	0.14	1.15	0.29	$144.0^{+2.9}_{-2.9}$	$0.55^{+0.15}_{-0.12}$	$0.93^{+0.31}_{-0.19}$	$494.9^{+218.7}_{-124.5}$
		<29.7	0.27	1.11	0.27	$318.9^{+6.2}_{-6.0}$	$0.38^{+0.04}_{-0.04}$	$0.54^{+0.09}_{-0.09}$	$784.4^{+161.2}_{-147.4}$
A1885 [2]		<13.5	0.47	1.81	0.09	$5.4^{+0.4}_{-0.4}$	—	—	—
Z6718 [2]		<11.0	0.34	1.90	0.05	—	—	—	—
A1902 [2]		<21.5	0.15	1.46	0.23	—	—	—	—
A1914		10.5	0.32	1.77	0.11	—	—	—	—
A1918		10.1	0.28	1.78	0.09	—	—	—	—
A1927		10.1	0.32	1.84	0.07	—	—	—	—
A1930		10.8	0.30	1.67	0.12	$2.4^{+0.6}_{-0.6}$	—	—	—
RXJ1440.6 + 0327	a	9.9	0.28	1.80	0.08	—	—	—	—
	b	9.9	0.28	1.79	0.07	—	—	—	—
RXJ1442.2 + 2218		10.1	0.32	1.92	0.11	$3.7^{+0.4}_{-0.4}$	—	—	—
RXJ1449.5 + 2746		10.2	0.33	1.80	0.10	—	—	—	—
A1978		9.4	0.32	1.78	0.09	—	—	—	—
A1983	a	10.0	0.26	1.50	0.12	—	—	—	—
	b	10.4	0.24	2.02	0.06	—	—	—	—
A1991		9.9	0.27	1.62	0.10	$1.1^{+0.3}_{-0.3}$	—	—	—
Z7160		<30.1	0.31	1.58	0.10	$50.3^{+4.6}_{-4.7}$	$0.24^{+0.13}_{-0.11}$	$0.49^{+0.23}_{-0.34}$	$153.1^{+113.7}_{-85.8}$
A2009		9.7	0.19	1.60	0.13	$6.1^{+1.2}_{-1.1}$	—	—	—
A2034	a	<16.6	0.28	2.10	0.05	—	—	—	—
	b	<16.1	0.26	1.69	0.08	—	—	—	—
A2029		9.8	0.28	1.72	0.10	—	—	—	—
A2033		9.7	0.32	1.70	0.12	—	—	—	—
A2050		9.7	0.34	2.19	0.10	—	—	—	—
A2052		9.4	0.26	1.64	0.10	$2.6^{+0.4}_{-0.4}$	$0.22^{+0.16}_{-0.21}$	$0.15^{+0.07}_{-0.05}$	$4.8^{+2.1}_{-1.8}$
A2055	a	8.8	0.16	1.14	0.25	—	—	—	—
	b	8.8	0.25	1.82	0.09	—	—	—	—
	c	10.8	0.25	1.67	0.11	—	—	—	—
A2064		9.3	0.31	1.77	0.10	—	—	—	—
A2061	a	9.5	0.26	1.69	0.11	—	—	—	—
	b	9.6	0.30	1.75	0.10	—	—	—	—
RXJ1522.0 + 0741		10.2	0.28	1.75	0.08	—	—	—	—
A2065	a	8.8	0.28	1.83	0.07	—	—	—	—
	b	10.2	0.24	1.79	0.10	—	—	—	—
	c	9.4	0.33	1.77	0.08	—	—	—	—
A2063		9.9	0.25	1.75	0.08	—	—	—	—
A2069	a	9.6	0.32	1.86	0.09	—	—	—	—
	b	9.3	0.27	1.76	0.09	—	—	—	—
	c	9.6	0.27	1.88	0.07	—	—	—	—
A2072		10.5	0.31	1.93	0.11	$4.8^{+0.9}_{-1.0}$	—	—	—
RXJ1532.9 + 3021		8.6	0.14	1.18	0.32	$415.5^{+20.8}_{-19.5}$	$0.21^{+0.03}_{-0.03}$	$0.48^{+0.03}_{-0.03}$	$689.4^{+51.6}_{-50.3}$
A2107		10.4	0.29	1.79	0.08	—	—	—	—
A2111 [2]	a	9.8	0.26	2.27	0.07	—	—	—	—
[2]	b	9.8	0.33	1.86	0.12	—	—	—	—
A2110		10.1	0.28	1.74	0.10	—	—	—	—
A2104 [2]		<21.1	0.31	1.53	0.18	—	—	—	—
A2124		9.7	0.28	1.70	0.10	—	—	—	—

Table 4 – *continued*

Cluster		aperture size (kpc)	Mg_2 index	4000-Å break	δBR	$L(H\alpha)$ (10^{40}erg/s)	$E(B-V)$	revised δBR	revised $L(H\alpha)$ (10^{40}erg/s)
A2146		<28.3	0.30	1.38	0.14	$141.3^{+4.6}_{-4.8}$	$0.20^{+0.07}_{-0.08}$	$0.21^{+0.03}_{-0.03}$	$185.8^{+34.4}_{-32.7}$
A2142	a	10.9	0.32	1.80	0.13	—	—	—	—
	b	9.9	0.35	1.68	0.11	—	—	—	—
A2147		10.3	0.30	1.76	0.09	—	—	—	—
A2151a		8.7	0.32	1.88	0.09	—	—	—	—
RXJ1604.9 + 2356		9.4	0.31	1.77	0.08	—	—	—	—
Z7833		<26.5	0.25	1.79	0.11	—	—	—	—
A2175		10.0	0.33	1.75	0.09	—	—	—	—
A2187 [2]		<23.9	0.23	1.91	0.10	—	—	—	—
A2201 [2]		—	0.17	1.95	0.05	—	—	—	—
A2199		10.2	0.29	1.73	0.08	$2.7^{+0.2}_{-0.3}$	$0.10^{+0.09}_{-0.10}$	$0.10^{+0.01}_{-0.01}$	$3.5^{+0.8}_{-0.8}$
A2208		<18.6	0.28	1.73	0.11	—	—	—	—
A2204		9.6	0.23	1.08	0.31	$159.4^{+4.1}_{-3.4}$	—	—	—
A2219 [2]	a	<27.5	0.43	2.22	0.13	—	—	—	—
[2]	b	<27.5	0.34	1.44	0.04	—	—	—	—
[2]	c	<28.3	0.22	1.56	0.14	—	—	—	—
A2228 [2]		<14.9	0.46	1.89	0.08	—	—	—	—
RXJ1657.8 + 2751		9.0	0.28	2.07	0.14	—	—	—	—
A2244		10.3	0.27	1.68	0.10	—	—	—	—
A2256	a	9.1	0.28	1.67	0.09	—	—	—	—
	b	9.4	0.30	1.94	0.06	—	—	—	—
	c	8.8	0.27	1.84	0.03	—	—	—	—
	d	9.9	0.27	1.79	0.08	—	—	—	—
A2249		9.2	0.28	1.69	0.10	—	—	—	—
A2255	a	10.5	0.33	1.71	0.10	—	—	—	—
	b	9.3	0.25	1.74	0.08	—	—	—	—
RXJ1715.3 + 5725		9.3	0.27	1.65	0.11	$1.2^{+0.2}_{-0.2}$	—	—	—
Z8193		<23.1	0.18	1.49	0.19	$153.1^{+4.5}_{-5.8}$	$0.57^{+0.13}_{-0.15}$	$0.56^{+0.16}_{-0.14}$	$605.8^{+220.0}_{-42.3}$
A2254 [2]		—	0.36	2.05	0.04	—	—	—	—
Z8197		9.6	0.26	1.42	0.13	$16.0^{+0.8}_{-0.8}$	$0.33^{+0.12}_{-0.10}$	$0.25^{+0.06}_{-0.04}$	$35.1^{+11.6}_{-7.4}$
A2259 [2]		—	0.24	2.15	0.07	—	—	—	—
RXJ1720.1 + 2638		8.8	0.31	1.25	0.14	$[12.7^{+2.7}_{-3.2}]$	—	—	—
A2261 [2]		—	0.35	2.48	0.04	—	—	—	—
A2294 [2]		—	−0.02	1.56	−0.03	$30.2^{+2.3}_{-2.3}$	—	—	—
RXJ1733.0 + 4345		9.6	0.29	1.78	0.09	$0.2^{+0.1}_{-0.1}$	—	—	—
RXJ1740.5 + 3539	a	10.3	0.26	1.62	0.07	—	—	—	—
	b	10.2	0.30	1.84	0.08	—	—	—	—
Z8276		9.4	0.28	1.72	0.10	$12.5^{+0.8}_{-0.7}$	$0.24^{+0.09}_{-0.10}$	$0.16^{+0.02}_{-0.03}$	$22.0^{+5.2}_{-4.7}$
Z8338		9.8	0.32	2.12	0.12	—	—	—	—
RXJ1750.2 + 3505		10.6	0.29	1.84	0.11	$15.0^{+3.7}_{-3.8}$*	—	—	—
A2292 [2]		—	0.09	2.10	0.06	$3.0^{+0.9}_{-0.9}$	—	—	—
Z8451		<13.3	0.41	1.61	0.14	—	—	—	—
RXJ2114.1 + 0234		10.2	0.30	1.90	0.10	—	—	—	—
Z8503		<19.7	0.25	2.55	0.13	—	—	—	—
RXJ2129.6 + 0005 [2]		9.9	0.24	1.66	0.13	$5.8^{+2.0}_{-1.9}$	—	—	—
A2390		9.9	0.31	1.35	0.19	$61.6^{+3.0}_{-3.3}$	$0.22^{+0.10}_{-0.11}$	$0.29^{+0.06}_{-0.06}$	$104.7^{+28.7}_{-23.78}$
A2409 [2]		<20.2	0.25	1.60	0.14	—	—	—	—
A2426		<14.6	0.29	1.21	0.12	—	—	—	—
A2428		<12.8	0.35	1.22	0.16	—	—	—	—
A2443		11.2	0.30	1.97	0.09	—	—	—	—
A2457		9.8	0.31	2.04	0.06	—	—	—	—
A2495		10.1	0.17	1.65	0.12	$2.0^{+0.5}_{-0.5}$	—	—	—
Z8852		9.9	0.30	1.92	0.09	—	—	—	—
A2572a	a	9.1	0.33	2.04	0.06	—	—	—	—
	b	9.9	0.33	2.00	0.07	—	—	—	—
A2572b		9.2	0.28	1.86	0.09	—	—	—	—
A2589		9.1	0.31	1.89	0.09	—	—	—	—
A2593		9.6	0.31	1.91	0.09	—	—	—	—
A2626	a	10.3	0.27	1.87	0.08	—	—	—	—
	b	10.2	0.29	1.95	0.08	$1.1^{+0.4}_{-0.4}$	—	—	—

Table 4 – *continued*

Cluster		aperture size (kpc)	Mg_2 index	4000-Å break	δBR	$L(H\alpha)$ (10^{40}erg/s)	$E(B-V)$	revised δBR	revised $L(H\alpha)$ (10^{40}erg/s)
A2627	a	<18.0	0.14	1.22	0.27	—	—	—	—
	b	<17.4	0.29	2.28	0.07	—	—	—	—
A2631		<31.5	0.24	2.12	0.10	—	—	—	—
A2634		9.8	0.32	1.85	0.09	$1.3^{+0.4}_{-0.6}$	—	—	—
A2657		9.9	0.27	1.83	0.10	—	—	—	—
A2665		10.5	0.29	1.82	0.09	$[0.6^{+0.3}_{-0.3}]$	—	—	—
A2675		10.7	0.25	1.91	0.09	—	—	—	—

Notes:
1. FOS spectrum with very little flux below 4000 Å, suggesting that the slit was not at the parallactic angle (see also spectra in Fig. 2).
2. The spectrum is very noisy.
* The Hα affected by a cosmic ray hit.
The FOS spectra in A92 and C95 were reduced using an optimal extraction technique, so the precise aperture from which the spectrum is taken is not known for each galaxy; we give the upper limit from the slit length of 6 arcsec in column 2. The aperture used for extracting the spectra in C95 taken with the ISIS on the WHT is not known.
The 4000-Å break in column 4 is measured from an f_λ spectrum rather than f_ν. Bracketed values mark where an abnormal value is due to loss of blue light from the slit.
The Hα line luminosity in column 6 is measured for the spectrum taken from the given aperture and does *not* represent the total line luminosity from the galaxy. A bracketed line luminosity shows where the line flux may have been reduced by atmospheric absorption.
The $E(B-V)$ in column 7 has been estimated from the Hα/Hβ ratio in the spectrum from the given aperture, and *not* from the total line fluxes given in Tables 5 and 6.
The 'revised' δBR in column 8, and the 'revised' Hα luminosity in column 9 are after the spectrum has been corrected for internal reddening by the amount shown in column 7.
Notes on individual galaxies:
A1437 There is overlap between the 10-kpc apertures taken for each component of the dumbbell galaxy.
RXJ1206.5 + 2810 The centre of the aperture was taken as midway between the two galaxy components.
RXJ1750.2 + 3505 The Hα emission is badly affected by a cosmic ray hit.
A2626 The 10 kpc aperture for each galaxy overlaps.

A92 and C95, though with a larger spread probably due to the less accurate sky subtraction obtained with the shorter FOS slit. There are also two blue non line emitters from these data (A1682a and A1902 with δBR of 0.19 and 0.23 respectively, discarding A689 as a probable AGN). Fig. 15 shows that there is a similar trend of reduced D_{4000} with increasing Hα luminosity, again with the distribution of D_{4000} for the 10-kpc-aperture *non*-line-emitting galaxies plotted at the arbitrary value of $L(H\alpha) = 3\times 10^{38}$ erg s^{-1}.

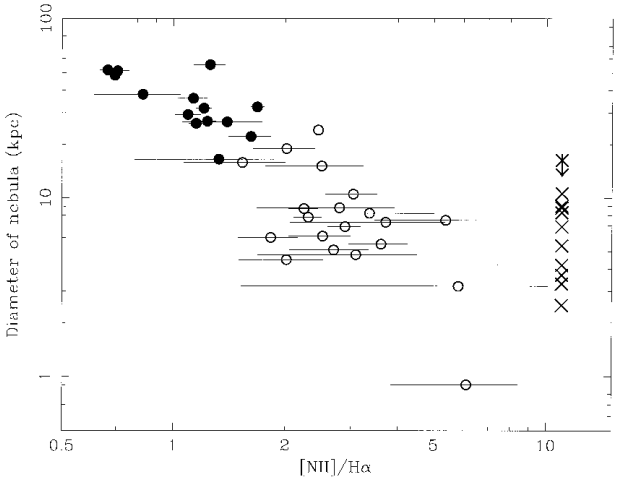

Figure 9. Ratio of [N II]λ6584/Hα plotted against the diameter of the nebula for all galaxies where this could be determined. Symbols are the same as in Fig. 7, with the [N II]-only emitting galaxies shown at an arbitrary value of [N II]/Hα of 11.

Most of the non-line-emitting galaxies have stellar indices of $1.6 < D_{4000} < 2.0$, the only exception being A1366 with a D_{4000} of 1.24. Six further non-line-emitting galaxies have values of $D_{4000} < 1.5$ from the FOS data (A761, Z5604, A1703, A1902, A2426 and A2428), but we note that these data are more susceptible to inaccurate sky subtraction due to the short slit, and thus the D_{4000} is much less certain.

3.11 Stellar populations

The spectra of many of the line-luminous BCGs show evidence of a young stellar population; the best (and most extreme) example is the central galaxy in A1835, which shows clear Balmer absorption lines (Fig. 16). We construct a co-added spectrum from the two *new* IDS observations of this galaxy, and note that at the spectral resolution afforded by these data we can independently confirm the appearance of a broad He IIλ4686 feature (Fig. 16; cf. Allen 1995, who also shows the central galaxy in A1068 to have Wolf–Rayet features). We have searched for such features in other line-emitting galaxies, but the low signal-to-noise ratios of most spectra preclude any other definite detection.

Once corrected for intrinsic reddening, many of the line-emitting galaxies show very prominent UV/blue continua with a clear Balmer break at 3646 Å, again both indicative of a population of massive stars. Assuming that the excess blue continuum of the central cluster galaxies is due to massive young stars rather than a power-law continuum, we characterize the stellar population by a simple spectral analysis (cf. Crawford & Fabian 1993; Allen 1995). We examine all the BCG spectra (extracted from the central apertures, shown in Tables 4 and 7 and corrected for intrinsic reddening) with Hα in emission. The galaxy spectra are fitted over

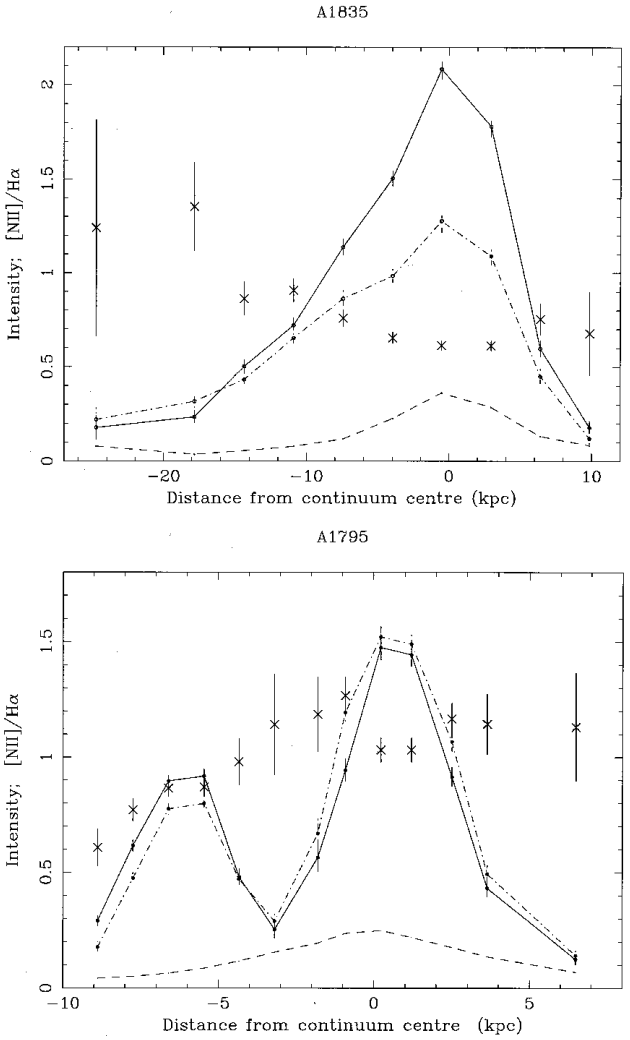

Figure 10. The spatial profile of the Hα (solid line), [N II]λ6584 (dot-dashed line) and red continuum (dashed line) along the slit for the central galaxy in A1835 (top) and A1795 (bottom). The *y*-axis is in units of 10^{-15} erg cm^{-2} s^{-1} for line intensities, and of 10^{-16} erg cm^{-2} s^{-1} (A1835) and 5×10^{-15} erg cm^{-2} s^{-1} (A1795) for the continuum. The crosses give the values of the intensity ratio [N II]/Hα at each row along the slit.

the rest-frame wavelength range 3300–5400 Å by the spectra of the template elliptical galaxy and model stellar atmospheres (Kurucz 1979). For simplicity, we use only templates of O5, B5, A5 and F5 stellar types, and let the normalization of each and the elliptical galaxy vary as free parameters in the fitting. The emission lines of [O II] and Hβ, [O III] and [N I] were masked out of the BCG spectrum before fitting, and the data are smoothed by 3 pixels. We do not attempt to fit those galaxies where the spectrum is either too noisy (A478) or shows a marked loss of blue light from the slit (i.e., A2294, RXJ0338.7+0958, RXJ0352.9+1941, RXJ0439.0+0520 and Z3916). We include the high-ionization systems (A2146 and A1068), but not the low-ionization system (RXJ0821.0+0752) with the very high value of intrinsic reddening.

The composition of the best-fitting stellar models are shown in Table 7, with each component given as a fraction of the total continuum at (rest-frame) 4500 Å. The errors on the components are the $\Delta\chi^2 = 1$ confidence limits for the components in the model, and do not encompass the range in the estimate of $E(B-V)$ from

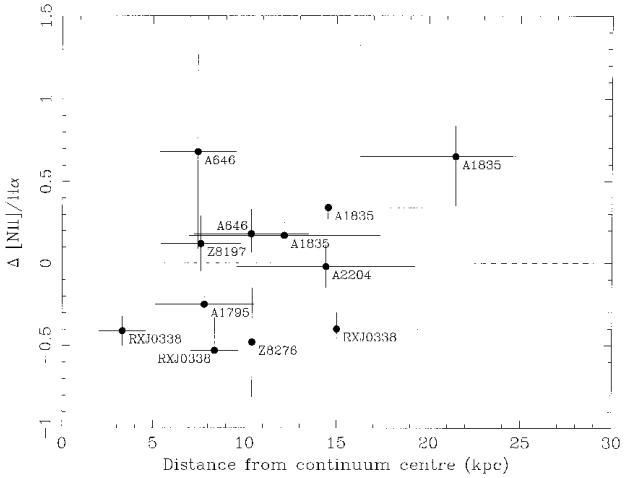

Figure 11. The difference in the intensity ratio of [N II]/Hα from the central value (Δ[N II]/Hα), as a function of distance from the continuum centre. The dashed line marks Δ[N II]/Hα of zero, i.e., no change in value between the centre of the galaxy and the spatially extended line emission.

Table 4. Examples of the best-fitting stellar models are shown in Fig. 17. The differing results between the three observations of A1835 is most likely due to the long slits sampling a slightly different position of the galaxy each time (the emission-line nebulae and blue light distribution are not necessarily symmetric; e.g. McNamara & O'Connell 1993). Although a few of the spectra are the same as those modelled in a similar manner by Allen (1995), we find a subtly different balance of massive stars required by the fits, mainly due to both the lesser values of $E(B-V)$ inferred from our Balmer line ratios and the use of a different elliptical galaxy template. The only galaxy for which we could not achieve any satisfactory fit using stellar models was that in Z8193. In all galaxies where the stellar components were fitted to a spectrum extracted from a ~10-kpc aperture, the monochromatic rest-wavelength 4500-Å luminosity of underlying galaxy component is within the range of the 24 non-emission-line galaxies used to construct the elliptical template ($0.08-3.11\times10^{40}$ erg s^{-1} Å^{-1} from the 10-kpc aperture, with an average of 0.96×10^{40} erg s^{-1} Å^{-1}).

Most of the best-fitting models to the high-Hα-luminosity systems require a fraction of O5 stars (from Z3146 at 58 per cent to Z7160 at 2 per cent), whereas few of the lower Hα-luminosity systems require any O5 stars. The fluxes of each stellar component are converted to a number of stars, assuming monochromatic 4500-Å luminosities of $\sim2.7\times10^{34}$, $\sim2.5\times10^{32}$, $\sim1.3\times10^{31}$ and $\sim1.6\times10^{30}$ erg s^{-1} Å^{-1} for O5, B5, A5 and F5 stellar types respectively. The number of O5 stars inferred from the best fits, as well as the number ratios of the different stellar types are listed for each best-fitting model in Table 8. The rate of visible star formation inferred by our model fits is also shown in Table 8. We assume a constant rate of formation, and stellar lifetimes of 3.66×10^6, 2.65×10^7, 4.78×10^8 and 2.11×10^9 yr for O5, B5, A5 and F5 stars respectively (from Shapiro & Teukolsky 1983). The visible star formation rates are quoted for the *total* area covered by the slit aperture (given in Table 7) – conversion to a star formation rate per kpc is non-trivial, and depends on the assumed radial profile of the excess blue light. We confirm the finding of Allen (1995) that in all cases, the number of lower mass stars in relation to the O stars exceeds predictions from either continuous formation (at a constant rate) or a single burst of star formation with a 'normal' Scalo IMF. The exceptions to this are the BCGs whose spectra only need an

Table 5. Red emission-line fluxes (in units of 10^{-15} erg cm^{-2} s^{-1}).

Cluster	log L(Hα)	Size (kpc)	Hα	[N II]λ6584	[S II]λ6717	[S II]λ6731	[O I]λ6300	[O I]λ6363
Z235	40.61	—	$1.3^{+0.2}_{-0.2}$	$2.3^{+0.2}_{-0.2}$	$0.9^{+0.3}_{-0.3}$	$0.6^{+0.3}_{-0.3}$	<0.1	<0.1
A115	41.33	38.0	$1.2^{+0.2}_{-0.2}$	$1.0^{+0.2}_{-0.2}$	$0.2^{+0.2}_{-0.2}$	$0.6^{+0.2}_{-0.2}$	<0.1	[—]
RXJ0107.4 + 3227	39.72	4.5	$3.9^{+0.9}_{-0.9}$	$7.9^{+0.4}_{-1.0}$	$1.2^{+1.1}_{-0.9}$	[$1.4^{+0.6}_{-1.2}$]	<0.1	<0.2
RXJ0123.2 + 3327	—	3.3	<0	$7.0^{+2.0}_{-1.6}$	—	—	—	—
A262	39.74	6.9	$4.6^{+0.4}_{-0.4}$	$13.3^{+0.5}_{-0.5}$ *	$4.2^{+0.5}_{-0.5}$	[$2.9^{+0.5}_{-0.4}$]	$0.3^{+0.4}_{-0.3}$	<0.1
A291	41.66	—	$2.5^{+0.1}_{-0.1}$	$2.0^{+0.1}_{-0.1}$	$1.5^{+0.1}_{-0.1}$	$0.7^{+0.1}_{-0.1}$	$0.6^{+0.1}_{-0.1}$	$0.2^{+0.1}_{-0.1}$
A400 a	—	3.7	<0	$7.4^{+1.8}_{-1.6}$	[—]	[—]	—	—
A400 b	—	2.5	<0	$3.5^{+1.3}_{-0.9}$	[—]	[—]	—	—
A401	—	10.6	<0	$0.9^{+0.3}_{-0.3}$	—	—	—	—
Z808	40.67	—	$0.4^{+0.1}_{-0.4}$	$0.8^{+0.2}_{-0.1}$	$0.2^{+0.1}_{-0.1}$	<0.1	<0.1	<0.1
RXJ0338.7 + 0958	41.25	31.8	$35.3^{+1.3}_{-1.2}$	$42.7^{+1.3}_{-1.3}$	$14.8^{+1.3}_{-1.3}$	$11.2^{+1.3}_{-1.4}$	$9.2^{+1.2}_{-1.2}$	$4.6^{+1.2}_{-1.2}$
RXJ0352.9 + 1941	41.77	—	$10.7^{+0.2}_{-0.3}$	$9.8^{+0.3}_{-0.2}$	$5.8^{+0.3}_{-0.3}$	$3.9^{+0.3}_{-0.2}$	$2.5^{+0.2}_{-0.2}$	$0.9^{+0.2}_{-0.2}$
A478	41.03	—	$3.3^{+0.2}_{-0.2}$	$3.7^{+0.2}_{-0.2}$	$1.5^{+0.2}_{-0.2}$	$1.1^{+0.2}_{-0.2}$	$0.9^{+0.2}_{-0.2}$	$0.5^{+0.2}_{-0.2}$
RXJ0439.0 + 0520	42.04	—	$5.4^{+0.1}_{-0.2}$	$8.1^{+0.2}_{-0.1}$	$3.1^{+0.2}_{-0.2}$	$1.9^{+0.2}_{-0.1}$	$0.9^{+0.1}_{-0.1}$	$0.4^{+0.1}_{-0.1}$
Z1121	40.16	—	$0.5^{+0.1}_{-0.1}$	$0.7^{+0.1}_{-0.1}$	<0.1	<0.1	<0.1	<0.1
RXJ0751.3 + 5012 b	39.81	8.2	$2.7^{+0.9}_{-1.6}$	$8.9^{+1.2}_{-1.1}$	[—]	[—]	<0.4	<0.2
A611	—	—	<0	$0.4^{+0.2}_{-0.1}$	<0.1	<0.1	<0.1	<0.1
RXJ0821.0 + 0752	41.48	—	$5.5^{+0.2}_{-0.2}$	$2.7^{+0.2}_{-0.1}$	$1.1^{+0.2}_{-0.2}$	$0.5^{+0.2}_{-0.2}$	<0.2	<0.1
A646	41.41	29.3	$3.5^{+0.2}_{-0.2}$	$3.8^{+0.2}_{-0.2}$	$1.5^{+0.2}_{-0.2}$	[$0.5^{+0.2}_{-0.2}$]	$0.9^{+0.2}_{-0.2}$	$0.4^{+0.2}_{-0.2}$
Z1665	<39.36	5.4	<0.5	$3.1^{+0.4}_{-0.5}$	[—]	—	—	—
A671	—	—	[<0]	[$3.0^{+0.9}_{-0.8}$]	—	—	—	—
A750	—	<16.3	<0	$0.4^{+0.1}_{-0.1}$	—	—	—	—
A795	41.29	22.1	$2.3^{+0.2}_{-0.3}$	$3.8^{+0.3}_{-0.3}$	[—]	[—]	$1.1^{+0.2}_{-0.2}$	$0.3^{+0.2}_{-0.2}$
Z2701	40.94	—	$0.4^{+0.1}_{-0.1}$	$0.8^{+0.2}_{-0.1}$	$0.3^{+0.2}_{-0.1}$	$0.2^{+0.2}_{-0.2}$	<0.2	<0.2
RXJ1000.5 + 4409 a	40.35	—	$0.2^{+0.1}_{-0.1}$	$0.5^{+0.1}_{-0.1}$	$0.2^{+0.1}_{-0.1}$	$0.1^{+0.1}_{-0.1}$	$0.1^{+0.1}_{-0.1}$	<0.1
RXJ1000.5 + 4409 b	40.34	—	$0.2^{+0.1}_{-0.1}$	$0.3^{+0.1}_{-0.1}$	<0.1	<0.1	<0.1	<0.1
Z3146	42.85	—	$17.1^{+0.4}_{-0.3}$	$13.5^{+0.3}_{-0.3}$	$6.5^{+0.4}_{-0.3}$	$5.3^{+0.4}_{-0.4}$	$3.5^{+0.3}_{-0.3}$	$0.9^{+0.3}_{-0.3}$
Z3179	40.92	—	$0.9^{+0.2}_{-0.4}$	$3.2^{+0.4}_{-0.3}$	$0.6^{+0.3}_{-0.3}$	$0.8^{+0.3}_{-0.2}$	$0.5^{+0.2}_{-0.2}$	<0.1
A1023	—	—	<0	$1.0^{+0.3}_{-0.3}$	—	—	—	—
A1068	42.24	—	$19.5^{+0.6}_{-0.4}$	$24.6^{+0.3}_{-0.6}$	$5.2^{+0.6}_{-0.4}$	$4.4^{+0.4}_{-0.6}$	$2.8^{+0.4}_{-0.4}$	$1.2^{+0.4}_{-0.4}$
A1084	40.91	—	$1.0^{+0.2}_{-0.2}$	$1.2^{+0.2}_{-0.2}$	$0.6^{+0.3}_{-0.3}$	$0.1^{+0.3}_{-0.1}$	$0.4^{+0.1}_{-0.1}$	$0.1^{+0.1}_{-0.1}$
A1204	41.03	—	$0.8^{+0.1}_{-0.1}$	$1.1^{+0.1}_{-0.1}$	$0.3^{+0.1}_{-0.1}$	$0.3^{+0.1}_{-0.1}$	$0.3^{+0.1}_{-0.1}$	$0.2^{+0.1}_{-0.1}$
Z3916	41.48	—	$1.5^{+0.1}_{-0.1}$	$1.7^{+0.1}_{-0.1}$	$1.1^{+0.1}_{-0.1}$	$0.5^{+0.1}_{-0.1}$	[—]	[—]
A1361	41.13	—	$2.2^{+0.2}_{-0.1}$	$3.6^{+0.2}_{-0.1}$ *	$1.4^{+0.1}_{-0.2}$	$0.6^{+0.2}_{-0.1}$	$0.4^{+0.1}_{-0.1}$	$0.4^{+0.1}_{-0.1}$
RXJ1206.5 + 2810	39.80	6.0	$1.8^{+0.3}_{-0.3}$	$3.4^{+0.3}_{-0.3}$	[—]	[—]	<0.1	<0.1
Z4905	<39.60	6.9	<0.2	$0.9^{+0.2}_{-0.2}$	—	[—]	—	—
RXJ1223.0 + 1037	39.71	6.1	$1.8^{+0.3}_{-0.3}$	$4.4^{+0.3}_{-0.3}$	[—]	[—]	$0.1^{+0.3}_{-0.1}$	<0.1
RXJ1230.7 + 1220	39.11	0.9	$23.2^{+7.8}_{-9.2}$	$142.2^{+10.1}_{-8.6}$	$20.3^{+7.8}_{-8.3}$	$38.3^{+8.9}_{-7.9}$	[<1.6]	<1.9
A1664	42.06	—	$15.2^{+0.4}_{-0.3}$	$10.5^{+0.3}_{-0.3}$	$5.7^{+0.3}_{-0.3}$	$4.7^{+0.3}_{-0.3}$	$2.4^{+0.2}_{-0.2}$	$0.8^{+0.2}_{-0.2}$
A1668	40.37	10.5	$1.3^{+0.2}_{-0.2}$	$3.9^{+0.2}_{-0.2}$	$1.2^{+0.2}_{-0.2}$	$0.5^{+0.2}_{-0.2}$	$0.6^{+0.2}_{-0.2}$	$0.1^{+0.2}_{-0.2}$
RXJ1320.1 + 3308 a	39.74	4.8	$1.0^{+0.4}_{-0.4}$	$3.0^{+0.4}_{-0.4}$	[<0.3]	$0.9^{+0.4}_{-0.4}$	<0.2	<0.1
A1767	—	9.0	<0	$1.8^{+0.5}_{-0.4}$	[—]	[—]	—	—
A1795	41.07	26.2	$6.9^{+0.2}_{-0.2}$	$7.9^{+0.2}_{-0.2}$	$4.0^{+0.3}_{-0.2}$	$2.9^{+0.3}_{-0.3}$	$1.9^{+0.2}_{-0.2}$	$0.7^{+0.2}_{-0.2}$
A1835	42.43	48.5	$8.8^{+0.2}_{-0.2}$	$6.1^{+0.2}_{-0.2}$	$2.7^{+0.2}_{-0.2}$	$2.4^{+0.2}_{-0.2}$	$2.1^{+0.2}_{-0.2}$	$0.6^{+0.2}_{-0.2}$
	42.37	51.9	$7.7^{+0.2}_{-0.2}$	$5.1^{+0.2}_{-0.2}$	$2.7^{+0.2}_{-0.2}$	$2.2^{+0.2}_{-0.2}$	$1.8^{+0.2}_{-0.2}$	$0.3^{+0.2}_{-0.2}$
	42.50	—	$10.4^{+0.2}_{-0.2}$	$7.7^{+0.2}_{-0.2}$	$3.4^{+0.2}_{-0.2}$	$2.2^{+0.2}_{-0.2}$	$1.9^{+0.2}_{-0.2}$	$0.7^{+0.18}_{-0.18}$
A1885	40.73	—	$1.5^{+0.1}_{-0.1}$	$1.7^{+0.1}_{-0.1}$	$0.8^{+0.1}_{-0.1}$	$0.3^{+0.1}_{-0.1}$	$0.5^{+0.1}_{-0.1}$	$0.1^{+0.1}_{-0.1}$
A1930	40.38	15.1	$0.3^{+0.1}_{-0.1}$	$0.8^{+0.1}_{-0.1}$	[—]	[—]	$0.1^{+0.1}_{-0.1}$	<0.1
RXJ1442.2 + 2218	40.65	24.0	$1.1^{+0.2}_{-0.2}$	$2.7^{+0.2}_{-0.2}$	$0.2^{+0.2}_{-0.2}$	$1.1^{+0.2}_{-0.2}$	[—]	$0.1^{+0.2}_{-0.2}$
RXJ1449.5 + 2746	<39.30	4.2	<0.5	$5.2^{+1.3}_{-1.1}$	[—]	—	—	—
A1991	40.08	8.8	$0.8^{+0.2}_{-0.3}$	$2.1^{+0.2}_{-0.3}$	$1.1^{+0.3}_{-0.3}$	$0.7^{+0.3}_{-0.3}$	[$0.4^{+0.3}_{-0.2}$]	$0.4^{+0.3}_{-0.2}$
Z7160	41.70	—	$1.6^{+0.2}_{-0.1}$	$1.4^{+0.1}_{-0.1}$	$0.8^{+0.2}_{-0.1}$	$1.0^{+0.1}_{-0.2}$	$0.6^{+0.1}_{-0.1}$	$0.3^{+0.1}_{-0.1}$
A2009	41.09	26.7	$1.1^{+0.2}_{-0.2}$	[$1.6^{+0.2}_{-0.2}$]	$1.0^{+0.3}_{-0.2}$	$0.3^{+0.2}_{-0.3}$	$0.2^{+0.3}_{-0.3}$	<0.1
A2033	<40.05	8.3	<0.4	$1.5^{+0.2}_{-0.2}$	—	—	—	—
A2052	40.47	8.7	$5.5^{+0.4}_{-0.5}$	$12.3^{+0.5}_{-0.5}$	$3.9^{+0.4}_{-0.5}$	$2.6^{+0.5}_{-0.4}$	$1.6^{+0.4}_{-0.4}$	$0.1^{+0.4}_{-0.4}$
A2055 a	—	8.8	<0	$1.1^{+0.2}_{-0.2}$	—	—	—	—
A2072	40.68	18.9	$0.7^{+0.1}_{-0.1}$	$1.3^{+0.1}_{-0.1}$	$0.4^{+0.1}_{-0.1}$	[—]	$0.2^{+0.1}_{-0.1}$	<0.1
RXJ1532.9 + 3021	42.78	51.3	$9.2^{+0.5}_{-0.3}$	$6.5^{+0.4}_{-0.3}$	$3.7^{+0.4}_{-0.4}$	$2.9^{+0.4}_{-0.4}$	$1.9^{+0.4}_{-0.4}$	$0.6^{+0.4}_{-0.4}$
A2146	42.15	—	$5.4^{+0.2}_{-0.2}$	$9.2^{+0.2}_{-0.2}$	$2.2^{+0.2}_{-0.2}$	$2.8^{+0.2}_{-0.2}$	$0.9^{+0.1}_{-0.1}$	$0.4^{+0.1}_{-0.1}$
A2199	40.44	7.8	$6.5^{+0.4}_{-0.6}$	$14.9^{+0.7}_{-0.5}$	[$3.1^{+0.5}_{-0.6}$]	$2.2^{+0.6}_{-0.5}$	$0.9^{+0.4}_{-0.4}$	$0.2^{+0.4}_{-0.4}$
A2204	42.29	55.4	$18.5^{+1.5}_{-1.3}$	[$23.3^{+1.4}_{-1.4}$]	$8.7^{+1.6}_{-1.4}$	$9.6^{+1.5}_{-1.6}$	$5.0^{+1.4}_{-1.3}$	$2.3^{+1.4}_{-1.3}$
RXJ1715.3 + 5725	40.09	5.5	$3.5^{+0.6}_{-0.6}$	$12.7^{+0.7}_{-0.7}$	[—]	$1.6^{+0.5}_{-0.7}$	[<0.3]	<0.2
Z8193	42.19	—	$10.7^{+0.2}_{-0.3}$	$6.2^{+0.3}_{-0.2}$	$3.4^{+0.2}_{-0.3}$	$2.1^{+0.3}_{-0.2}$	$1.9^{+0.2}_{-0.2}$	$0.7^{+0.2}_{-0.2}$
Z8197	41.33	26.9	$3.6^{+0.3}_{-0.2}$	$4.5^{+0.1}_{-0.2}$	$1.6^{+0.2}_{-0.2}$	$1.4^{+0.2}_{-0.2}$	$0.6^{+0.2}_{-0.2}$	$0.3^{+0.2}_{-0.2}$

Table 5 – *continued*

Cluster	log L(Hα)	Size (kpc)	Hα	[N II]λ6584	[S II]λ6717	[S II]λ6731	[O I]λ6300	[O I]λ6363
RXJ1720.1+2638	[41.18]	15.1	$[1.3^{+0.6}_{-0.6}]$	$[0.5^{+0.2}_{-0.1}]$	$1.1^{+0.2*}_{-0.1}$	$0.6^{+0.1}_{-0.2}$	$0.4^{+0.2}_{-0.1}$	$0.4^{+0.2}_{-0.1}$
A2294	41.48	—	$2.0^{+0.1}_{-0.1}$	$1.0^{+0.1}_{-0.1}$	$0.3^{+0.1}_{-0.1}$	$0.3^{+0.1}_{-0.1}$	$0.1^{+0.1}_{-0.1}$	<0.1
RXJ1733.0+4345	39.26	3.2	$0.4^{+0.3}_{-0.3}$	$2.2^{+0.3}_{-0.3}$	$[0.5^{+0.3}_{-0.3}]$	$0.4^{+0.3}_{-0.3}$	<0.1	<0.1
A2292	40.63	—	$0.7^{+0.2}_{-0.2}$	$1.4^{+0.1}_{-0.3}$	<0.1	<0.2	<0.3	<0.4
Z8276	41.23	32.3	$6.8^{+0.3}_{-0.3}$	$11.4^{+0.3}_{-0.3}$	$4.6^{+0.3}_{-0.4}$	$2.7^{+0.4}_{-0.3}$	$1.8^{+0.3}_{-0.3}$	$0.3^{+0.3}_{-0.3}$
RXJ1750.2+3505	41.23	15.8	$1.2^{+0.2}_{-0.1}$*	$2.9^{+0.1}_{-0.1}$	$0.7^{+0.2}_{-0.1}$	$0.2^{+0.2}_{-0.2}$	$0.3^{+1.3}_{-0.2}$	$0.2^{+1.3}_{-0.2}$
RXJ2129.6+005	41.05	16.5	$0.4^{+0.2}_{-0.1}$	$0.6^{+0.1}_{-0.1}$	<0.1	<0.1	$0.2^{+0.1}_{-0.1}$	<0.1
A2390	41.99	36.1	$3.8^{+0.3}_{-0.3}$	$4.3^{+0.3}_{-0.3}$	$1.9^{+0.3}_{-0.3}$	$0.5^{+0.3}_{-0.3}$	$1.0^{+0.3}_{-0.3}$	$0.1^{+0.3}_{-0.3}$
A2495	40.41	15.8	$0.9^{+0.2}_{-0.2}$	$1.4^{+0.2}_{-0.3}$	<0.2	<0.2	$0.2^{+0.2}_{-0.2}$	[—]
A2626 b	[39.96]	5.1	$[0.7^{+0.2}_{-0.1}]$	$1.8^{+0.2}_{-0.2}$	$0.6^{+0.1}_{-0.2}$	$0.7^{+0.2}_{-0.1}$	<0.1	<0.1
A2627 a	—	—	<0	$0.5^{+0.1}_{-0.1}$	—*	—*	<0.1	<0.1
A2627 b	—	—	$0.1^{+0.1}_{-0.1}$	$0.7^{+0.1}_{-0.2}$	<0.3	<0.3	<0.1	<0.1
A2634	40.12	7.5	$3.4^{+1.1}_{-1.3}$	$18.1^{+1.0}_{-1.1}$	[—]	$0.5^{+0.3}_{-0.5}$	<0.2	<0.3
A2665	39.81	7.3	$0.4^{+0.2}_{-0.2}$	$1.7^{+0.2}_{-0.2}$	$0.3^{+0.2}_{-0.2}$	$0.5^{+0.2}_{-0.2}$	<0.2	<0.1

Notes:
Hα luminosities are expressed in units of erg s^{-1}, and are the *total* slit luminosities, i.e., *not* those from the '10 kpc aperture'.
All fluxes are expressed in units of 10^{-15} erg cm^{-2} s^{-1}, and are the total flux from the slit.
Values in square brackets are affected by atmospheric absorption.
Hα in absorption is marked as <0.
Values marked by an asterisk are affected by a cosmic ray hit.

O-star population in addition to the elliptical galaxy template, which is compatible with a very recent single starburst. Over the wavelength range being modelled, however, the spectrum of O stars are fairly featureless, and the models can be equally well fitted by an elliptical galaxy diluted by a power-law continuum, albeit with a steep $f_\lambda \propto \lambda^{-3.5}$ spectral slope. Note that the limits on optical polarization observed in the blue light regions of central galaxies in the A1795 and A2597 clusters appears to rule out the possibility of a scattered nucleus as the origin of the blue light (McNamara et al. 1996a,c, 1999).

As originally mooted by JFN, young O stars will provide a major source of photoionization for the emission-line nebula (the less massive stars do not contribute significantly to the photoionization). We calculate the Hα luminosity resulting from photoionization by the O-star component required by each best-fitting stellar model given in Table 7, assuming that each star produces an Hα luminosity of 5.5×10^{36} erg s^{-1} (following Allen 1995), and that the covering fraction of the stars by the gas is unity. The comparison between the predicted and observed (corrected for intrinsic reddening) Hα luminosities is shown in Fig. 18. Those galaxies where the best-fitting stellar population did not require any O-stars are plotted at an arbitrary predicted Hα luminosity of 2×10^{39} erg s^{-1}. The errors on the predicted Hα in this plot are derived using only the errors on the stellar components in the spectral fitting, whereas there are also systematic uncertainties due to the amount of $E(B-V)$ inferred from the Balmer decrement. We repeat the stellar fits for each galaxy, now sampling the full range of $E(B-V)$ given in Table 4 where appropriate, and plot the enlarged errors for the these points by diamonds in Fig. 18. (A point with no error diamond around it is one not requiring any dereddening from the Balmer decrement, e.g., A2204.) Increasing the $E(B-V)$ to the maximum shown in Table 4 did not permit any O stars as part of the stellar composition in the central galaxies which did not require them in the first place. The data are broadly consistent with a large fraction of the observed Hα luminosity being provided by photoionization from a young stellar population (note that there will be a range of O-star subtypes present all contributing to the photoionization). Larger departures from this relationship may reflect the range of covering fractions present in the galaxies. In all this analysis, the distribution of the dust is unknown, and a large uncertainty remains about how well the reddening inferred from the line emission can be applied to the galaxy stellar continuum.

Surprisingly, a few of the lower Hα-luminosity systems are also close to this relation, although six of them (and two of the high-luminosity objects) do not have any predicted O5 stars to generate the observed line luminosity; this agrees with higher line intensity ratios seen in such systems, implying that a different ionization source dominates such systems.

We also carry out a simple stellar analysis for the only non-Hα-emitting galaxy out of the new IDS observations to show appreciable evidence for a blue continuum, A1366 (see Section 3.5). It requires an excess population of 12 per cent O5 stars and 3 per cent B5 stars at (rest-frame 4500 Å). It is also well fitted by a power-law component with slope of $f_\lambda \propto \lambda^{-3.3}$, containing 16 per cent of the flux at rest-frame 4500 Å.

4 DISCUSSION

4.1 Do brightest cluster galaxies differ between Abell and non-Abell clusters?

The X-ray flux selection used to compile the BCS has produced a sample of the most luminous clusters within $z < 0.3$. Although the bulk of the sample is formed from clusters selected through cross-correlation against optical catalogues, the BCS also includes clusters selected from their X-ray properties alone. In fact, one of the key aims of the BCS is to examine the optical differences between clusters of similar X-ray luminosity and redshift. Whilst the determination of a robust galaxy density (i.e., cluster richness) is beyond the scope of this paper, we can use the brightest cluster galaxy to make a preliminary comparison between optically selected and X-ray-selected clusters. From Table 1 we can state that 48 of the 51 BCS clusters within a redshift of 0.05 have a BCG that is optically catalogued (irrespective of its cluster environment) in either the MCG, NGC or IC optical catalogues, and they are all

Table 6. Blue emission-line fluxes (in units of 10^{-15} erg cm^{-2} s^{-1}).

Cluster	[O II]λ3727	Hβ		[O III]λ5007		[N I]λ5199	
Z235	$1.5^{+0.5}_{-0.5}$	<0.4	$[0.5^{+0.2}_{-0.2}]$	<0.6	$[0.4^{+0.2}_{-0.2}]$	<0.1	—
A115	$1.4^{+0.1}_{-0.1}$	$0.2^{+0.1}_{-0.1}$	$[0.5^{+0.2}_{-0.2}]$	<0.1	$[0.2^{+0.2}_{-0.2}]$	— *	— *
RXJ0107.4 + 3227	<0.7	<0.2	$[1.7^{+0.6}_{-0.5}]$	<0.7	$[2.1^{+0.5}_{-0.5}]$	<0.3	—
A262	$6.1^{+1.0}_{-0.8}$	<0.5	$[2.0^{+0.5}_{-0.4}]$	$1.0^{+0.7}_{-0.7}$	$[2.2^{+0.4}_{-0.4}]$	<0.6	—
A291	$2.1^{+0.4}_{-0.4}$	$0.9^{+0.2}_{-0.2}$	$[1.0^{+0.1}_{-0.1}]$	$0.3^{+0.2}_{-0.1}$	$[0.3^{+0.1}_{-0.1}]$	<0.1	$[0.2^{+0.1}_{-0.1}]$
Z808	<0.7	<0.1	—	<0.2	—	<0.1	—
RXJ0338.7 + 0958	$57.1^{+9.3}_{-8.9}$	$4.7^{+1.8}_{-1.6}$	$[7.4^{+1.9}_{-1.7}]$	$3.2^{+1.6}_{-1.4}$	$[4.4^{+1.6}_{-1.5}]$	$4.4^{+1.5}_{-1.5}$	$[3.1^{+1.9}_{-1.6}]$
RXJ0352.9 + 1941	$5.0^{+0.3}_{-0.3}$	$2.0^{+0.2}_{-0.2}$	$[2.2^{+0.2}_{-0.2}]$	$1.4^{+0.2}_{-0.2}$	$[1.4^{+0.2}_{-0.2}]$	$0.7^{+0.2}_{-0.2}$	$[1.0^{+0.1}_{-0.1}]$
A478	<0.5	$0.9^{+0.4}_{-0.4}$	$[0.8^{+0.3}_{-0.3}]$	$0.5^{+0.4}_{-0.4}$	$[0.4^{+0.3}_{-0.3}]$	<0.5	$[0.2^{+0.2}_{-0.2}]$
RXJ0439.0 + 0520	$2.2^{+0.3}_{-0.3}$	$0.9^{+0.1}_{-0.1}$	$[1.1^{+0.1}_{-0.1}]$	$1.2^{+0.1}_{-0.1}$	$[1.3^{+0.1}_{-0.1}]$	$0.3^{+0.2}_{-0.2}$	$[0.3^{+0.1}_{-0.1}]$
Z1121	$0.2^{+0.4}_{-0.2}$	<0.5	—	<0.5	—	<0.1	—
RXJ0751.3 + 5012 b	$7.0^{+3.6}_{-2.9}$	<0.4	[<1.2]	$1.4^{+0.9}_{-0.9}$	$[1.6^{+0.6}_{-0.6}]$	<0.2	—
RXJ0821.0 + 0752	$0.4^{+0.4}_{-0.4}$	$0.2^{+0.2}_{-0.2}$	$[0.4^{+0.2}_{-0.2}]$	<0.2	$[1.0^{+0.2}_{-0.2}]$	<0.19	—
A646	$4.6^{+0.5}_{-0.5}$	$0.9^{+0.3}_{-0.2}$	$[1.1^{+0.2}_{-0.3}]$	$0.3^{+0.2}_{-0.2}$	$[0.3^{+0.2}_{-0.2}]$	$0.7^{+0.3}_{-0.3}$	$[0.4^{+0.2}_{-0.2}]$
A795	$3.3^{+0.3}_{-0.3}$	$0.2^{+0.2}_{-0.2}$	$[0.4^{+0.2}_{-0.2}]$	$0.5^{+0.2}_{-0.2}$	$[0.7^{+0.2}_{-0.2}]$	<0.1	[<0.1]
Z2701	$0.9^{+0.5}_{-0.5}$	$0.5^{+0.1}_{-0.1}$	$[0.6^{+0.1}_{-0.1}]$	$0.1^{+0.1}_{-0.1}$	$[0.1^{+0.1}_{-0.1}]$	$0.2^{+0.2}_{-0.1}$	$[0.4^{+0.1}_{-0.1}]$
RXJ1000.5 + 4409 a	$0.5^{+0.3}_{-0.3}$	$0.1^{+0.1}_{-0.1}$	$[0.1^{+0.1}_{-0.1}]$	$0.2^{+0.1}_{-0.1}$	$[0.2^{+0.1}_{-0.1}]$	<0.2	—
RXJ1000.5 + 4409 b	$0.5^{+0.4}_{-0.3}$	<0.1	—	<0.1	—	<0.1	—
Z3146	$15.0^{+0.4}_{-0.4}$	$4.6^{+0.2}_{-0.2}$	$[4.6^{+0.2}_{-0.2}]$	$2.6^{+0.2}_{-0.2}$	$[2.5^{+0.2}_{-0.2}]$	$1.4^{+0.1}_{-0.1}$	$[2.0^{+0.2}_{-0.2}]$
Z3179	$0.8^{+0.3}_{-0.3}$	$0.1^{+0.2}_{-0.1}$	$[0.2^{+0.2}_{-0.2}]$	$0.8^{+0.3}_{-0.3}$	$[0.8^{+0.3}_{-0.2}]$	<0.1	[<0.2]
A1068	$9.7^{+0.4}_{-0.4}$	$3.6^{+0.4}_{-0.4}$	$[4.1^{+0.4}_{-0.4}]$	$12.2^{+0.5}_{-0.5}$	$[12.6^{+0.5}_{-0.4}]$	$1.6^{+0.2}_{-0.2}$	$[1.8^{+0.4}_{-0.3}]$
A1084	<0.7	<0.2	—	<0.2	—	<0.1	—
A1204	$1.1^{+0.5}_{-0.4}$	<0.1	$[0.2^{+0.1}_{-0.1}]$	$0.1^{+0.1}_{-0.1}$	$[0.1^{+0.2}_{-0.1}]$	<0.1	[<0.1]
Z3916	$0.4^{+0.4}_{-0.3}$	$0.3^{+0.2}_{-0.1}$	$[0.4^{+0.2}_{-0.2}]$	$0.1^{+0.2}_{-0.1}$	$[0.2^{+0.1}_{-0.1}]$	<0.1	—
A1361	$3.4^{+0.5}_{-0.5}$	$0.8^{+0.2}_{-0.2}$	$[1.0^{+0.2}_{-0.2}]$	$0.9^{+0.2}_{-0.2}$	$[0.9^{+0.2}_{-0.2}]$	<0.3	—
RXJ1206.5 + 2810	<0.8	<0.5	—	<0.5	—	<0.2	—
RXJ1223.0 + 1037	<2.6	<1.0	—	<0.5	—	<0.6	—
RXJ1230.7 + 1220	$84.0^{+22.0}_{-19.4}$	<3.6	$[20.8^{+3.3}_{-3.1}]$	$7.6^{+7.0}_{-7.3}$	$[21.0^{+3.6}_{-3.4}]$	<7.5	—
A1664	$10.9^{+1.0}_{-1.1}$	$2.7^{+0.2}_{-0.2}$	$[2.9^{+0.2}_{-0.2}]$	$1.4^{+0.2}_{-0.2}$	$[1.5^{+0.2}_{-0.2}]$	$0.6^{+0.2}_{-0.2}$	$[1.1^{+0.3}_{-0.3}]$
A1668	$3.2^{+0.6}_{-0.6}$	$0.5^{+0.3}_{-0.3}$	$[1.0^{+0.2}_{-0.2}]$	$1.6^{+0.3}_{-0.3}$	$[1.7^{+0.2}_{-0.2}]$	$0.5^{+0.4}_{-0.3}$	$[0.5^{+0.1}_{-0.1}]$
RXJ1320.1 + 3308 a	<1.5	<0.5	$[0.6^{+0.5}_{-0.4}]$	$1.4^{+0.6}_{-0.6}$	$[1.2^{+0.3}_{-0.3}]$	<0.5	—
A1795	$11.4^{+0.9}_{-0.9}$	$1.4^{+0.3}_{-0.2}$	$[2.0^{+0.6}_{-0.5}]$	$1.2^{+0.2}_{-0.2}$	$[2.0^{+0.7}_{-0.6}]$	$1.2^{+0.4}_{-0.4}$	$[1.6^{+0.2}_{-0.2}]$
A1835	$6.7^{+0.2}_{-0.2}$	$1.8^{+0.1}_{-0.1}$	$[2.1^{+0.1}_{-0.1}]$	$1.3^{+0.1}_{-0.1}$	$[1.5^{+0.1}_{-0.1}]$	$0.5^{+0.1}_{-0.2}$	$[0.7^{+0.1}_{-0.2}]$
	$5.6^{+0.3}_{-0.3}$	$1.1^{+0.1}_{-0.1}$	$[1.2^{+0.1}_{-0.1}]$	$0.9^{+0.1}_{-0.1}$	$[1.0^{+0.2}_{-0.1}]$	$0.4^{+0.2}_{-0.2}$	$[0.4^{+0.2}_{-0.2}]$
	$6.3^{+0.4}_{-0.4}$	$1.8^{+0.1}_{-0.1}$	$[2.2^{+0.1}_{-0.1}]$	$1.6^{+0.1}_{-0.1}$	$[1.7^{+0.1}_{-0.1}]$	$0.6^{+0.2}_{-0.2}$	$[1.6^{+0.2}_{-0.2}]$
A1885	$2.2^{+0.5}_{-0.5}$	$1.0^{+0.3}_{-0.3}$	$[1.2^{+0.2}_{-0.2}]$	$0.5^{+0.3}_{-0.2}$	$[0.4^{+0.2}_{-0.2}]$	$0.2^{+0.2}_{-0.2}$	$[0.3^{+0.1}_{-0.1}]$
A1930	<0.4	<0.3	—	<0.3	—	<0.1	—
RXJ1442.2 + 2218	$3.1^{+0.7}_{-0.7}$	<0.2	$[0.4^{+0.4}_{-0.3}]$	$0.4^{+0.3}_{-0.3}$	$[0.7^{+0.4}_{-0.3}]$	<0.2	—
RXJ1449.5 + 2746	$2.7^{+0.9}_{-0.9}$	<0.2	[<0.9]	$0.3^{+0.2}_{-0.3}$	$[1.6^{+0.4}_{-0.4}]$	<0.5	—
A1991	$1.1^{+0.3}_{-0.3}$	<0.1	[<0.1]	$0.3^{+0.2}_{-0.3}$	$[0.4^{+0.4}_{-0.3}]$	<0.2	—
Z7160	$1.3^{+0.1}_{-0.1}$	$0.1^{+0.1}_{-0.1}$	$[0.3^{+0.1}_{-0.1}]$	<0.1	[<0.1]	<0.1	—
A2009	$1.2^{+0.3}_{-0.3}$	$0.2^{+0.2}_{-0.2}$	$[0.4^{+0.1}_{-0.3}]$	$0.1^{+0.2}_{-0.2}$	$[0.3^{+0.2}_{-0.3}]$	$0.2^{+0.2}_{-0.2}$	$[0.2^{+0.1}_{-0.1}]$
A2052	$7.5^{+0.8}_{-0.8}$	$0.6^{+0.5}_{-0.5}$	$[1.4^{+0.3}_{-0.3}]$	$5.7^{+0.6}_{-0.6}$	$[5.9^{+0.3}_{-0.3}]$	<0.3	$[0.7^{+0.2}_{-0.2}]$
A2072	$0.7^{+0.2}_{-0.2}$	$0.1^{+0.1}_{-0.1}$	$[0.3^{+0.1}_{-0.1}]$	$0.1^{+0.1}_{-0.1}$	$[0.2^{+0.1}_{-0.1}]$	<0.1	$[0.2^{+0.1}_{-0.1}]$
RXJ1532.9 + 3021	$9.2^{+0.2}_{-0.2}$	$2.5^{+0.1}_{-0.1}$	$[2.5^{+0.1}_{-0.1}]$	$1.4^{+0.1}_{-0.1}$	$[1.4^{+0.1}_{-0.1}]$	$0.7^{+0.1}_{-0.1}$	$[0.9^{+0.1}_{-0.1}]$
A2146	$4.6^{+0.7}_{-0.6}$	$1.4^{+0.2}_{-0.2}$	$[1.5^{+0.1}_{-0.1}]$	$10.7^{+0.3}_{-0.2}$	$[10.6^{+0.2}_{-0.2}]$	$0.4^{+0.1}_{-0.1}$	$[0.7^{+0.1}_{-0.1}]$
A2199	$8.9^{+1.3}_{-1.2}$	$0.7^{+0.3}_{-0.3}$	$[2.0^{+0.2}_{-0.2}]$	$1.6^{+0.3}_{-0.3}$	$[2.4^{+0.3}_{-0.3}]$	<0.1	$[0.8^{+0.1}_{-0.1}]$
A2204	$25.5^{+0.6}_{-0.6}$	$4.9^{+0.4}_{-0.4}$	$[5.6^{+0.2}_{-0.2}]$	$3.0^{+0.4}_{-0.4}$	$[3.8^{+0.2}_{-0.2}]$	$1.5^{+0.5}_{-0.5}$	$[2.7^{+0.3}_{-0.3}]$
RXJ1715.3 + 5726	$3.8^{+1.1}_{-1.0}$	<0.3	$[1.8^{+0.4}_{-0.4}]$	$0.7^{+0.8}_{-0.8}$	$[1.4^{+0.3}_{-0.3}]$	<0.2	$[1.0^{+0.3}_{-0.3}]$
Z8193	$8.5^{+0.7}_{-0.6}$	$2.2^{+0.4}_{-0.4}$	$[1.8^{+0.3}_{-0.3}]$	$1.4^{+0.3}_{-0.3}$	$[1.4^{+0.3}_{-0.3}]$	$1.2^{+0.5}_{-0.4}$	[<0.2]
Z8197	$4.4^{+0.3}_{-0.3}$	$0.6^{+0.1}_{-0.2}$	$[0.8^{+0.1}_{-0.1}]$	$0.5^{+0.1}_{-0.2}$	$[0.5^{+0.1}_{-0.1}]$	<0.2	$[0.3^{+0.1}_{-0.1}]$
RXJ1720.1 + 2638	$2.1^{+0.2}_{-0.2}$	$0.5^{+0.2}_{-0.1}$	$[0.7^{+0.1}_{-0.1}]$	<0.2	$[0.2^{+0.1}_{-0.1}]$	$0.2^{+0.1}_{-0.1}$	$[0.3^{+0.1}_{-0.1}]$
A2294	$0.4^{+0.1}_{-0.1}$	$0.6^{+0.2}_{-0.2}$	$[0.9^{+0.2}_{-0.2}]$	$0.9^{+0.1}_{-0.2}$	$[1.2^{+0.3}_{-0.3}]$	$0.2^{+0.1}_{-0.1}$	$[0.3^{+0.2}_{-0.2}]$
RXJ1733.0 + 4345	<0.7	<0.1	$[0.4^{+0.1}_{-0.1}]$	$0.3^{+0.3}_{-0.3}$	$[0.6^{+0.2}_{-0.2}]$	<0.1	$[0.1^{+0.1}_{-0.1}]$
A2292	<0.1	$0.4^{+0.3}_{-0.3}$	$[0.6^{+0.4}_{-0.4}]$	$0.1^{+0.1}_{-0.1}$	$[0.2^{+0.2}_{-0.2}]$	<0.1	—
Z8276	$9.0^{+0.7}_{-0.7}$	$1.7^{+0.3}_{-0.3}$	$[2.0^{+0.2}_{-0.2}]$	$1.6^{+0.3}_{-0.3}$	$[1.6^{+0.2}_{-0.2}]$	$0.3^{+0.3}_{-0.3}$	$[0.4^{+0.2}_{-0.2}]$
RXJ1750.2 + 3505	$1.5^{+0.1}_{-0.2}$	<0.3	$[0.5^{+0.2}_{-0.2}]$	$0.7^{+0.2}_{-0.2}$	$[0.7^{+0.2}_{-0.2}]$	<0.10	$[0.4^{+0.1}_{-0.1}]$
RXJ2129.6 + 0005	$0.7^{+0.1}_{-0.2}$	<0.2	$[0.2^{+0.1}_{-0.1}]$	< 0.1	[<0.2]	<0.1	$[0.2^{+0.1}_{-0.1}]$
A2390	$4.3^{+0.3}_{-0.3}$	$0.2^{+0.3}_{-0.2}$	$[1.1^{+0.2}_{-0.2}]$	$0.6^{+0.3}_{-0.3}$	$[1.0^{+0.2}_{-0.2}]$	<0.2	$[0.4^{+0.5}_{-0.4}]$
A2495	<0.7	<0.3	[<0.2]	<0.2	[<0.1]	<0.1	—
A2634	<3.2	<0.6	$[0.9^{+0.9}_{-0.9}]$*	$0.9^{+0.9}_{-0.9}$	$[1.9^{+0.9}_{-0.9}]$	<0.5	—
A2665	$1.4^{+0.5}_{-0.5}$	<0.2	$[0.5^{+0.1}_{-0.1}]$	<0.2	$[\ 0.1^{+0.1}_{-0.1}]$	<0.2	—

Notes:

We have tabulated values and upper limits for the blue emission-line fluxes in those clusters where only Hα or [O II]λ3727 are definitely detected.

The values of Hβ, [O III]λ5007 and [N I] tabulated in square brackets are measured in the 'residual' spectrum (i.e., after a scaled template galaxy has been subtracted). Where there is no value shown for a line flux for the residual spectrum, the values/limits are not improved from the original fit.

All fluxes are expressed in units of 10^{-15} erg cm^{-2} s^{-1} and are *total* fluxes from the slit.

Values marked by an asterisk are affected by a cosmic ray hit.

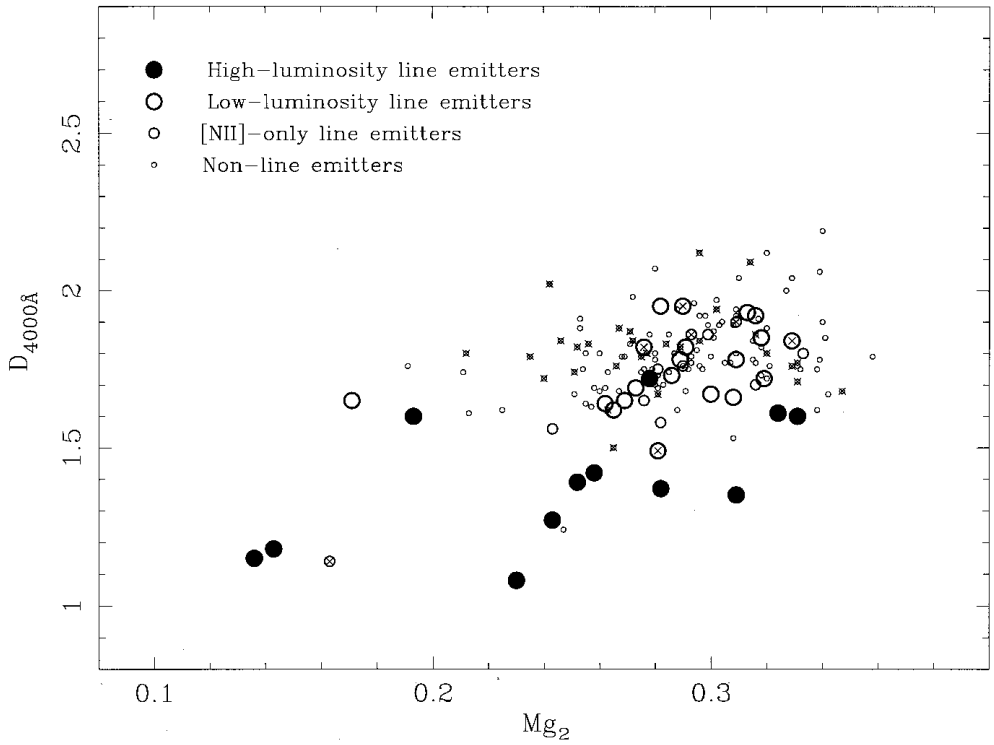

Figure 12. Plot of the 4000 Å break (D_{4000}) against the Mg_2 index, as measured from ∼10 -kpc central apertures only. Symbols are similar to previous figures: solid circles show high-luminosity emitters; large open circles show lower luminosity systems, [N II]-only line emitters and non-line emitters, dependent on the symbol size (see key). Galaxies that were not observed at the parallactic angle are marked also by a cross.

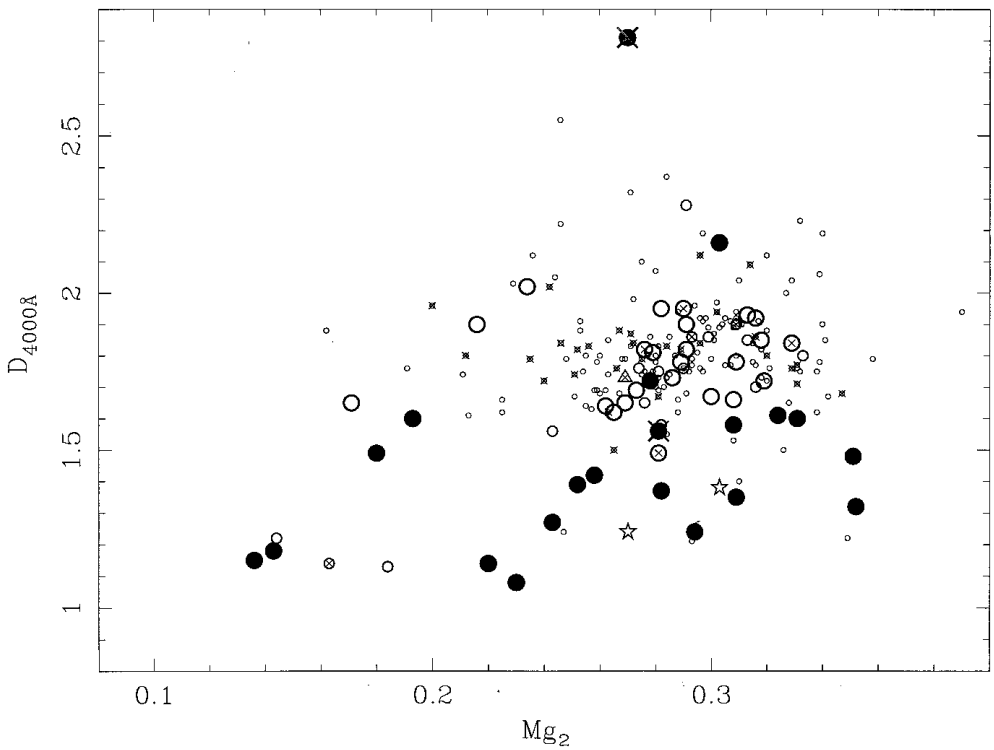

Figure 13. Plot of the 4000 Å break (D_{4000}) against the Mg_2 index, but now including the data from A92 and C95, which are not all from a 10 kpc aperture. Symbols as in previous figure.

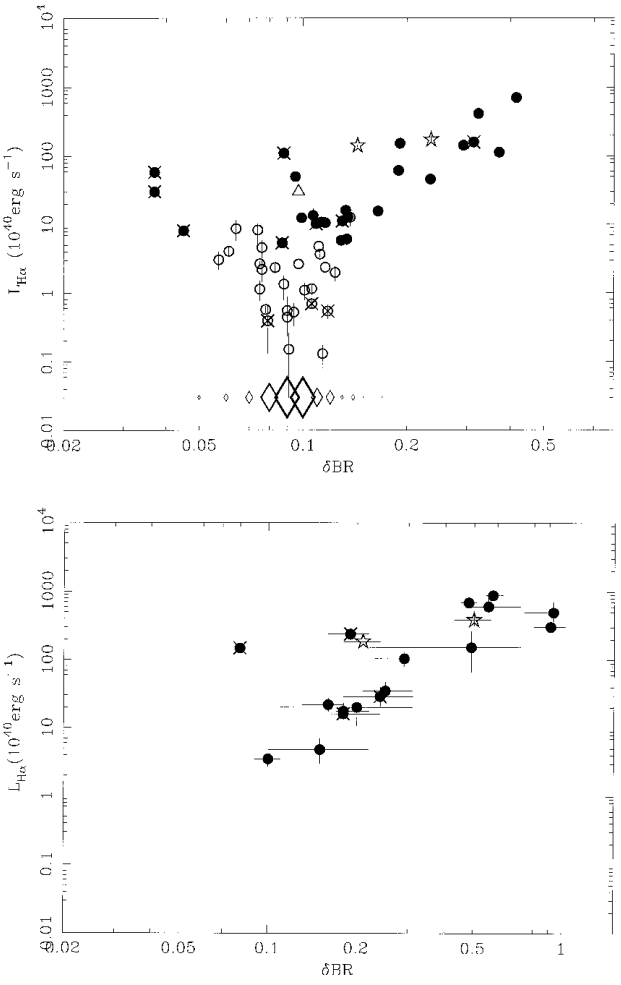

Figure 14. (Top) Plot of the δBR stellar index (see Section 3.5) against the Hα slit luminosity for all the Hα line emitters in this paper, for the apertures listed in Table 4. Symbols are as in previous figures, with crosses marking those galaxies not observed at the parallactic angle (these might preferentially lose blue light from the slit, and thus have a decreased δBR than expected from the Hα luminosity). The distribution of δBR observed for the 10 kpc aperture spectra of the non-line-emitting galaxies is shown by the diamonds at the arbitrary value of $L(\mathrm{H}\alpha) = 3 \times 10^{38}$ erg s^{-1}, with the size of the symbol proportional to the number of galaxies with that value of δBR. (Bottom) The same plot, but now only for those galaxies showing internal reddening (see Section 3.9), using 'corrected' values of both δBR and $L(\mathrm{H}\alpha)$.

(where indicated) elliptical galaxies. The three exceptions are RXJ0338.7 + 0958, RXJ0341.3 + 1524 and RXJ1205.1 + 3920, each of which is centred on a galaxy on the Palomar Sky Survey. The first source is the well-studied poor group 2A 0335 + 096 (e.g., Sarazin, Baum & O'Dea 1995a), the second is centred on an anonymous Zwicky galaxy (III Zw 054), and the third, while at much higher galactic latitude than the other two sources, is missing from all available optical catalogues. There are a number of optically catalogued central cluster galaxies beyond 0.05, but the fraction in both Abell and non-Abell clusters drops to essentially zero in these catalogues beyond a redshift of 0.075. These numbers clearly indicate that the brightest member galaxies of X-ray-selected clusters are almost always easily identified at $z < 0.05$, even if the cluster has itself been missed in optical cluster/group searches. This implies that none of the BCS clusters are intrinsically 'dark' and the brightest galaxies within them show a limited scatter in optical luminosity.

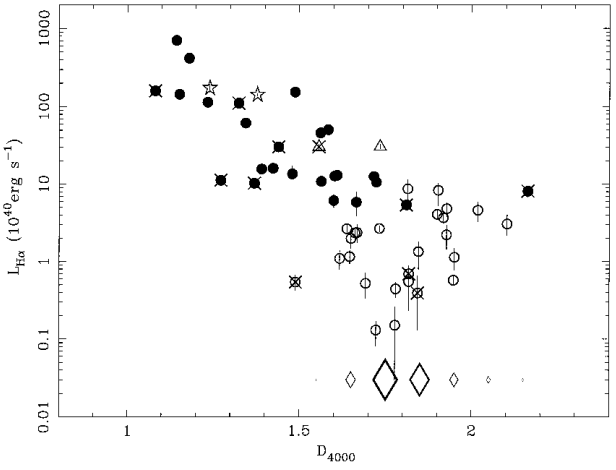

Figure 15. Plot of the 4000 Å break (D_{4000}) against the Hα slit luminosity for all the Hα line emitters in this paper (with the exception of RXJ0352.9+1941 which, with a D_{4000} of 2.8 is off the plot) for the apertures listed in Table 4. Symbols are as in previous figures, with crosses marking those galaxies not observed at the parallactic angle. The distribution of D_{4000} observed for the 10 kpc aperture spectra of the non-line-emitting galaxies is shown by the diamonds at an arbitrary value of $L(\mathrm{H}\alpha) = 3 \times 10^{38}$ erg s^{-1}, with the size of the symbol proportional to the number of galaxies with that value of D_{4000}.

4.2 Cooling flow nebulae

Around one-third of the BCGs in this paper show optical line emission of some degree – from those with low-level [N II]-only emission, to some of the brightest non-AGN line emitters known (Z3146, RXJ1532.9 + 3021). The Hα-emitting dominant galaxies show properties very similar to those at the centre of known cooling flow clusters (e.g., JFN; Heckman et al. 1989). We defer detailed discussion of whether individual clusters contain cooling flows until the X-ray compilation paper (Crawford et al., in preparation), but for the moment we assume that the majority of these systems are described as cooling flow nebulae (the few exceptions are discussed further in Section 4.3).

Central galaxies of cooling flow clusters have long been known to show luminous line emission, spatially extended in filaments spread over the central 5–60 kpc of the cluster core (e.g., Lynds 1970; Heckman 1981; Hu et al. 1985; JFN; Heckman et al. 1989; A92; C95). Such nebulae are too bright to be simply the recombination phase of the cooling gas in the intracluster medium (JFN); an additional local heat source is required – distributed throughout the optically emitting region of the core – to re-ionize the atoms many times in order to produce the observed luminosity (JFN; Johnstone & Fabian 1988; Heckman et al. 1989; Donahue & Voit 1991; Crawford & Fabian 1992). Despite this, the presence of such line emission is dependent on the cluster properties: large line luminosity extended emission-line regions are found in clusters with high cooling flow rates (JFN; Allen 1998), and so far such systems have *not* been found around BCGs in non-cooling flow clusters. Line emission is not, however, ubiquitous in BCGs contained in strong cooling flows (e.g., A2029, A2063), and occurs at around 32 per cent throughout our cluster sample, which includes non-cooling-flow clusters. There is a propensity for the emission-line systems to be associated with those BCGs which contain a central radio source (Heckman et al. 1989; C95), though again not exclusively (e.g., A1060). The probability of the BCG containing a central radio

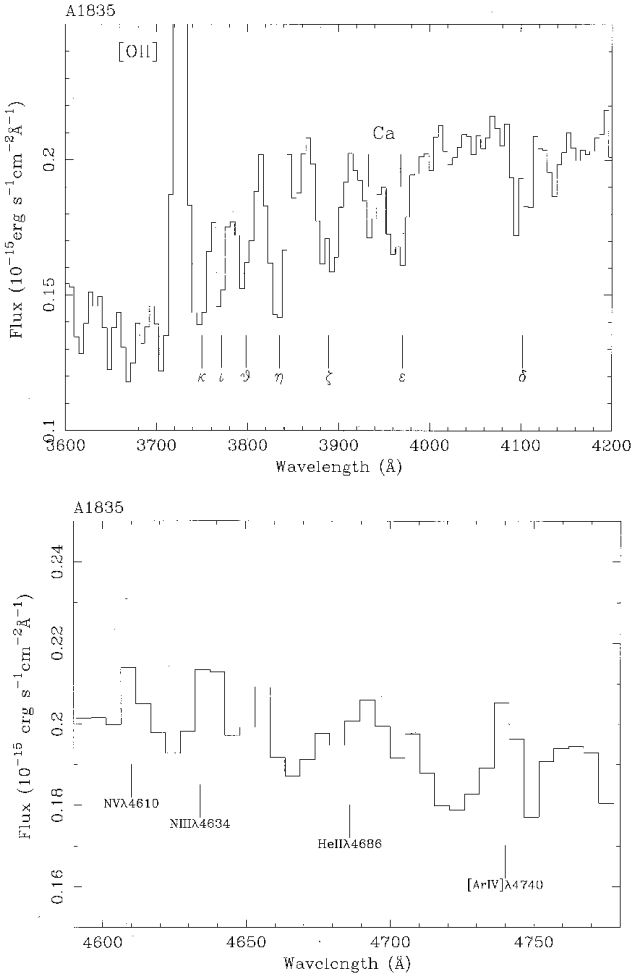

Figure 16. (Top) Co-added IDS (rest-frame) spectra of A1835, showing the clear signature of Balmer lines in absorption. [O II] in emission and the Ca absorption doublet are also marked. Note the false zero of the spectrum. (Bottom) Co-added spectrum of A1835 (in the rest-frame), showing the ~4650-Å Wolf–Rayet feature. Note the false zero of the spectrum.

source will, however, be again dependent on the general cluster properties. Further discussion of the relation between the optical properties of the BCG to the X-ray properties of the host cluster and any central radio source are postponed to the next papers in this series where the X-ray data and radio data are presented (Crawford et al., in preparation; Edge et al., in preparation).

4.2.1 High-Hα-luminosity cooling flow systems

Only the cooling flow nebulae with a high line luminosity [$L(\mathrm{H}\alpha) > 10^{41}$ erg s^{-1}] are accompanied by an excess ultraviolet/blue continuum (Figs 12 to 15; JFN). Both the line emission and the blue light are extended on scales of 5–60 kpc, and are seen to be spatially coincident from the flattening of the radial gradient of the Mg_2 spectral index within the emission-line regions (Cardiel et al. 1998). The morphology of the blue light also seems (in the few cases imaged) spatially related to that of the contained radio source (McNamara & O'Connell 1993; McNamara 1995; Sarazin et al. 1995b; McNamara et al. 1996a; McNamara 1997). The ultraviolet continuum has been successfully ascribed to massive young star formation, from both the spectra (once intrinsic reddening has been corrected; Allen 1995; Section 3.11) and from high-resolution images (McNamara et al. 1996a,b; Pinkney et al. 1996). The line ratios observed in these systems have strong Balmer lines relative to forbidden lines such as [O III], [N II] and [S II] (see Fig. 8; mean values around [N II]/Hα~0.8, [S II]/Hα~0.4, [O I]/Hα~0.2 and [O III]/Hβ~0.6). A good relation is found between the observed Hα luminosity (again corrected for intrinsic reddening) and that predicted from photoionization by the O stars predicted to be present from the stellar fit to the dereddened continuum (Allen 1995; Fig. 18). Detailed modelling of the BCG spectra (Johnstone & Allen, in preparation) indicates that the ionizing fluxes required to produce the emission-line ratios and luminosities observed in these systems can be fully accounted for by the observed O-star populations (assuming very hot stars, with $T > 40\,000$ K, and a low mean ionization parameter, $U \sim -4$) in a high-metallicity environment (about solar; see also Filippenko & Terlevich 1992 and Allen 1995). Together with the spatial correspondence of the blue light and line emission (Cardiel et al. 1998), it seems that the most line-luminous cooling flow nebulae are powered by a population of massive hot stars.

The additional stellar population is too centrally concentrated for the stars to be the immediate depository of gas cooling from the hot intracluster medium, as X-ray profiles of cooling flow clusters show the mass deposition to have a more distributed, flat profile (Fabian 1994, and references therein). Large masses of X-ray-absorbing material are detected in the spectra of cooling flow clusters (White et al. 1991; Allen & Fabian 1997), indicating that cold clouds can be an end-product of the cooling process. Such clouds might coagulate and condense to form a central reservoir of cold gas. As suggested by the double-lobed blue light morphology of A1795 and A2597, and as hypothesized by several authors (McNamara & O'Connell 1993; Pinkney et al. 1996; McNamara 1997), the interaction between the outflowing radio plasma and this gas reservoir could induce a massive starburst. The distribution of stellar types inferred is weighted to lower mass stars (Section 3.11 and Allen 1995), suggesting that such a starburst is triggered at irregular time-scales. Those galaxies requiring an excess population of just O stars (e.g., those in A291, Z3146, Z8276) may only have one very recent such starburst, whilst others may have aged such that few O stars remain. This scenario predicts that the very luminous systems are created by the *combination* of a central radio source and a surrounding mass of cold clouds accumulated from the cooling flow – both a common consequence of a rich (but non-binary) cluster environment. Thus it is possible a central radio source will not induce star formation and luminous line emission unless the cooling flow has accumulated a reservoir of cold gas. Hence any BCG in a cooling flow cluster that contains a strong radio source, yet no optical anomalies, should also lack evidence for intrinsic absorption in the cluster X-ray spectrum. A full examination of the correlations between cooling flow properties and both the type of line emission and presence of a central radio source will be addressed in the subsequent papers in this series.

The ionization state of the nebula in high-Hα-luminosity systems are seen to change away from the galaxy, but not in a consistent manner (Figs 10 and 11; see also S1101 in Crawford & Fabian 1992). As shown in Section 3.8, the variation is not simply caused by stellar Hα absorption in the galaxy continuum increasing the central value of [N II]/Hα derived, as the line ratios both drop and rise off-centre in different galaxies (Fig. 11). This change in line ratios is not easily ascribed to a radial metallicity gradient either, as any overabundance of nitrogen and sulphur would likely be concentrated toward the centre of the galaxy, producing a drop in the line ratios at larger radius.

Table 7. Percentages of the stellar components at (rest-frame) 4500 Å in the best fit to the BCG spectra. The BCG spectra were extracted from the aperture shown in column 2, and corrected for intrinsic reddening by the amount shown in the column marked $E(B-V)$. The monochromatic 4500-Å luminosity of the elliptical galaxy component to the fit shown in the final column.

Name	aperture (kpc)	$E(B-V)$	% O5	% B5	% A5	% F5	% Elliptical	L(Elliptical) (10^{40} erg s^{-1} Å^{-1})
A115	8.8	0.00	4 ± 1	—	4 ± 1	—	92 ± 1	0.61 ± 0.01
A291	<25.1	0.00	15 ± 1	—	—	—	85 ± 1	1.46 ± 0.01
RXJ0751.3 + 5012b	10.2	0.00	—	3 ± 2	—	—	97 ± 3	0.26 ± 0.01
A646	10.5	0.06	8 ± 1	—	—	9 ± 3	83 ± 3	0.48 ± 0.02
RXJ1000.5 + 4409	<21.0	0.00	—	—	—	22 ± 10	78 ± 11	0.43 ± 0.06
A795	8.8	0.00	5 ± 1	—	—	—	95 ± 1	0.68 ± 0.01
Z3146	<32.0	0.20	58 ± 1	—	—	—	42 ± 2	2.93 ± 0.12
A1068	<19.3	0.39	9 ± 2	27 ± 1	—	34 ± 1	30 ± 3	2.61 ± 0.27
A1361	<16.8	0.00	5 ± 1	—	—	—	95 ± 1	0.58 ± 0.01
RXJ1206.5 + 2810	9.9	0.00	—	—	—	4 ± 1	96 ± 1	0.35 ± 0.01
RXJ1223.0 + 1037	10.1	0.00	—	—	——	2 ± 2	98 ± 2	0.25 ± 0.01
RXJ1230.7 + 1220	9.9	0.00	7 ± 1	—	—	—	93 ± 1	0.08 ± 0.01
A1664	<18.0	0.46	46 ± 1	—	43 ± 4	—	11 ± 3	0.73 ± 0.22
A1795	10.3	0.15	—	9 ± 2	19 ± 4	10 ± 7	62 ± 3	0.60 ± 0.03
A1835	10.4	0.40	24 ± 3	18 ± 6	29 ± 4	23 ± 5	6 ± 2	1.02 ± 0.38
	10.4	0.55	23 ± 4	31 ± 8	27 ± 6	19 ± 2	—	—
	<29.7	0.38	10 ± 3	35 ± 8	12 ± 5	16 ± 6	27 ± 3	6.55 ± 0.73
RXJ1442.2 + 2218	10.1	0.00	1 ± 1	—	—	–	99 ± 2	0.44 ± 0.01
A1991	9.9	0.00	—	—	—	4 ± 2	96 ± 2	0.49 ± 0.01
Z7160	<30.1	0.24	2 ± 1	—	6 ± 3	22 ± 6	70 ± 3	5.04 ± 0.18
A2052	9.4	0.22	—	3 ± 1	8 ± 3	17 ± 7	72 ± 3	0.54 ± 0.02
A2072	10.5	0.00	2 ± 1	—	—	—	98 ± 1	0.61 ± 0.01
RXJ1532.9 + 3021	8.6	0.21	25 ± 1	—	46 ± 2	—	29 ± 1	1.34 ± 0.06
A2146	<28.3	0.20	10 ± 1	—	—	24 ± 6	66 ± 5	2.66 ± 0.18
A2199	10.2	0.10	—	—	—	11 ± 1	89 ± 1	0.39 ± 0.01
A2204	9.6	0.00	26 ± 1	—	—	—	74 ± 1	0.92 ± 0.01
RXJ1715.3 + 5725	9.3	0.00	5 ± 1	—	—	—	95 ± 1	0.61 ± 0.01
Z8197	9.6	0.33	—	21 ± 1	—	16 ± 4	63 ± 2	1.70 ± 0.07
Z8276	9.4	0.24	8 ± 1	—	—	—	92 ± 1	0.82 ± 0.01
A2390	9.9	0.22	15 ± 1	—	9 ± 5	32 ± 9	44 ± 4	1.06 ± 0.10
A2495	10.1	0.00	4 ± 1	—	—	—	96 ± 1	0.41 ± 0.01

The central galaxies in Z235, A262, Z808, Z2701, Z3179, A1668, RXJ1320.1 + 3308, A1930, RXJ1733.0 + 4345, A2626b and A2634 did not require any excess stellar population above that of the template elliptical. RXJ0107.4 + 3227 required only a 0.4 per cent excess of O5 stars at 4500 Å.

4.2.2 Low-luminosity cooling flow systems

The variation in the properties of the cooling flow nebulae form a continuous trend with line luminosity (e.g., Figs 7 and 8), implying a gradual change in the dominance of ionization mechanism, rather than two discrete populations (cf. Heckman et al. 1989). The cooling flow galaxies with a lower luminosity emission-line region have stronger forbidden line emission to Balmer line emission ratios ([N II]/Hα∼2.4 and [S II]/Hα∼1, but [O III]/Hβ showing a large spread). Such line intensity ratios are traditionally difficult to explain, and require a steeper ionizing spectrum over 13.6–100 eV than can be produced by the O stars present in the higher luminosity systems. There is no evidence for an appreciable excess blue continuum in these galaxies (Figs 12 to 15), suggesting that massive stars cannot make such an important contribution to the ionization.

The line ratios suggest the introduction of an additional, harder ionizing source, and the nebulae are also physically smaller than the high-luminosity systems, suggesting that the dominant ionization source is not as spatially extended. Several processes have been proposed, such as self-irradiation from X-rays in the cooling flow (Voit & Donahue 1990; Donahue & Voit 1991; which is, however, in contradiction with the observed X-ray flux distribution) to self-absorbed mixing layers tapping both the kinetic and thermal energy of the gas (Crawford & Fabian 1992). Another realistic possibility is that as the amount of visible star formation decreases down the Hα-luminosity 'sequence', the relative importance of any low-level nuclear activity as an ionization source increases (Johnstone & Allen, in preparation). Determining the source of photoionization will require the radial mapping of the ionization parameter across the nebula in such systems.

At the very low-luminosity extreme of the Hα sequence we find a small fraction of [N II]-only line emitters in our sample, which are most common in the lower X-ray luminosity clusters ($< 10^{44}$ erg s^{-1}; Fig. 4). The line emission in these galaxies closely resembles that found in around half of ordinary elliptical galaxies (Phillips et al. 1986) ascribed to low-level LINER activity.

4.3 The non-cooling-flow line emitters

We have marked four obvious exceptions from the general behaviour of line emitters by different symbols in the correlations presented in Section 3. Specifically, there are two BCGs (in A1068 and A2146) with a combination of line ratios and line luminosity (high [N II]/Hα and [O III]/Hβ for their Hα luminosity) that suggests that the dominant form of ionization is due to an AGN (these are marked by open star symbols in Figs 7 to 15; note that the dominant galaxy in A2089 also shows a similar ionization state). A2146 also has prominent He IIλ4686 line emission (Fig. 2; Allen 1995), in agreement with the suggestions of a harder ionizing continuum than is usually seen in cooling flow nebulae. Follow-up

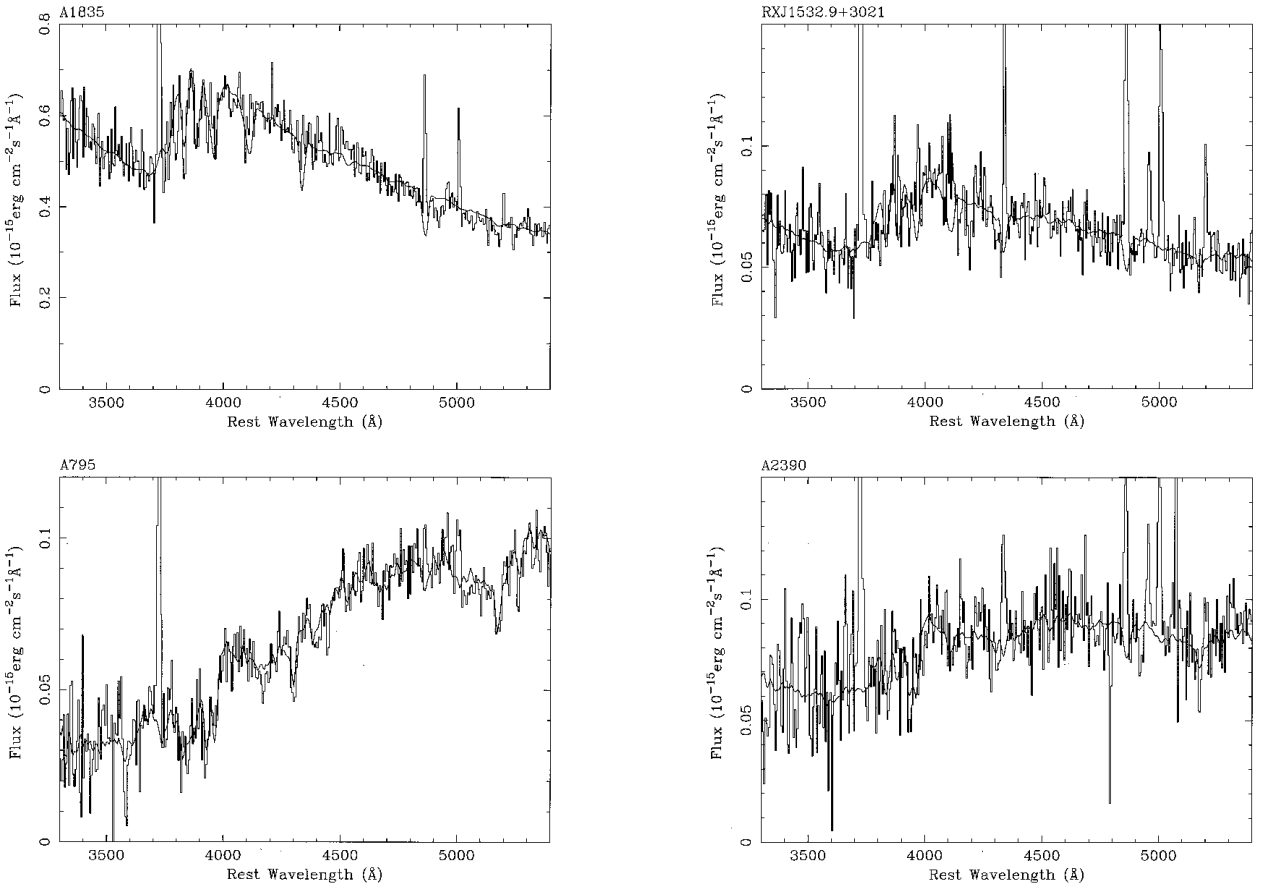

Figure 17. Four central cluster galaxy spectra (corrected for intrinsic reddening), each with the best-fit stellar model (smooth line) as in Table 7. The emission-line regions of the spectrum were not used in the fit.

X-ray observations confirm the presence of a point-like component of X-ray emission at the BCG in A2146 (at a small fraction of the overall cluster luminosity; Allen 1995). A similar situation may exist for A1068, where the presence of an AGN cannot be ruled out, although the *IRAS* fluxes and Wolf–Rayet features in this galaxy argue in favour of a massive starburst (Allen 1995). Two other systems (A2204 and RXJ0439.0 + 0520) also have high [N II]/Hα for their Hα luminosity, but other line ratios more consistent with the majority trend. Both these clusters contain strong central radio sources (Edge et al., in preparation) which might dilute the cooling flow properties.

Similarly, there are two galaxies offset from the general trend in the opposite direction (A2294 and RXJ0821.0 + 0752). These two galaxies have stronger Balmer lines relative to the forbidden-line emission, placing them more into the regime of classical H II regions (these are marked by open triangles in the Figs 7 to 15).

5 SUMMARY AND CONCLUSIONS

We have presented spectral observations of 256 dominant galaxies in 217 clusters, including 87 per cent of the 203 clusters that comprise the BCS. This sample has been supplemented with basic information about the brightest galaxy in a further 21 BCS clusters, as available from the literature. We have listed new redshifts for 17 clusters, mostly systems discovered through X-ray-selection. One such cluster, RXJ1532.9 + 3021, is at a redshift of $z = 0.36$, and is thus the second most distant object in the BCS.

27 per cent of the central dominant galaxies show narrow, low-ionization emission lines in their spectra, all but five with line intensity ratios typical of nebulae associated with galaxies at the centres of cooling flow clusters. A further 6 per cent of the clusters have central galaxies showing only [N II] line emission with Hα in absorption. We find no evidence for an increase in the frequency of line emission with X-ray luminosity, the distribution being consistent with a constant fraction. We also find that at low redshift a purely X-ray-selected cluster has a higher probability of containing an emission-line system around its dominant galaxy than an optically selected cluster. We find similar numbers of dominant galaxies in both optically selected and purely X-ray-selected clusters at low redshift included in optical catalogues, suggesting that the two techniques select clusters with similar properties. The projected separation between the optical positions of the BCG and the X-ray cluster centroid determined from RASS is smaller for the line-emitting BCGs than for those without line emission (at mean values of ~30 and ~90 kpc respectively). Assuming that the line emission traces a cooling flow system, this is consistent with the idea that there is a smaller offset between the gravitational centre and the central dominant galaxy in cooling flow clusters.

We have measured three stellar indices (δBR, Mg_2 and D_{4000}) from a spectrum extracted from the central 10 kpc of each galaxy in our sample; we have also fitted the emission lines in spectra extracted from both this region and the total span of the emission-line nebula. The total slit Hα ranges over four decades in luminosity ($10^{39} - 10^{43}$ erg s^{-1}), and the properties of the emission-line system follow continuous trends of behaviour across this full luminosity range. The more Hα-luminous systems

Table 8. Numbers of O5 stars and number ratios of massive stars from the fits given in Table 7. The rate of visible star formation (for the whole aperture as given in Table 7) inferred from these fits is given in the last column.

Name	No. of O5 stars	B5/O5	A5/O5	F5/O5	Visible SFR ($M_\odot\ yr^{-1}$)
A115	$9.3 \pm 1.2 \times 10^3$	—	2257 ± 864	—	0.20
A291	$9.1 \pm 0.3 \times 10^4$	—	—	—	0.99
RXJ0751.3+5012b	—	—	—	—	0.09
A646	$1.7 \pm 0.2 \times 10^4$	—	—	19254 ± 7158	0.40
RXJ1000.5+4409	—	—	—	—	0.52
A795	$1.3 \pm 0.1 \times 10^4$	—	—	—	0.14
Z3146	$1.51 \pm 0.03 \times 10^6$	—	—	—	16.43
A1068	$5.0 \pm 1.2 \times 10^5$	86 ± 61	1744 ± 875	29840 ± 10093	30.59
A1361	$1.1 \pm 0.2 \times 10^4$	—	—	—	0.12
RXJ1206.5+2810	—	—	—	—	0.06
RXJ1223.0+1037	—	—	—	—	0.03
RXJ1230.7+1220	$2.3 \pm 0.2 \times 10^2$	—	—	—	0.02
A1664	$1.17 \pm 0.03 \times 10^6$	—	1927 ± 173	—	23.06
A1795	—	—	—	—	1.94
A1835	$1.35 \pm 0.16 \times 10^6$	86 ± 31	2599 ± 505	17149 ± 4249	76.98
	$1.79 \pm 0.28 \times 10^6$	144 ± 43	2382 ± 636	13852 ± 2814	124.37
	$9.2 \pm 3.1 \times 10^5$	360 ± 145	2427 ± 1369	25877 ± 13472	125.13
RXJ1442.2+2218	$2.1 \pm 1.4 \times 10^2$	—	—	—	0.02
A1991	—	—	—	—	0.09
Z7160	$4.2 \pm 1.4 \times 10^4$	—	7565 ± 4562	232815 ± 94533	8.55
A2052	—	—	—	—	0.96
A2072	$3.5 \pm 1.6 \times 10^3$	—	—	—	0.04
RXJ1532.9+3021	$4.4 \pm 0.9 \times 10^5$	—	3724 ± 154	—	12.26
A2146	$1.4 \pm 0.2 \times 10^5$	—	—	41956 ± 11194	5.62
A2199	—	—	—	—	0.21
A2204	$1.2 \pm 0.1 \times 10^5$	—	—	—	1.29
RXJ1715.3+5725	$1.2 \pm 0.1 \times 10^4$	—	—	—	0.13
Z8197	—	—	—	—	7.86
Z8276	$2.8 \pm 0.2 \times 10^4$	—	—	—	0.30
A2390	$1.3 \pm 0.1 \times 10^5$	—	1218 ± 676	36993 ± 10350	5.40
A2495	$5.7 \pm 0.9 \times 10^3$	—	—	—	0.06

($L(\mathrm{H}\alpha \gtrsim 10^{41}$ erg s^{-1}) have the more spatially extended line-emitting regions (diameter > 20 kpc), and show a higher ratio of Balmer to forbidden line emission (i.e., [N II]/H$\alpha \lesssim 1$). Some of the more luminous systems are sufficiently extended that we can plot spatially resolved line ratios, and find that the ratio of forbidden to Balmer lines can either increase or decrease away from the centre of the galaxy. We find that this effect is too large to be simply ascribed to Hα stellar absorption affecting the line ratios where the emission is coincident with the underlying galaxy continuum, but is rather a real ionization effect. The Balmer decrement measured in the more luminous nebulae often implies the presence of internal dust, with reddening typically of $E(B-V) \sim 0.3$ (but with a wide range). These stronger line emitters also show a significantly blue spectrum.

After correction for intrinsic reddening (where appropriate), we have characterized the excess blue light in the high-L(Hα) galaxies by fitting simple template stellar spectra to their central continuum. Most of the galaxies require an excess population of O stars in sufficient numbers to provide the photoionization that can produce the observed Hα luminosity. Even though the distribution of stellar types is only crudely determined, the greater number of lower mass stars relative to the O-star population does not favour predictions from either continuous star formation or a single starburst. These findings are compatible with models that suggest the massive star formation is triggered from the interaction between outflowing plasma from the central radio source, and cold clouds deposited from, and embedded in a cluster cooling flow.

The lower Hα luminosity emission-line systems show line ratios (i.e., [N II]/H$\alpha \gtrsim 2$) requiring the introduction of a much harder source of ionization, and are much less spatially extended. The galaxy continuum shows no evidence for an appreciable amount of massive stars, with stellar indices little different from those expected from the stellar population of non-line-emitting dominant galaxies. Possibilities for the dominant ionization mechanism include turbulent mixing layers or low-level nuclear activity. The small fraction of [N II]-only emitters closely resemble the low-level LINER activity found in many ordinary elliptical galaxies.

There are only five obvious exceptions from the general trends shown by the line-emitting galaxies. At least one (A2146) shows evidence for contaminating photoionization by a central active nucleus. Two other galaxies (A2294 and RXJ0821.0+0752) have line intensity ratios suggestive of classical H II regions.

This paper is the first in a series detailing the observed properties of the BCS clusters in the radio, optical and X-ray wavebands. Later papers will investigate the dependence of the optical spectral characteristics of the dominant galaxies presented here with both the global cluster properties and those of any radio source contained in the BCG.

ACKNOWLEDGMENTS

CSC, ACE and ACF thank the Royal Society for financial support. Thanks are also due to Stefano Ettori for his help in observing during the 1996 December run, and to Roderick Johnstone for

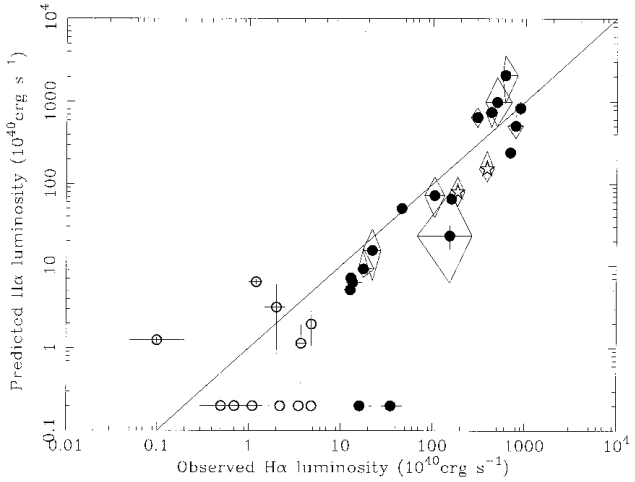

Figure 18. The observed Hα luminosity (corrected for reddening) plotted against the Hα luminosity predicted from the O-star component of the best-fit stellar model, assuming a covering fraction of unity. Error bars on the observed luminosity are from the errors to the fit to the Hα intensity, and on the predicted luminosity from the errors on the O-star component in the stellar model. The error diamonds around some points show the errors in the predicted luminosity when using the full range of $E(B-V)$ given by the errors in Table 4. High-Hα-luminosity systems [$L(\mathrm{H}\alpha) > 10^{41}$ erg s^{-1}] are shown by solid circles, those at lower Hα-luminosity by open circles, and the two high-ionization systems A1068 and A2146 by open stars. The points plotted at an arbitrary predicted luminosity of 2×10^{39} erg s^{-1} are those galaxies for which no O stars were required in the best-fit stellar population. The solid diagonal line gives the direct one-to-one relationship between the predicted and observed fluxes.

anything and everything to do with the computers. The INT is operated on the island of La Palma by the Isaac Newton Group in the Spanish Observatorio del Roque de los Muchachos of the Instituto de Astrofisica de Canarias. This research has made use of the NASA/IPAC Extragalactic Database (NED).

REFERENCES

Abell G. O., 1958, ApJS, 3, 211
Abell G. O., Corwin H. G., Olowin R. P., 1989, ApJS, 70, 1
Allen S. W., 1995, MNRAS, 276, 947
Allen S. W., 1998, MNRAS, 296, 392
Allen S. W., Fabian A. C., 1997, MNRAS, 286, 583
Allen S. W., Fabian A. C., 1998, MNRAS, 297, 63
Allen S. W. et al., 1992, MNRAS, 259, 67 (A92)
Baum S. A. et al., 1998, ApJ, 492, 854
Bohlin R. C., Savage B. D., Drake J. F., 1978, ApJ, 224, 132
Böhringer H., Voges W., Fabian A. C., Edge A. C., Neumann D. M., 1993, MNRAS, 264, 25
Bruzual G., 1983, ApJ, 273, 105
Cardelli J. A., Clayton G. C., Mathis J. S., 1989, ApJ, 345, 245
Cardiel N., Gorgas J., Aragon-Salamanca A., 1995, MNRAS, 277, 502
Cardiel N., Gorgas J., Aragon-Salamanca A., 1998, MNRAS, 298, 977
Colina L., Perez-Fournon I., 1990, ApJS, 72, 41
Crawford C. S., Fabian AC, 1992, MNRAS, 259, 265
Crawford CS, Fabian A. C., 1993, MNRAS, 265, 431
Crawford C. S., Edge A. C., Fabian A. C., Allen S. W., Böhringer H., Ebeling H., McMahon RG., Voges W., 1995, MNRAS, 274, 75 (C95)
Davoust E., Considere S., 1995, A&AS, 110, 19
Donahue M., Voit G. M., 1991, ApJ, 381, 361
Donahue M., Stocke J. T., Gioia I. M., 1992, ApJ, 385, 49
Ebeling H., Mendes de Oliveira C., White D. A., 1995, MNRAS, 277, 1006
Ebeling H., Voges W., Böhringer H., Edge A. C., Huchra J. P., Briel U. G., 1996, MNRAS, 281, 799
Ebeling H., Edge A. C., Fabian A. C., Allen S. W., Crawford C. S., Böhringer H., 1997, ApJL, 479, L101 (Paper II)
Ebeling H., Edge A. C., Böhringer H., Allen S. W., Crawford C. S., Fabian A. C., Voges W., Huchra J. P., 1998, MNRAS, 301, 881 (Paper I)
Edge A. C., Röttgering H., 1995, MNRAS, 277, 1580
Faber S. M., Friel E. D., Burstein D., Gaskel C. M., 1985, ApJS, 57, 711
Fabian A. C., 1994, ARA&A, 32, 277
Filippenko A. V., Terlevich R., 1992, ApJ, 397, L79
Gregory S. A., Burns J. O., 1982, ApJ, 255, 373
Heckman T. M., 1981, ApJ, 250, 59
Heckman T. M., Baum S. A., van Breugel W. J. M., McCarthy P., 1989, ApJ, 338, 48
Hu E. M., Cowie L. L., Wang Z., 1985, ApJS, 59, 447
Johnstone R. M., Fabian A. C., 1988, MNRAS, 233, 581
Johnstone R. M., Fabian A. C., Nulsen P. E. J., 1987, MNRAS, 224, 75 (JFN)
Kurucz R., 1979, ApJS, 40, 1
Laurikainen E., Moles M., 1989, ApJ, 345, 176
Le Borgne J. F., Pello R., Sanahuja B., 1992, A&AS, 95, 87
Lynds C. R., 1970, ApJL, 159, L151
McNamara B. R., 1995, ApJ, 443, 77
McNamara B. R., 1997, in Soker N., ed., ASP Conf. Ser. Vol. 115, Galactic and Cluster Cooling Flows. Astron. Soc. Pac., San Francisco, p. 109
McNamara B. R., O'Connell R. W., 1989, AJ, 98, 2018
McNamara B. R., O'Connell R. W., 1992, ApJ, 393, 579
McNamara B. R., O'Connell R. W., 1993, AJ, 105, 417
McNamara B. R., Wise M., Sarazin C. L., Jannuzi B. T., Elston R., 1996a, ApJ, 466, L9
McNamara B. R., O'Connell R. W., Sarazin C. L., 1996b, AJ, 112, 91
McNamara B. R., Jannuzi B. T., Sarazin C. L., Elston R., Wise M. W., 1996c, ApJ, 469, 66
McNamara B. R., Jannuzi B. T., Sarazin C. L., Elston R, Wise M. W., 1999, ApJ, in press
Maurogordato S., Proust D., Cappi A., Slezak E., Martin J. M., 1997, A&AS, 123, 411
O'Dea C. P., Owen F. N., 1985, AJ, 90, 954
Owen F. N., White R. A., Thronson H. A., 1988, AJ, 95, 1
Owen F. N., Ledlow M. J., Keel W. C., 1995, AJ, 109, 14
Peres C. B., Fabian A. C., Edge A. C., Allen S. W., Johnstone R. M., White D. A., 1998, MNRAS, 298, 416
Pesce J. E., Fabian A. C., Edge A. C., Johnstone R. M., 1990, MNRAS, 244, 58
Peterson B. M., 1978, ApJ, 223, 74
Phillips M. M., Jenkins C. R., Dopita M. A., Sadler E. M., Binette L., 1986, AJ, 91, 1062
Pinkney J. et al., 1996, ApJ, 468, L13
Porter A. C., Schniedel D. P., Hoessel J. G., 1991, AJ, 101, 1561
Rhee G. F. R. N., Katgert P., 1988, A&AS, 72, 243
Romanishin W., 1987, ApJ, 323, L113
Sandage A., 1978, AJ, 83, 904
Sarazin C. L., Baum S. A., O'Dea C. P., 1995a, ApJ, 451, 125
Sarazin C. L., Burns J. O., Roettger K., McNamara B. R., 1995b, ApJ, 447, 559
Shapiro S. L., Teukolsky S. A., 1983, Black Holes, White Dwarfs and Neutron Stars, John Wiley & Sons, New York
Stark A. A., Gammie C. F., Wilson R. W., Bally J., Linke R. A., Heiles C., Hurwitz M., 1992, ApJS, 79, 77
Stocke J. T. et al., 1991, ApJS, 76, 813
Struble M. F., Rood H. J., 1991, ApJS, 77, 363
Tadhunter C. N., Morganti R., di Serego Alighieri S., Fosbury R. A. E., Danziger I. J., 1993, MNRAS, 263, 999
Ulrich M.-H., 1976, ApJ, 206, 364
Voges W., 1992, Proceedings of Satellite Symposium 3, ESA ISY-3, p. 9
Voit G. M., Donahue M., 1990, ApJ, 360, L15
Wang Q. D., Ulmer M. P., Lavery R., 1997, MNRAS, 288, 702

White D. A., Fabian A. C., Johnstone R. M., Mushotzky R. F., Arnaud K. A., 1991, MNRAS, 252, 72

White D. A., Fabian A. C., Allen S. W., Edge A. C., Crawford C. S., Johnstone R. M., Stewart G. C., Voges W., 1994, MNRAS, 269, 589 (W94)

Zwicky F., Herzog E., Wild P., Karpowicz M., Kowal C. T., 1961–1968, Catalogue of Galaxies and Cluster Galaxies, Vols 1–6

This paper has been typeset from a TEX/LATEX file prepared by the author.